Thermal and Flow Field Investigations of a Micro-Tangential-Jet Film Cooling Scheme on Gas Turbine Components

Othman Hassan

A Thesis in the Department of

Mechanical and Industrial Engineering

Presented in Partial Fulfillment of the Requirements

For the Degree of Doctor of Philosophy

Concordia University

Montreal, Quebec, Canada

June 2013

CONCORDIA UNIVERSITY
SCHOOL OF GRADUATE STUDIES

This is to certify that the thesis prepared

By: Othman Hassan

Entitled: Thermal and Flow Field Investigations of a Micro-Tangential-Jet Film Cooling Scheme on Gas Turbine Components

and submitted in partial fulfillment of the requirements for the degree of

Doctor of Philosophy

complies with the regulations of the University and meets the accepted standards with respect to originality and quality.

Signed by the final examining committee:

Dr. Tarek Zayed — Chair

Dr. Stephane Moreau — External Examiner

Dr. Liangzhu Wang — External to Program

Dr. Wahid S. Ghaly — Examiner

Dr. Lyes Kadem — Examiner

Dr. Ibrahim Hassan — Thesis Supervisor

Approved by

Chair of Department or Graduate Program Director

Dean of Faculty

Abstract

Thermal and Flow Field Investigations of a Micro-Tangential-Jet Film Cooling Scheme on Gas Turbine Components

Othman Hassan, Ph.D.

Concordia University, 2013

Gas turbines play a major role in modern aerospace and in industrial power generation nowadays. Advanced gas turbines are designed to operate at increasingly higher inlet turbine gas temperature to increase their efficiency and specific power output. In order to enable this increase in the operating temperature, high-temperature resistant materials, Thermal-Barrier Coatings (TBCs), and advanced cooling techniques, are employed. Internal cooling, impingement cooling, and film cooling, are the typical cooling techniques that are being used nowadays for gas turbine engines cooling. For the past five decades, significant efforts have been implemented in the area of film cooling to design and investigate the performance of numerous cooling schemes at various operating conditions and geometries. However, the achieved effectiveness to date, especially over actual airfoil geometries, is still relatively low. Further efforts are essential to propose novel designs that are capable of providing the required cooling loads.

The present study investigates the thermal performance and flow characteristics downstream a new film cooling scheme over a gas turbine vane and a flat plate. The state-of-the-art transient Thermochromic Liquid Crystal (TLC) technique has been employed for film cooling measurements, while the Particle Image Velocimetry (PIV) technique has been employed for flow field investigations. Validation of all measurement techniques were conducted and good agreement with literature works has been achieved. The Micro-Tangential-Jet (MTJ) scheme is a discrete-holes shaped cooling scheme with micro sized exit height that supplies the jet parallel to the surface. The

MTJ scheme consists of two main parts, a circular supply micro-tube, and a shaped exit parallel to the vane surface. The shaped exit of the scheme starts with a circular cross section. Lateral expansion angles are then applied in both directions and a relatively constant height is maintained throughout the scheme yielding a squared exit. Due to the micro thickness of the jet, a deep penetration inside the main stream is achievable, while maintaining a tangential injection direction to the surface, thereby avoiding jet lift off.

The film cooling performance of one row of MTJ scheme on the vane pressure side and another row on the suction side is investigated at different blowing ratios using the transient TLC technique. Comparisons with the film cooling performance of previously proposed shaped schemes are carried out to highlight the advantages and disadvantages of the new design. Mach number distributions over the airfoil surface are determined with and without the MTJ scheme to investigate the effect of the added material on the airfoil characteristics. A comprehensive analysis based on the current findings, previous efforts in the literature, and the flow field investigations using the PIV technique downstream the MTJ scheme is presented. Overall, the new design showed superior film cooling performance, compared to the best achieved results in literature. The effectiveness distribution downstream the MTJ scheme was characterized with superior lateral spreading over both pressure and suction surfaces. The measurements showed similarity in the characteristics of the 2-D film downstream the MTJ scheme and the one that accompanies the injection from continuous slot schemes. Moreover, the investigations showed that the presence of the MTJ scheme over the vane pressure or suction sides did not result in significant HTC augmentation, especially at blowing ratios less than unity. The MTJ scheme could be the first of a new generation of film cooling schemes over airfoil geometries.

Acknowledgments

Praise be to Allah the almighty for giving me the success to finish my thesis.

Achieving the work presented in this thesis would not have been possible without the help and support of a number of people. I would like to thank my supervisor, Prof. Ibrahim Hassan, for his efforts with me throughout my Ph.D. program. Also, I would like to thank my research colleagues, Amin, Carole, Fan, Hamza, Ming, Qian and Yingjie for all their help and contributions in my work. I thank my family members, especially my parents, brothers and sister for their moral support and their encouragement during my study. My wife deserves heartfelt thanks for standing by my side throughout my degree program.

Table of Content

List of Figures

List of Tables

Nomenclature

Br	Blowing ratio, calculated based on the scheme exit area $(\rho_j u_j/\rho_m u_m)$
Br_s	Blowing ratio, the same coolant amount supplied to the scheme as the reference case
Br_b	Blowing ratio, calculated based on the scheme base area
C	Chord length (m)
C_p	Specific heat at constant pressure (kj/kg. K)
d	Diameter (m)
D_o	Distance between lens optical center and the target (m)
f	Lens focal length (m)
h	Heat transfer coefficient ($W/m^2.K$) and test section height (m)
k	Thermal conductivity (W/m.K)
L	Length (m)
Ma	Mach number
N	Number of images captured per test
n	Exponential constant
P	Pressure (N/m^2)

p	Film hole pitch (m)
q”	heat transfer flux (W/m^2)
Re	Reynolds number $(\rho D_h U_m/\mu)$
S	Height (m)
T	Temperature (K)
t	Time (s) & Thickness (m)
u	x-Velocity (m/s)
v	y-Velocity (m/s)
w	z-Velocity (m/s)
W	Width (m)
X	Axial direction
x	x-coordinate
y	y-coordinate
z	z-coordinate

Greek Symbols

θ	Dimensionless temperature and, Mounting angle of camera body (degrees)
α	Thermal diffusivity (m^2/s), = $(k/\rho C_p)$

η	Film cooling effectiveness $((T_f - T_m)/(T_j - T_m))$.
ρ	density (kg/m^3)
φ	Expansion angle (degree) and, Overall cooling effectiveness

Subscripts and Superscripts

aw	adiabatic wall
avg	average
c	centerline
f	film
h	hydraulic
i	initial
j	jet
m	main stream
o	stagnation and without
s	streamwise
w	wall

Abbreviations

2D	Two Dimensional

3D	Three Dimensional
CRVP	Counter Rotating Vortex Pair
DAQ	Data Acquisition
DJFC	Double Jet Film Cooling
HTC	Heat Transfer Coefficient
MTJ	Micro-Tangential-Jet
NHFR	Net Heat Flux Reduction
PIV	Particle Image Velocimetry
PSP	Pressure Sensitive Paint
RGB	Red-Green-Blue
SLRP	Stereo Lithography Rapid Prototyping
SN	Sublimation of Naphthalene
SP	Swollen Polymer
TIFF	Tagged Image File Format
TLC	Thermochromic Liquid Crystal
TSP	Temperature Sensitive Paint

Chapter 1

Introduction

1.1. Motivation

Gas turbines play a major role in modern aeronautical propulsion and power generation. Both the efficiency and the load density of gas turbine engines are dependent on the combustion gases inlet temperature to the turbine. 11^{o}C/year average increase in the maximum operating temperature of gas turbine engines were recorded due to thermal enhancements compared to only 5^{o}C/year due to components material properties enhancements, Downs and Landis (2009). It is clear that the achieved increase in the operating temperature due to thermal enhancement is more than twice the increase due to the component strength enhancement. Meanwhile, increasing the operating temperature requires efficient cooling techniques to protect the engine components from such high temperatures. Internal passage cooling, impingement cooling on the inner surfaces, and film cooling are the typical cooling techniques being used nowadays. Among those cooling techniques, film cooling is the most important one. Film cooling is the injection of compressed air onto the surface to be cooled, producing a thin coolant layer to protect the component surface from the hot gas stream. The protection provided by film cooling is mainly dependent on the film cooling scheme configuration. Designing new schemes and understanding the nature of interaction between the two cross streams, main and secondary, are essential to providing surface protection against the high inlet gas temperatures.

Numerous film cooling schemes were previously proposed in literature. A tangential jet injection from a continuous slot with a small lip thickness provides the best film cooling performance, Kacker and Whitelaw (1968). Meanwhile, discrete shaped holes provide better material strength, compared to continuous slots; however, the effectiveness performance of slot

schemes is much better. Applying tangential injection to actual airfoil surfaces is expected to change the airfoil aerodynamic loading characteristics; in order to minimize this effect, the scheme exit height must be at minimum; i.e., in the micro scale. Adding the benefits of micro injection to the benefits of tangential injection and discrete shaped holes is expected to provide optimal film cooling performance. Micro scaled jets have yet a further benefit; in effect a micro jet is capable of penetrating a deeper distance than a macro jet.

1.2. Objectives and Organization

The objectives of the present study are;

- To design a new film cooling scheme that is capable of providing superior film cooling performance to meet the needs of the next generation of gas turbines.
- To experimentally investigate the film cooling performance of the new scheme over an airfoil vane under a variety of flow conditions and for varying geometric parameters.
- To experimentally investigate the flow field characteristics downstream the new scheme and provide a better understanding of the interaction between the secondary and the main streams. This will also allow optimizing the scheme dimensions.

Chapter 2 is a comprehensive literature review in which the experimental efforts implemented in the area of film cooling are addressed. Such efforts include; 1) different film cooling schemes previously proposed, classified under macro and micro schemes, 2) a brief illustration of the alternative solutions previously proposed to overcome the challenges facing the application of shaped schemes such as the manufacturing expenses and machining difficulties, 3) the efforts implemented in the area of flow field investigations downstream film cooling schemes, and 4) a summary of the up to date situation of the film cooling technology. Chapter 3 is a description of the test facilities and experimental methodologies implemented throughout this study to achieve the desired objectives. The chapter includes details of the wind tunnel, test

sections, test vanes, calibration procedures, instrumentation and signals control systems, validations of different techniques, and the experimental uncertainties. Chapter 4 presents film cooling effectiveness investigations of the new film cooling scheme design, the MTJ scheme, at different blowing ratios using the transient TLC technique. The chapter includes the following; 1) the detailed geometrical ratios of the scheme and the test conditions, 2) the effect of the presence of the scheme added material over the vane surface on the resulting Mach number distribution, compared to the case when no MTJ scheme is used, 3) very detailed effectiveness distributions downstream the scheme on both pressure and suction sides and a comparison with the corresponding performance of another superior cooling scheme from literature, the louver scheme, at the same blowing ratios, and 4) a comparison between the MTJ scheme performance and numerous other film cooling schemes that were previously proposed in literature and had achieved enhanced effectiveness performance. Chapter 5 is complementary to chapter 4 and includes the Heat Transfer Coefficient (HTC) performance of the MTJ scheme. The chapter is composed of the same sections as in chapter 4. The HTC performance and the Net Heat Flux Reduction (NHFR) performance of the scheme are compared to the ones of the louver scheme and a number of previously proposed shaped schemes. Chapter 6 presents the flow field investigations downstream a scaled up model of the MTJ scheme, over a flat plate using the PIV technique. The chapter includes, 1) the detailed geometrical ratios of the Scaled-up MTJ scheme, 2) detailed velocity and vorticity characteristics downstream the MTJ scheme and a comparison with the corresponding flow characteristics downstream a circular hole cooling scheme, and 3) film cooling performance predictions of the MTJ scheme based on the flow field characteristics. Finally, chapter 7 summarizes the contributions of the present study and proposes recommendations for future studies.

Chapter 2

Literature Review

The research efforts that are being implemented in the area of film cooling could be divided into two main research directions; the first is the design of new cooling schemes with superior film cooling performance, and the second is the study of different flow parameters effects on the performance of a certain scheme design. Superior film cooling performance means high effectiveness, minimum heat transfer coefficient increase compared to the case with no film cooling, and optimal lateral secondary jet spreading. The first research direction was initiated with the design of continuous slot schemes. However, due to its harmful impact on the components material strength, it was replaced with discrete-holes schemes. Circular and shaped schemes are the typical discrete-holes schemes that are being used nowadays.

2.1. Macro-Film Cooling

2.1.1. Tangential-Jet Injection Slot Schemes

The inclination angle of the injection scheme is of special importance as it highly affects the scheme's film cooling performance. Zero inclination angle, tangential injection, has been proven to be the best case scenario by Goldstein et al. (1966), Hartnett et al. (1961), Seban (1960), Hatch and Papell (1959), Chin et al. (1958), Wieghardt (1946) and many others. Extensive research has been conducted to investigate the effect of different geometrical and flow parameters on the film cooling performance of continuous slot schemes with tangential injection. Kacker and Whitelaw (1968) investigated the effect of slot height and the injected coolant

turbulence intensity on the effectiveness of tangential slot injection. They investigated four different lip thickness to slot height ratios for a velocity ratio ranging from 0.288 to 2.66 and a density ratio of unity. They concluded that; 1) the film cooling effectiveness increases as the lip thickness to slot height ratio decreases, and is the most effective parameter in the case of tangential injection, 2) at a velocity ratio of unity, the maximum effectiveness corresponds to the minimum lip thickness to slot height ratio, 3) the turbulence intensity has minimal effect on the cooling effectiveness.

Burggraf and Huffmeier (1973) experimentally investigated the film cooling performance of a single, thick lip metered injection slot, Fig. 2.1a. They compared the effectiveness and the HTC of the new scheme with the previously published results of other slot scheme configurations such as, the ideal step slot, Fig. 2.1b, the ideal submerged slot, Fig. 2.1c, and the thick lip ideal step slot, Fig. 2.1d. They observed that the effectiveness is adversely affected by metering geometries and the lip thickness, when compared to ideal slot performance. They also concluded that the HTC performance could be correlated as a wall-jet type of heat transfer relationship when the blowing ratio is higher than unity. Moreover, they noticed increased heat transfer coefficient values with film cooling compared to corresponding values without film cooling and the maximum increase was in the area directly after the slot exit. The effect of a backward facing step on the film cooling effectiveness of thin and thick lip slot schemes was investigated by Matthews and Whitelaw (1973) at different blowing, density, and lip thickness to slot height ratios. Metzger et al. (1978) investigated experimentally the influence of upstream injection and intermediate panel temperature on multiple slot film cooling. A pair of flush, angled injection slots separated by intermediate heat transfer surface was used. They found that both the upstream slot and the intermediate surface have significant effect on the downstream film cooling performance. They concluded that ignoring the upstream effects or taking them partially into consideration, by using superposition, results in conservative estimates of the amount of film cooling flow needed.

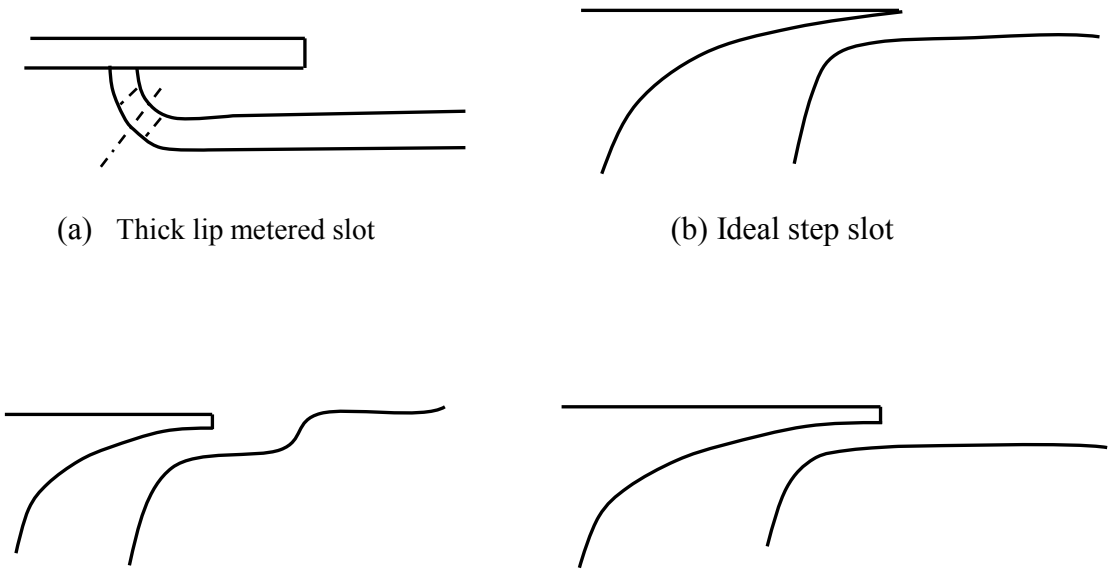

Figure 2.1, Tangential injection configurations

To sustain reasonable material strength, researchers replace the continuous slot with discrete circular holes parallel to the test surface. Nina and Whitelaw (1971) investigated thirteen different configurations of discrete-holes injection slots. They investigated the effect of open area ratio and lip length and thickness. They observed that a large open area ratio with a thin lip length in the range between 2.36 to 4 slot heights results in the highest effectiveness. Folayan and Whitelaw (1976) proposed a combined tangential and normal injection slot scheme with finite lip thickness. They investigated the effect of variety of parameters on the resulting effectiveness, such as; the lip length, pitch to diameter ratio, open area ratio, density ratio, ratio of tangential momentum to normal momentum, velocity ratio, distance of normal holes to the exit of tangential holes. The conclusions of their study are; 1) the effectiveness increases with increasing the velocity ration, lip length, and open area ratio, 2) for a given coolant flow rate, the influence of tangential to normal momentum ratio increase on the resulting effectiveness is small and tends to improve the effectiveness, and 3) single row of tangential holes with small pitch to diameter ratio results in a better performance than combined tangential and normal holes. Martiny et al. (1997) investigated experimentally the effect of a mixing jet on slot film cooling over a flat plate using electric heater foils in combination with IR thermography. They positioned the mixing jet five jet diameters downstream the slot exit and examined the performance at two different blowing rates, 1 and 2, which correspond to jet momentum rates of 7 and 10. They observed reduction in the film cooling effectiveness performance by about 15 to 25% in the interaction area downstream the mixing jet with HTC augmentation up to 100%.

Bittlinger et al. (1994) investigated experimentally the HTC performance resulting from tangential slot injection in the near slot region. They presented a data base that includes the velocity and temperature profiles, adiabatic wall temperature and heat transfer measurements for a wide range of blowing ratios, from 0.5 to 3.4. They concluded that; 1) the velocity and temperature profiles show pronounced dependence on the blowing ratio, 2) at blowing ratios less

than unity, the velocity profile is changing rapidly toward a turbulent boundary layer profile, 3) at blowing ratios higher than unity, a wall-jet like behavior is observed. Changing the internal profile of the slot was expected to have a contribution in the resulting film cooling performance. Farmer et al. (1997) investigated the effect of shaping the inclined slot on the film cooling effectiveness and the HTC performance over a flat plate experimentally using the TLC technique. They conducted the investigations in a subsonic wind tunnel using 35^{o} inclination angle slots and a density ratio of 1.55. They found that shaping the slot improves the overall film cooling performance, the effectiveness increases with a slight reduction in the HTC.

2.1.2. Shaped Discrete-Holes Injection Schemes

2.1.2.1. Fan-shaped and laidback fan-shaped schemes

Goldstein et al. (1974) proposed and investigated for the first time a circular hole scheme with an expanded exit over a flat plate. The expanded shaped exit scheme was created from a circular hole scheme by applying 10^{o} lateral expansion angles, resulting in the so-called fan-shaped scheme. The authors investigated the effect of various flow parameters on the film cooling effectiveness and used a flow visualization technique to observe the traces of the secondary stream. Flow visualization indicated a better jet attachment to the surface for the fan-shaped scheme relatively to the circular hole scheme. As a result, significant enhancement in the film cooling effectiveness for the fan-shaped scheme, compared to the circular one, was recorded at all investigated blowing ratios. The authors also concluded that the effect of density ratio is limited to cases of high blowing ratios and tends to enhance the effectiveness performance. Subsequently to Goldstein et al.'s study, many efforts have been implemented to propose novel shaped schemes designs and to investigate the effect of different geometrical and flow parameters on their film cooling performance.

Gritsch et al. (1998) investigated the performance of fan-shaped and laidback fan-shaped schemes, Fig. 2.2a, over a flat plate and compared the results with those of a circular hole scheme. They examined the effect of different flow and geometric parameters, such as the main stream and coolant Mach numbers and the orientation of the coolant supply with respect to the main stream direction. The investigations showed enhanced film cooling effectiveness performance for both shaped schemes in comparison to the circular one especially at high blowing ratios. Meanwhile, the laidback fan-shaped scheme provided better lateral coverage than the fan-shaped one. The authors also observed that the performance of the circular hole scheme was highly affected with changing the main stream Mach number from subsonic to supersonic values and by changing the coolant Mach number and the coolant supply direction at different blowing ratios. They related this performance to the formation of shock waves in the area of interaction of the two streams at supersonic main stream Mach numbers, and the presence of jet lift off at high blowing ratios. Gritsch et al. (2000) presented a complementary study to the previous one by investigating the HTC performance of the fan-shaped and laidback fan-shaped schemes. They observed that the shaped schemes provide significant reduction in the HTC values compared to circular hole schemes because of the enhanced jet spreading over the surface, especially at high blowing ratios. Moreover, the laidback fan-shaped scheme provides better HTC performance than the fan-shaped one.

Continuing the investigations of the extended exit schemes, Saumweber et al. (2003) investigated experimentally the effect of free stream turbulence intensity on the film cooling performance of the fan-shaped and laidback fan-shaped schemes at different blowing ratios. They noticed that, increasing the turbulence intensity lowers the film cooling effectiveness of the circular hole scheme at low blowing ratios due to the increased mixing between the two streams. Meanwhile a gain in the effectiveness was observed at high blowing ratios due to the enhanced lateral spreading and the diminished tendency of lifting off the surface.

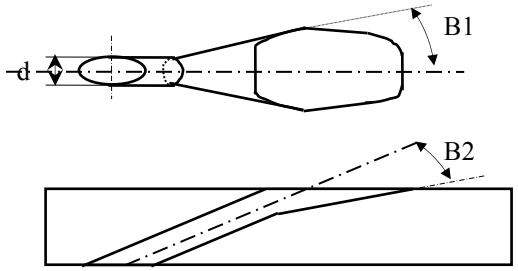

a) Laidback fan-shaped scheme, Gritsch et al. (1998)

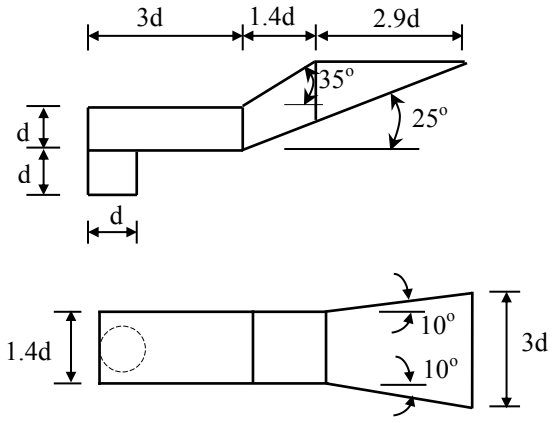

b) The louver scheme, Zhang and Hassan (2006)

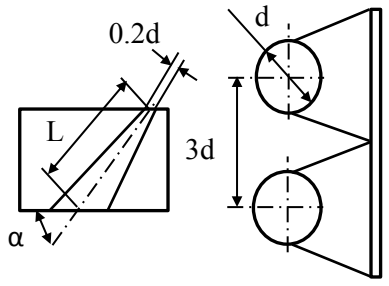

c) The console scheme, Sargison et al. (2002)

Figure 2.2, Shaped Schemes previously proposed and investigated in literature

With the case of holes with extended exit, they observed that the increase in turbulence intensity resulted in reduced film cooling effectiveness with all blowing ratios. The latter was due to the increased mixing between the two cross streams. Moreover, increasing the turbulence intensity resulted in increased HTC. The sensitivity to turbulence intensity change in the case of shaped schemes was more than the case of circular hole scheme. Saumweber and Schulz (2004) continued the previous study by investigating the effect of interaction between film cooling rows on the net film cooling performance downstream the last row. They came up with very useful conclusions as follows; a) the film cooling performance downstream two rows of holes is dominated by the second row geometry and blowing ratio, b) the film cooling effectiveness is significantly enhanced by double row injection in comparison to a single row injection, c) with double row injection, two rows of circular holes or one row of circular holes and one row of shaped holes, increasing the blowing ratio of the second row beyond the optimal value do not significantly affect the effectiveness. The latter is useful in extending the streamwise covered area, d) with double row injection from two rows of shaped schemes, increasing the blowing ratio results in improved film cooling effectiveness regardless of the blowing ratios applied.

The main target of the investigations carried out by Colban and Thole (2007) was to experimentally compare the film cooling benefits and the resulting aerodynamic losses between the fan-shaped and circular hole schemes. They observed increased aerodynamic losses with circular hole schemes, compared to the case without film cooling, and a shift in the passage vortex from the suction side towards the pressure side of the neighboring vane. They related the increased aerodynamic losses to the lift off accompanying the injection with high blowing ratios. Also, they found that the aerodynamic losses accompanying the fan-shaped schemes are much less than those accompanying the circular hole scheme due to the absence of lift off. Colban et al. (2007) continued their investigations of the fan-shaped scheme performance over gas turbine components. They investigated the film cooling effectiveness performance of multiple rows of

fan-shaped schemes over a gas turbine vane pressure and suction sides. They found that the coolant holes on the leading edge do not have significant contribution on the effectiveness of the pressure side. Meanwhile, and due to multiple injection the effectiveness on the pressure side increases with downstream distance. They observed similar performance over the suction side.

Gao et al. (2009) investigated experimentally the effect of compound injection, multiple rows effect and upstream wake on the film cooling performance of laidback fan-shaped schemes on gas turbine blade pressure and suction sides using the PSP technique. They stated that the film cooling effectiveness of compound angle laidback fan-shaped schemes is higher than those achieved with circular hole schemes. Moreover, they observed more uniform and laterally distributed jets with the laidback fan-shaped schemes than other cases. They also observed that the effectiveness was significantly affected by changing the upstream wake rod phase. A similar study was presented by Mhetras et al. (2007) as they studied the effect of flow parameter variations on the full coverage film effectiveness on a gas turbine blade using six rows of compound shaped holes experimentally. They concluded that; 1)the pressure gradient in the coolant cavity affects the blowing ratio in a hole row which results in accumulated coolant near the tip and under-cooling near the hub, 2) secondary flow vortices, such as the passage and tip vortices, have significant impact on the suction side effectiveness, 3) overall film effectiveness on the suction side is comparable to that on the pressure side even with less number of film rows, for all blowing ratios and free stream conditions, 4) mainstream Mach number and showerhead injection variation do not have significant impact on the film coverage over the blade surface. Zhang and Moon (2007) investigated the performance of single, double and triple rows injection. They also compared the effectiveness resulting from compound injection with the corresponding effectiveness calculated using the superposition principle. They observed under predictions in the calculated effectiveness with the superposition method, compared with those obtained from compound injection.

Wright et al. (2011) investigated the effect of density ratio and free stream turbulence intensity on the film cooling effectiveness of both fan-shaped and laidback fan-shaped schemes over a flat plate using the PSP technique. The main aim of their work was to extend the PSP application area to include the investigations of the density ratio variation on the film cooling effectiveness performance downstream various geometries. They observed that the effect of density ratio variation is more noticeable in the case of circular hole scheme than the cases of shaped schemes. The latter means that shaped schemes are more stable than circular hole schemes. Also, they observed that as the turbulence intensity increases the film cooling effectiveness decreases for both circular and shaped schemes.

The previously presented research efforts are not all what have been implemented to investigate the performance of the fan-shaped and laidback fan-shaped schemes. However, many other researches were conducted to investigate the effect of different geometrical and flow parameters on the film cooling performance of such schemes.

2.1.2.2. Shaped scheme with internal impingement effect

Combining the benefits of jet impinging and the enhanced film cooling performance of shaped schemes in one scheme, Immarigeon and Hassan (2005) numerically investigated the performance of the louver scheme. The louver scheme was originally proposed by Pratt & Whitney Canada. The louver scheme is a normal shaped scheme in which the flow is forced to go through a bend inside the scheme before being injected at the surface. This scheme provides thermal protection to the area upstream the hole exit, as well as the area downstream of it. The investigations showed that the louver scheme is capable of preventing lift off, compared to the circular hole scheme, at high blowing ratios. The authors also investigated the effect of the presence and arrangement of pedestals inside the scheme. The results indicated that those pedestals could be helpful in enhancing the performance of the scheme, based on their

arrangement. The pedestals affect the coolant spreading downstream the scheme exit. Zhang and Hassan (2006) continued the investigations of the louver scheme by presenting the modified louver, Fig. 2.2b. The modified louver is simpler in design than the one presented by Immarigeon and Hassan (2005) which facilitates the manufacturing of the scheme. The performance of the modified louver was very close to that of the original one. Zhang and Hassan (2006) investigated the performance of multiple, in-line and staggered arrangements of rows of louver holes numerically. The results showed that the louver scheme achieved the highest effectiveness, compared to other shaped schemes. Moreover, the staggered arrangement was found to be much better than the in-line one. The authors also found that three staggered rows did not achieve much enhancement in the cooling effectiveness relatively to two rows; however, slight reduction in the HTC was recorded with the three rows case.

To support the numerical findings of the previous studies, Ghorab et al. (2011) investigated the performance of one row of louver schemes over a flat plate experimentally using the transient TLC technique. They investigated the performance of one row of the louver schemes at three different blowing ratios and a density ratio close to unity. Similar findings to those achieved numerically were recorded. They observed enhanced centerline and laterally averaged effectiveness and reduced HTC, compared to circular hole scheme. They also observed minor effect of blowing ratio increase on the HTC performance. As a result, the louver scheme showed significant enhancement in the NHFR ratio when compared to other shaped schemes. Elnady et al. (2010a and b) investigated the performance of the louver scheme using a linear cascade and the transient TLC technique on both pressure and suction sides of actual airfoil vane geometry. They investigated the performance of single and double staggered rows injection. Besides the enhanced effectiveness performance in the case of double injection, they observed reduction in the HTC compared to the case of single row injection.

2.1.2.3. Converging slot schemes

Sargison et al. (2002) proposed and experimentally investigated the film cooling and aerodynamic performance of a converging-slot-hole (console) scheme, Fig. 2.2c, over a flat plate. The scheme entry section is circular and then it is expands in the lateral direction and converges in the streamwise direction. For the scheme exit to be similar to that of a slot scheme, they manufactured the scheme without intermediate gabs between adjacent holes. They compared the results of the console scheme with those of a 35^{o} inclination angle circular, a fan-shaped and a slot schemes. Their investigations showed that the effectiveness and the HTC of the console scheme are very close to those of slot scheme. Meanwhile, the aerodynamic losses accompanying the console scheme are significantly less than those accompanying the fan-shaped and circular hole schemes. As a continuation to the previous analysis, Sargison et al. (2002) investigated the film cooling performance of the console scheme on an engine guide vane using an annular cascade. They observed that the console scheme achieves film cooling performance close or equal to that of the fan-shaped scheme. Meanwhile, the observed aerodynamic losses in the case of the console scheme are only 20% of those accompanying the fan-shaped scheme. A flow visualization study of the console scheme was conducted by Sargison et al. (2005). Similar to the previous studies, they compared the performance of one row of the console scheme over a flat plate with the corresponding performance of one row of circular, fan-shaped and slot schemes. The experiments showed that the coolant film downstream the console scheme is close to that of a slot scheme, thin film attached to the surface at any momentum flux ratio. Also, they concluded that, the flow field is unsteady downstream all film cooling geometries.

As a continuation to the work of Sargison et al., Liu et al. (2010) investigated experimentally the thermal performance of the console scheme over a gas turbine blade using the TLC technique. They studied the performance of number of rows of holes on both pressure and suction sides. They investigated the performance of each row separately at different momentum

flux ratios and then they investigated the performance of all rows at the same time, including three rows of circular hole schemes on the leading edge. They came up with the following conclusions; 1) the jets traces converge on the suction side while they diverge on the pressure side for both the console and the circular hole schemes because of the passage vortex effect; meanwhile, the influence on the console scheme is much less than the corresponding effect on the circular one, 2) the jets of the console scheme are very well attached to the surface regardless of the momentum flux ratio, which is the same observation stated before by Sargison et al. (2005) over flat plate; however, the intermediate regions between holes are not very well covered by the jets, 3) no significant increase in the effectiveness of the suction surface as a result of increasing the momentum flux ratio was observed due to the tendency of the jet to lift off the surface; meanwhile, the effectiveness was notably enhanced on the pressure side by increasing the momentum flux ratio.

The great performance of the console scheme was the motivation of Liu et al. (2011 and 2012) to study the effect of variety of geometrical parameters on the film cooling performance of the scheme. The first parameter they considered was the effect of the exit-entry area ratio. They investigated two different exit-entry ratios, 0.67 and 1.33, which corresponds to divergence angles of 11^{o} and 21^{o}, respectively. The investigations showed that a smaller exit-entry area ratio results in better film cooling performance with all momentum flux ratios. Moreover, a momentum flux ratio of two results in optimal film cooling performance with both cases. The second parameter they considered was the effect of changing the straight console scheme exit area to a waist-shaped one. The purpose of adding the waist to the normal console scheme exit was to enforce part of the secondary stream to move towards the mid-span area. This in turn will sustain uniform coolant distribution all over the surface. They compared the results of the waist-shaped scheme with those of the normal console scheme with different divergence angles. They found that the waist-shaped scheme was very successful in covering the mid-span region; however, the

resulting average effectiveness was lower than the average effectiveness of the console scheme with small convergence angle. Meanwhile, the presence of the waist resulted in increased HTC values in the mid-span region due to the increased interaction between adjacent jets. They concluded that, a console scheme with small divergence angle gives better surface protection than a waist-shaped one; however, the flow resistance characteristics of the waist-shaped scheme is much better than that of the small divergence angle one because of the increased exit-entry area ratio.

All previously proposed and investigated shaped schemes showed enhanced film cooling performance, compared to circular hole schemes. The main disadvantages of shaped schemes are; the difficulty in manufacturing and the increased costs, compared to circular hole schemes. As a result, many research works have been conducted to find alternatives of shaped schemes.

2.1.2.4. Alternatives of shaped schemes

a) Circular hole schemes impeded in trenches or craters

Thermal Barrier Coating (TBC) is used nowadays to enhance the thermal resistance and life time of different gas turbine components. While spraying the TBC over the surface, special precautions must be considered regarding the film cooling holes, in order not to be closed. As a result of this process trenches and craters are formed around the holes exits. Lu et al. (2009) was the first who investigated the benefits of trenches on the film cooling performance of circular hole schemes. They investigated the effect of trench width and depth on the film cooling effectiveness and the HTC of one row of circular hole schemes using the IR thermography technique. The investigations showed that the effectiveness of trenched circular hole schemes is much better than the effectiveness of normal circular hole schemes; however, it was not as good as that of shaped schemes. They related this performance to the reduced momentum of the jet at the exit of the trench, compared to the case of individual jets of circular holes. The presence of the trench

resulted in increased turbulence on the surface and hence increased HTC values, compared to the circular hole scheme case. By investigating the effect of trench depth and width on the film cooling performance they found that a trench with a depth of 0.75D could be considered optimal. Lu et al. (2009) presented a similar study by investigating the performance of three different cratered geometries. They compared the results with those of circular, trenched, and shaped schemes. The investigations showed enhanced effectiveness performance with the cratered geometries, compared to normal circular hole schemes; however, the trenched and shaped schemes provided better effectiveness performance than them. By these two studies, a good alternative to the expensive shaped schemes became available.

Harrison et al. (2009) continued the investigations of circular holes impeded in transverse trenches by presenting detailed film cooling performance of trenched circular holes over an airfoil vane suction side experimentally. They applied both heated and non-heated upstream conditions to isolate the hydrodynamic effects of the trench and to highlight the effects of the thermal boundary layer. Also, they explored the effect of tripped and un-tripped boundary layer approaches. They found significant effect of the starting length conditions on the HTC. They observed higher increase in the HTC augmentation when the starting length was heated in comparison to when the starting length was not heated. They related this to the displacement of the thermal boundary layer by the injected gases. Also, the condition of the boundary layer, tripped or un-tripped, was found to have a significant effect on the HTC increase. A tripped boundary layer resulted in a much lower HTC increase than the corresponding un-tripped boundary layer. This was attributed to the transition of the boundary layer from laminar to turbulent in the case of the un-tripped boundary layer, while the tripped boundary layer was already turbulent. They noticed that the effect of blowing ratio on the HTC augmentation is not significant, except in the region directly after the scheme exit. Meanwhile, the scheme exit geometry has more significant effect is observed HTC than the blowing ratio. Dees et al. (2010)

presented a similar as that of Harrison et al. (2009) and experimentally investigated the HTC increase downstream dimple geometries. Similar to the trench scheme, the dimpled geometries are circular hole schemes with sudden change in the cross section of the scheme exit. Dees et al. (2010) investigated the film cooling of one row of three different dimple geometries, elliptic, tear drop, and diffuser, and a one row shaped schemes on the suction side of an airfoil under tripped and un-tripped boundary layer and heated and non-heated starting length conditions. They considered also the effect of turbulence intensity, Reynolds number, and blowing ratio. Their results for the shaped scheme are typically the same as the results of Harrison et al. (2009). Their general conclusion regarding the effect of the presence of dimple geometries on the HTC augmentation is that the dimples have an effect similar to that of the trip but the trip is more successful in causing boundary layer transition to turbulence than the dimple geometries.

b) Circular hole schemes with compound orientation

Many research works have been conducted to investigate the effect of different schemes orientation on the resulting effectiveness and HTC. Chappell et al. (2010) investigated four different hole designs, round axial, round compound, round radial and shaped axial, in the gill region of the suction side of an airfoil vane. They concluded that a round radial scheme could work as a good alternative of a shaped axial scheme, since its film cooling performance is close to that of the shaped axial scheme and its manufacturing costs are much cheaper. Chappell et al. (2010) continued the previous investigations by experimentally investigating the effect of different hole configuration on the aerodynamic losses. They concluded that; regardless of the film cooling hole configuration, applying film cooling results in aerodynamic loss by 4 to 45% compared to the case when no film cooling is used. Moreover, they found that the maximum aerodynamic loss occurs with the case or round radial and shaped axial schemes. This means that an optimization study must be conducted between the achieved enhancement in the cooling effectiveness and the resulting drawbacks on the aerodynamic losses.

c) Anti-vortex schemes

Based on the previously mentioned efforts in shaping the scheme exit, it is noticeable that shaping the scheme exit minimizes the interaction between the main and secondary streams. The latter is a result of the reduced secondary stream momentum component perpendicular to the main stream direction. Many research works have been conducted to investigate different factors affecting this interaction and the resulting vortical structure accompanying it. The flow field investigations showed the formation of a Counter Rotating Vortex Pair (CRVP) downstream the majority of film cooling schemes as a result of the velocity gradient at the boundaries of the secondary jet. This pair results in increased mixing between the two streams and hence reduced effectiveness performance. The intensity of the CRVP is at maximum with the circular hole scheme. The latter was the motivation of many researchers to propose geometrical modifications, anti-vortex hole configurations, to reduce the intensity of this pair. This in turn enhances the performance of circular hole schemes.

Kusterer et al. (2007) proposed the injection of the secondary stream from two separate circular holes being placed carefully in relation to each other, named Double Jet Film Cooling (DJFC), Fig. 2.3a. They concluded that an optimized location of the two schemes could generate an anti-kidney vortex pair. As a result, significant enhancement in the cooling effectiveness could be achieved. They continued the investigations and applied the DJFC scheme to a gas turbine blade and investigated the performance under real engine conditions. They found that the DJFC scheme is capable of replacing a row of shaped schemes on the suction side of the blade without negative effect on the thermal load. Heidmann and Ekkad (2008) proposed the injection from two side holes connected to a main circular hole, Fig. 2.3b. They investigated two different side branches locations numerically. In the first setup, the two side branches were connected to the main branch very close to the surface, in order to maximize the side angles. The performance was not good as the amount of coolant injected from the side branches was very small. They modified

this setup and changed the location of the two side branches to be close to the inlet of the main branch. This change increased the coolant amounts injected from the side branches. As a result, improvements in the film cooling effectiveness and the Net Heat Flux Reduction (NHFR) were achieved. A similar study was carried out by Li and Zhang (2010) as they proposed a single inlet and double outlet scheme, Fig 2.3c. They attached the side branch to the main branch, the trunk hole, at a distance 1d from the inlet and its exit was at a distance 3d from the exit of the main branch with a compound angle. The results of the setup was excellent since the generated vortices from the branch hole was capable of killing the strong CRVP of the main branch, especially at high blowing ratios. The HTC performance of the anti-vortex scheme was normal, increased HTC with blowing ratio increase; however, close to the hole exit the increase was significant due to the increased turbulence because of the interfering vortices.

Li et al. (2010) proposed and numerically investigated the nozzle scheme. The latter is a normal circular hole scheme with shaped orifices placed at different locations and orientations inside. They presented the film cooling effectiveness performance and the strength of the corresponding vortices of three different designs as well as the base line case, a circular hole scheme without orifices. The aim of the nozzle scheme was to control the velocity gradient at the hole exit and hence the strength of the resulting CRVP. Their technique was very successful in reducing the CRVP intensity close to the injection location. As a result, enhanced effectiveness performance, compared to the base line case, was achieved. They concluded that shaping the scheme exit is useful in reducing the momentum of the secondary jet and the enhancement of lateral jet spreading; however, if expansion angles are selected carefully the interaction between the two cross streams could be controlled and better results could be achieved.

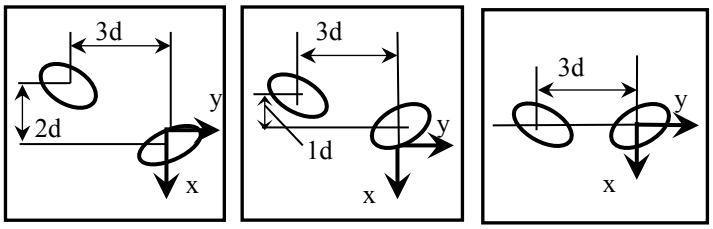

a) Double Jet Film Cooling, Kusterer et al. (2007)

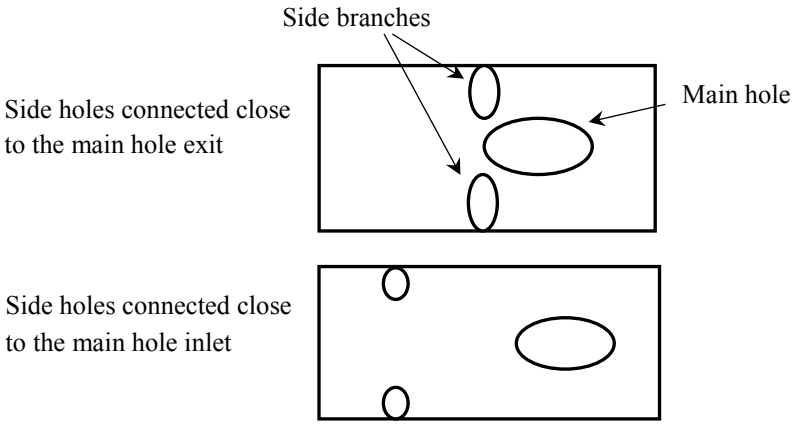

b) Side branches injection, Heidmann and Ekkad (2008)

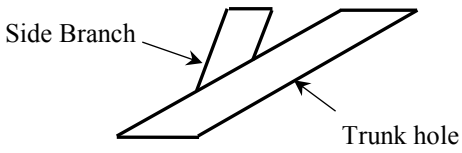

c) Single inlet double outlet scheme, Li and Zhang (2010)

Figure 2.3, Anti-vortex schemes

d) Circular hole schemes with external tabs or internal ridges

Ekkad et al. (2000) investigated the effect of different tab locations on the film cooling performance of circular hole schemes. They investigated different tabs locations, on the upstream edge, the downstream edge, and symmetrically along the spanwise edges. Placing tabs along the upstream edge showed enhanced effectiveness performance; however, the HTC was enhanced as well. The enhancement in the effectiveness was higher than the increase in the HTC and the net performance, represented in the NHFR, was positive. The other tab locations showed lower film protection than the case with no tabs. Nasir et al. (2003) completed the study of Ekkad et al. (2000) by investigating the effect of upstream tab orientation on the film cooling performance. They examined three different tab orientations, parallel to the surface, 45^{o} upwards, and 45^{o} downwards. For both velocity and turbulence intensity profiles it was noticed that the defect occurring in the boundary layer by the downward oriented tabs was at maximum. The increase in the HTC was much less than the enhancement in the effectiveness when horizontal and downward oriented tabs were used. Correspondingly, the net film cooling performance accompanying the use of horizontal or downward oriented tabs was positive. Upward oriented tabs showed very bad film cooling performance. The researchers concluded that; for the tabs to be effective, they should interact with the flow exiting the film cooling hole rather than the cross flow.

The tabs proposed by Ekkad et al. (2000) and Nasir et al. (2003) were not suitable from a practical point of view. In order for the tab geometry to be more applicable, Yang and Zhang (2012) proposed placing ridge-shaped tabs along the upstream edge of circular holes. The ridge shaped tabs resulted in more than 100% enhancement in the effectiveness, compared with the baseline case. However, they observed HTC enhancement, compared with the base line case, due to the increased turbulence. A reduction of about 100% in the heat flux without film cooling was recorded for the holes with the largest ridge-shaped tab installed. The main disadvantage of such

ridge-shaped tabs was the increased pressure drop across the cooling hole, compared to the base line case.

2.2. Micro-Film Cooling

Gau et al. (2009) experimentally investigated the performance of micro-free-jet flow using a micro slot nozzle manufactured by Micro-Electro-Mechanical System (MEMS) technique. They examined three different slot heights, 50, 100, and 200 μm, at different Reynolds numbers using flow visualization and instantaneous velocity measurements. Hot wire anemometer was used to measure both the velocity and the turbulence intensity of the jet. They reported superior performance of the micro jet in comparison with the macro one. Such superior performance is attributed to the absence of the surface vortices that accompany macro jets. Consequently, the micro jet has the slowest rate of decay in the centerline velocity and the slowest rate of increase in the centerline turbulence intensity. This allows the micro jet to penetrate the mainstream much deeper than the macro jet.

Getting benefit of the superior properties of micro jets, Li et al. (2009) experimentally investigated the film cooling performance of a micro slot over a flat plate. They investigated the performance schemes with different slot heights, 25, 45 and 50 μm, and different lip thicknesses, 100, 200 and 800 μm at blowing ratio range from 2.5 to 12.5. Using a 50 μm slot height and 800 μm lip thickness, the worst effectiveness performance was obtained due to the strong vortex generated in the back of the thick lip, while the best effectiveness performance was obtained when a slot height of 25 μm and a lip thickness of 100 μm were used. By comparing the effect of the lip thickness with micro and macro-film cooling, they found that the lip thickness with micro schemes is not as effective as that of macro schemes. One of the most important advantages they mentioned for the micro schemes over the macro ones is the reduced coolant amounts, it is two or

three times order of magnitude less than those supplied in the case of macro schemes. Such advantage must be considered carefully because of the number of rows of micro schemes needed to cover certain area is bigger than the number of rows of macro schemes needed to cover the same area.

2.3. Flow Field Investigations With Film Cooling

The flow nature accompanying cross injection with film cooling applications is very complex. Understanding such flow characteristics helps minimize the time and efforts applied in designing the injection schemes geometries. The Particle Image Velocimetry (PIV) technique is a powerful technique that is being implemented nowadays to investigate the flow characteristics of film cooling applications. Before the PIV was first proposed, researchers spent significant efforts to visualize the flow field downstream different injection schemes. To investigate the flow characteristics with compound injection of a shaped scheme, Lee et al. (2002) seeded the secondary stream with oil aerosol and illuminated it with two sets of 20mW He-Ne lasers. Using a high speed camera they were able to capture the motion of the injected coolant from compound angle shaped schemes. Their investigations showed the occurrence of reverse flow at the scheme exit with the compound injection cases. However, this did not affect the effectiveness performance of the schemes and enhanced effectiveness was recorded, compared to circular hole schemes.

Mahmood et al. (2005) used smoke to visualize the flow around an airfoil vane leading edge in a low speed wind tunnel. They succeeded in visualizing the vortical structure around the vane leading edge with and without leading edge fillets. The visualization of the flow field helped them decide which type of leading edge fillets was more useful, from heat transfer point of view, for the end wall region. Sargison et al. (2005) used two different flow visualization techniques to

visualize the flow downstream different coolant supply schemes over a flat plate. The aim of their study was to provide explanations to the enhancement in the effectiveness downstream their new design, the converging slot hole (console) scheme. They first used a fine nylon mesh covered with TLC to allow the measurement of the gas temperature contours in a direction perpendicular to the flow direction. Then they used the water/dry ice fog to visualize the flow. The investigations showed that the film downstream the console scheme is similar to that downstream a slot scheme. Moreover, the jet of the console scheme stayed thin and attached to the surface for long downstream distances even with very high momentum ratios. In a more advanced study, Polanka et al. (2002) presented the three components velocity field in the shower head region of a turbine blade using the Laser Doppler Velocimetry (LDV). They found that the spanwise orientation of the coolant jets had a dominating effect, as they observed very high levels of turbulence due to mainstream-jets interaction.

Berger and Liburdy (1998) applied the PIV technique to investigate the flow characteristics downstream a row of film cooling holes with different geometries and compound angles. Through their analysis they were able to clearly visualize the Counter Rotating Vortex Pair (CRVP) accompanying the circular hole scheme and to show the effect of changing the scheme exit configuration on the covered area by the jet and the vortex intensity. Their investigations showed that laterally diffused schemes without compound angles provides the best coverage in the near hole region. They also observed unique vorticity distributions downstream different geometries and compound angles. This in turn contributes to the heat transfer performance of the schemes. In another study, Aga et al. (2008) investigated the flow characteristics downstream a compound angled circular hole scheme over a flat plate. The visualization of the flow field downstream the compound angle circular hole scheme showed the absence of the CRVP vortices that accompany simple angled schemes and the presence of a large asymmetric vortex. The strength of the asymmetric vortex increases as the momentum flux ratio increases. Besides, they observed the

absence of secondary jet lift off even with high blowing ratios, Br = 3.0, which is a great advantage of compound angle injection. The findings of Aga et al. (2008) explains the enhancement in the cooling effectiveness of compound angle circular hole schemes, compared to normal simple angle schemes.

Takeshi et al. (2011) applied the PIV technique to investigate the flow field downstream optimized shaped schemes in a low speed wind tunnel. They observed different velocity distributions at the shaped schemes exits due to the change in the exit area configuration. With the laterally diffused scheme, they observed high velocity all over the exit area; however with the laterally and forward diffused exit, they observed high velocity at the upstream area of the exit and low velocity at the downstream area. Wright et al. (2011) investigated flow field characteristics downstream a circular hole scheme using the PIV technique. The aim of their study was to give a complete view of effect of the free stream turbulence intensity on the coolant-mainstream interaction at different blowing ratios. Their investigations showed that increasing the turbulence intensity helps the jet spreads laterally regardless of the blowing ratio value.

2.4. Summary of Literature

Significant efforts have been implemented in the area of film cooling of gas turbine components. Both thermal and flow field investigations, experimentally and numerically, have been conducted. The above mentioned literature could be summarized in the following points;

1- Applying tangential injection with the minimum possible lip thickness provides the best effectiveness performance. However, injecting the jet tangentially requires excess material on the surface which usually increases flow turbulence and enhances the HTC.

2- Discrete-holes schemes have been proposed to provide better material strength, compared to continuous slot schemes. The main disadvantage was the significant reduction in effectiveness performance, compared to continuous slot schemes.

3- Numerous discrete-holes schemes designs have been proposed in literature to provide enhanced effectiveness performance while maintaining reasonable material strength. Shaping the scheme exit helps reducing the momentum of the secondary jet and allows better attachment to the surface and a wider lateral jet spreading.

4- Due to the complexity of the manufacturing process of shaped schemes, significant research efforts have been conducted in designing simple alternatives to shaped schemes. The majority of these designs aimed to reduce the strength of the CRVP. Hence, better jet attachment characteristics could be obtained.

5- Micro jets have superior characteristics, compared to macro jets, represented in the absence of surface vortices. As a result, micro jets have a low rate of decay in the centerline velocity and a low rate of increase in the centerline turbulence intensity. This allows micro jets to penetrate deeper distances than macro jets.

6- Minor research efforts have been conducted in the area of micro-film cooling. The investigations carried out in this direction have shown promising results.

7- Visualizing the flow field downstream different film cooling configurations helps understanding the flow characteristics and hence designing more efficient schemes.

8- The PIV technique is a powerful technique to investigate the flow field characteristics downstream film cooling schemes.

2.5. Summary of Present Study Objectives

Based on the previously presented literature survey, the main objectives of the present study are;

1- To design a new film cooling scheme that combines the benefits of tangential jet injection and discrete-holes shaped schemes with micro dimensions.

2- To experimentally investigate the film cooling performance of the new scheme over an airfoil vane using the transient TLC technique. The investigations will be conducted under a variety of flow conditions and for varying geometric parameters.

3- To experimentally visualize and investigate the flow field characteristics downstream the new scheme using the PIV technique.

Chapter 3

Experimental Methodology

3.1. Test Facility

Figure 3.1 is a schematic diagram of the subsonic wind tunnel and its subcomponent established at Concordia University. The facility is designed so that both thermal and flow field investigations could be conducted. A separate Particle Image Velocimetry (PIV) system is available and is used throughout this study to investigate the flow field characteristics downstream film cooling schemes.

From thermal measurements point of view, the wind tunnel is composed of three main systems; mechanical, electronic, and thermography systems.

3.1.1. The Mechanical System

The mechanical system includes the supply loops of the main and secondary air streams, the flow meters, the heaters, and the pressure gauges and regulators. The main and secondary air streams are provided by a compressed air tank that has a pressure of 7 bars and a volume of $3.7m^3$. To mimic the real engine conditions, the main stream should be heated while the secondary stream is kept cold; however, the available air storage tank volume did not allow the heating of the main stream. As a result, the secondary stream is heated instead. Each flow loop is provided with pressure regulators, flow control valves, and flow meters. The pressure regulator of the main stream is a 1098-EGR-6351, 3" pressure regulator including 6351 pilot type

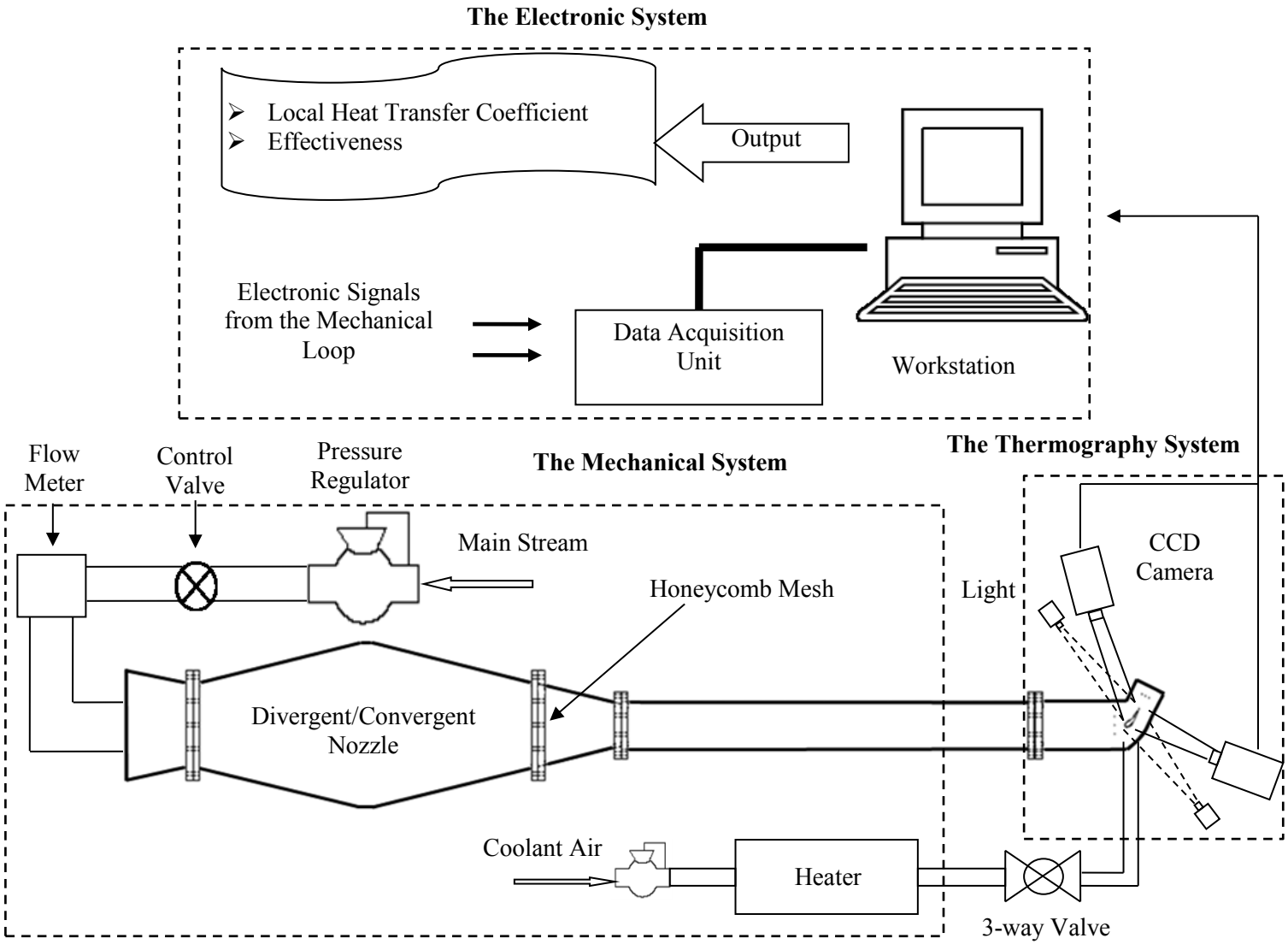

Figure 3.1, Schematic diagram of the test facility

(FISHER) with high sensitivity feedback. It has the capability of controlling the downstream main pressure with an outlet pressure ranging from 0.35 to 2.4 bars. This pressure range can be changed by replacing the adjusting spring. A Rosemount Multi-Variable flow meter (3095MV) is used to measure the main stream flow rate that is adjusted manually using a needle and gate control valve. The main flow meter records the load pressure and temperature to correct for density variations. For the secondary stream, a pressure regulator, R18-C05RG-LA (NORGREN), is connected before the air heater to control the secondary stream pressure that can range from 0.35 to 8.6 bars. A rotameter (FL-1502A) and a needle and gate control valve are used to measure and manually control the secondary stream flow rate, respectively.

To eliminate any fluctuations in the main stream supply, a divergent-convergent nozzle is installed in the mainstream flow path to settle down the main flow before entering the test section. The nozzle is manufactured of cast acrylic with 12.7mm wall thickness. Different nozzle dimensions were investigated numerically before manufacturing to identify the optimal design dimensions that yield the most uniform velocity profile at the exit of the divergent duct. The optimal inlet and outlet dimensions for the divergent nozzle, based on numerical simulations, are 152.4mm × 152.4mm, and 508.0mm × 275.0mm, respectively. The length of the nozzle is 700.0mm to allow a smooth transition between the inlet and the outlet sections. Meanwhile for the convergent section the inlet and outlet dimensions are 508.0mm × 275.0mm and 50.0mm × 110.0mm, respectively, with a length of 700.0mm. A fine grid mesh is installed at the exit of the divergent-convergent nozzle so that a turbulence intensity of 8.0 - 8.5% is maintained, based on the operating Reynolds number.

For the secondary stream to be heated, an air heater with a maximum capacity of 1.2kW is used. A variant is employed to adjust the power supplied to the heater and hence control the secondary stream temperature before being supplied to the test section. A 3-way solenoid valve is used to by-pass the flow during the heating up process. After a steady temperature is reached, the

flow is converted to the test section through a supply plenum with dimensions of 40.0mm × 20.0mm × 20.0mm. The plenum is used to ensure uniform secondary flow before the test vane.

3.1.2. The Thermography System

The thermography system includes the CCD camera, the Light source, the light supply, and the frame grabber. A 3CCD digital Toshiba camera (IK-TF7C) is used to capture the colored images of the TLC downstream the injection holes at a rate of 5 fps. Using A 1/3" C-Mount (TF8DA-8B) lens mounted on the 3CCD color camera, the zoom is adjusted through a focus ring, which has a scale of 1:2.2 / 8mm. The images captured by the camera are transferred to the work station through an NI PCIE-1340 dual frame grabber. To provide the test surface with the required light intensity, a variable intensity light source (Dolan-Jenner PL-800 fiber illuminator model) provided with optical fiber cables is used. The image quality depends on the adjustment of the lens, the light distribution and intensity. The light intensity is adjusted through an illuminator switch, which has a percentage scale ranging from 0 to 100. The captured, Red-Green-Blue (RGB) images are saved in Tagged Image File Format (TIFF) with a size of 1024 × 768 pixels. The images are then fed into an in-house MATLAB module to map them to the corresponding temperature distributions through an in-situ calibration process. During the analysis process, the RGB images are converted first to hue values, then to temperature values using the TLC calibration data provided from the calibration process.

3.1.3. The Electronic System

The electronic system includes the work station and the data acquisition (DAQ) system. A Pentium 4 Dell Precision workstation with 3.75GHz CPU, 3.25GB of RAMs and 250GB hard drive is used. An M-series NI DAQ system is used to capture the signal from all instruments and sensors, pressure, flow, and temperature. An in-house Labview code is used to manage the test

facility. The code controls the timing of valves opening and closing, recording of temperatures, pressures, flow rates, and the captured images.

3.2. Test Sections and Test Vanes

Three test sections were employed throughout this study. The first test section is a 2-D linear cascade manufactured to investigate the film cooling schemes performance over a gas turbine engine vane, Fig. 3.2a. As shown in the figure, the cascade is manufactured from a low conductivity transparent cast Acrylic. The cascade inlet cross section is 96.0mm × 51.0mm and its exit cross section is 29.5mm × 51.0mm. The cascade consists of two vanes, one in the middle and two halves on both sides. The sides of the test section are manufactured from transparent acrylic sheets to facilitate the imaging process. The cascade is designed so that the flow characteristics, pressure, and Mach number distributions, over the test vane surface are typical of those recorded over an actual airfoil gas turbine engine vane.

The geometrical properties of the vane used throughout this study are shown in Table 3.1. Figs. 3.2b, c, and d, are schematics of three different vanes manufactured for pressure measurement, calibration of the TLC material, and film cooling performance investigations, respectively. The pressure vanes, Fig. 3.2b, are manufactured with thirteen pressure holes on the vane surface for the pressure tubes to be installed. The first pressure prop is located at the stagnation line to measure the stagnation pressure. The remaining holes are distributed on both pressure and suction sides. This vane is used for pressure scanning and calculating the isentropic Mach number distribution around the vane surface. The isentropic flow assumption is applicable here because the maximum Mach number around the vane surface is 0.34 which allows the treatment of the flow as if it is an incompressible flow.

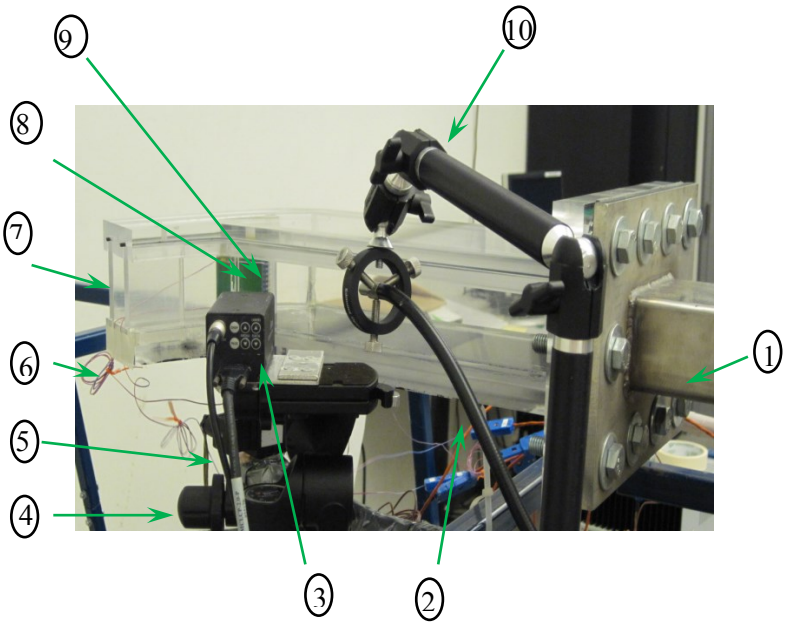

1	Main stream duct	2	Light supply
3	CCD camera	4	Camera holder
5	Secondary stream supply	6	Thermocouples
7	Mainstream exit	8	Test vane with TLC installed
9	Film holes	10	Light support

a) Test section

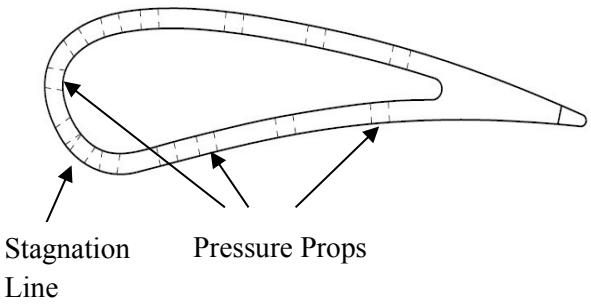

b) Pressure measurement vane

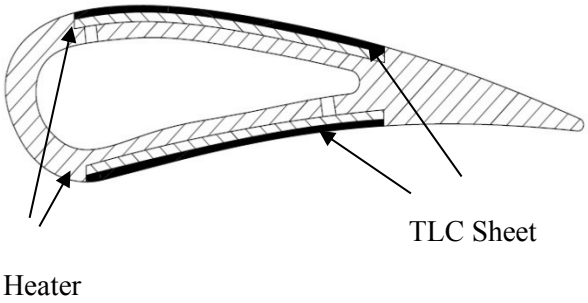

c) Calibration vane

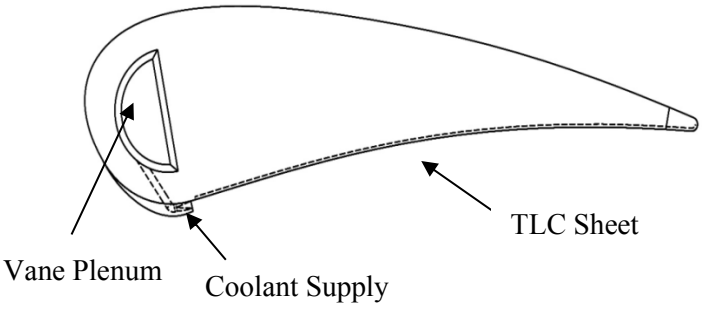

d) Vane with film cooling schemes

Figure 3.2, Vane test section and test vanes

Table 3.1, Current vane and validation vane geometrical properties

Parameter	Present test vane	Validation vane
True Chord, C (mm)	60.10	72.70
Axial Chord, Cx (mm)	38.88	48.50
Pitch, p (mm)	53.80	63.50
Span (mm)	54.00	127.00
Flow turning angle (degrees)	59.61	62.75

The calibration vane, Fig. 3.2c, has a special groove of 50.0mm × 50.0mm × 0.36mm to contain both the heater (Omega, KH-608/205P) and the TLC sheet. For every test set-up, this vane is used before starting the investigations to calibrate the TLC material. The calibration vane is manufactured shallow with a constant material thickness to allow uniform heat flux all over the TLC surface and correspondingly uniform color distribution. For all investigations, only one calibration vane was manufactured. The test vane, Fig 3.2d, has a groove in front of the film cooling scheme. The size of the groove is 50.0mm × 50.0mm × 0.2mm for the TLC sheets to be installed. The groove of the calibration vane and the test vane allows the TLC sheet to integrate the airfoil surface and minimize the resulting disturbance. During all investigations, separate vanes are manufactured for pressure side investigations and others are manufactured for suction side investigations. The reason for this is to ensure the supply of the designated coolant amount to the side under investigation. The difference in pressure between pressure and suction sides directs more coolant amounts towards the suction side than towards the pressure side. This coolant behavior results in a discrepancy between the actual supplied blowing ratios and the ones calculated theoretically. All vanes are manufactured from low conductivity material named Acura 60 using Stereo Lithography Rapid Prototyping (SLRP) technique. The test vane plenum size is manufactured as small as possible to minimize its impact on the film cooling performance of different schemes, close to the injection location. The thermal conductivity, k, of the vane material is 0.21 W/m. K, and the thermal diffusivity, α, is 0.13 m^2/s.

The second test section used in this study is a flat plate test section, Fig. 3.3. This test section is manufactured for two purposes; the first is to be used in the validation of the present methodology and technique, and the second is to be used for the flow field investigations downstream film cooling schemes using the PIV technique. The main test section is manufactured from a transparent material to facilitate imaging through the walls. The cross section of the test section is 99.0mm × 54.0mm and its length is 550.0mm. In the current test section, both the top

and bottom walls were removable to facilitate oil cleaning between tests and calibration of 3D measurements. The bottom plate was manufactured in two pieces, the first is the main body of the plate and the second is the region containing the film cooling schemes under investigation. This allows replacing the cooling scheme without disassembling the whole bottom plate, thereby minimizing the time of setup and the cost of manufacturing. The film cooling schemes were located at a distance of 200.0mm from the test section inlet to allow the main stream to develop before it interacts with the secondary stream. A plenum with internal dimensions of 65.0mm × 66.8mm × 45.0mm was used to supply the secondary stream to the test section.

The third test section is a 2-D linear cascade manufactured to validate the vane measurements and the test methodology. The test section dimensions imitate the work of Chappell et al. (2010). And the present results are compared to those of the reference work. The test vane geometrical dimensions are shown in Table 3.1. Three different vanes are manufactured, the first is for pressure scanning and is equipped with pressure taps all over the surface, the second is for the TLC calibration, and the third is for film cooling measurements. The cascade is manufactured with two vanes, one in the middle and two side halves. The flow characteristics around the vane surface measured throughout the present study are compared with the corresponding measurements of Chappell et al. (2010). This ensures the validity of the test section for film cooling investigations.

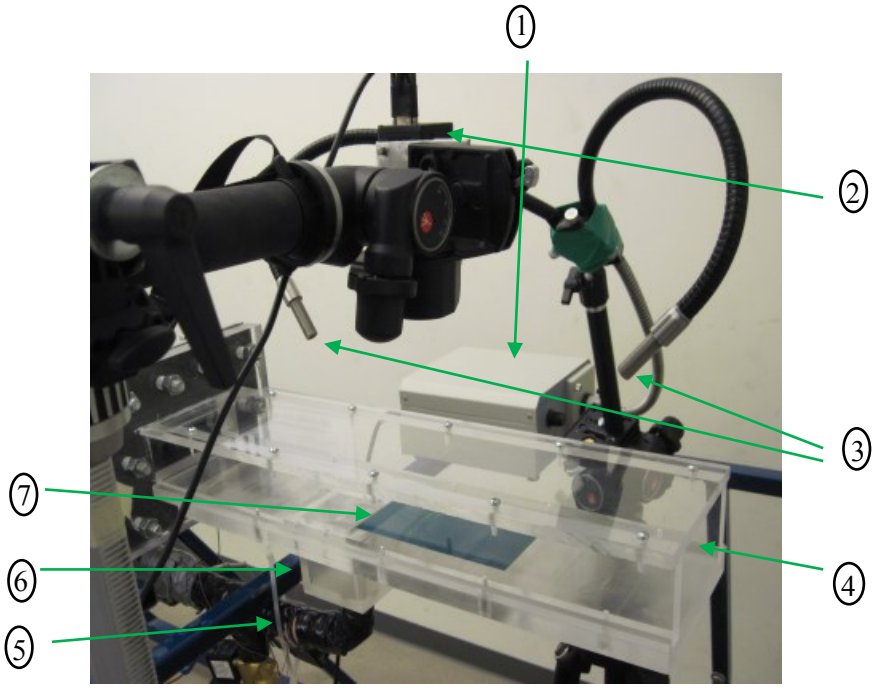

1	Light Source	2	CCD Camera
3	Light Supply	4	Main Duct
5	Coolant Supply	6	Plenum
7	TLC Sheet		

Figure 3.3, Flat plate test section details

3.3. Instrumentations and Signals Control System

Air flow meters, pressure transducers and thermocouples are selected and installed at specific locations along the test rig to measure the flow rate, pressure, and temperature of the main and secondary streams. Type-T thermocouples with a fine precision are used to measure the temperature of the secondary stream inside the plenum, inside the vane supply channel and at the film cooling scheme exit. Also, the same type of thermocouples is used to measure the main stream temperature at the entrance of the test section. A Rosemount multi-variable mass flow transmitter (3095MV) is used to measure the mainstream flow rate. A digital display and analog signal of 4-20mA are the two output signals from the multi-variable mass flow transmitter. Additionally, PGH-45L-100 Omega pressure gauges are placed in each loop to monitor the pressure.

The output signals from all instruments are connected to an M series National Instruments (NI) Data Acquisition System (DAQ), and are being monitored using labview software. An in-house labview code was developed to monitor and save various signals from pressure, flow, and temperature instruments under both steady and transient conditions. The solenoid valves are also controlled through the labview software. Fig. 3.4 presents a schematic diagram showing all connections and output signals from the instruments to the data acquisition system. The DAQ system consists of a SCXI-1000 signal-conditioning unit, with appropriate modules, NI PCI-6281 18-bit (analog input resolution), M series DAQ with an output rate of 2.8MS/s and a SCXI-116016 channel SPDT relay model. The instrument output analog signals are in mA and mV, as well as connect and disconnect signals. These signals are transferred to a DAQ card (PCI 6281) through a signal conditioner.

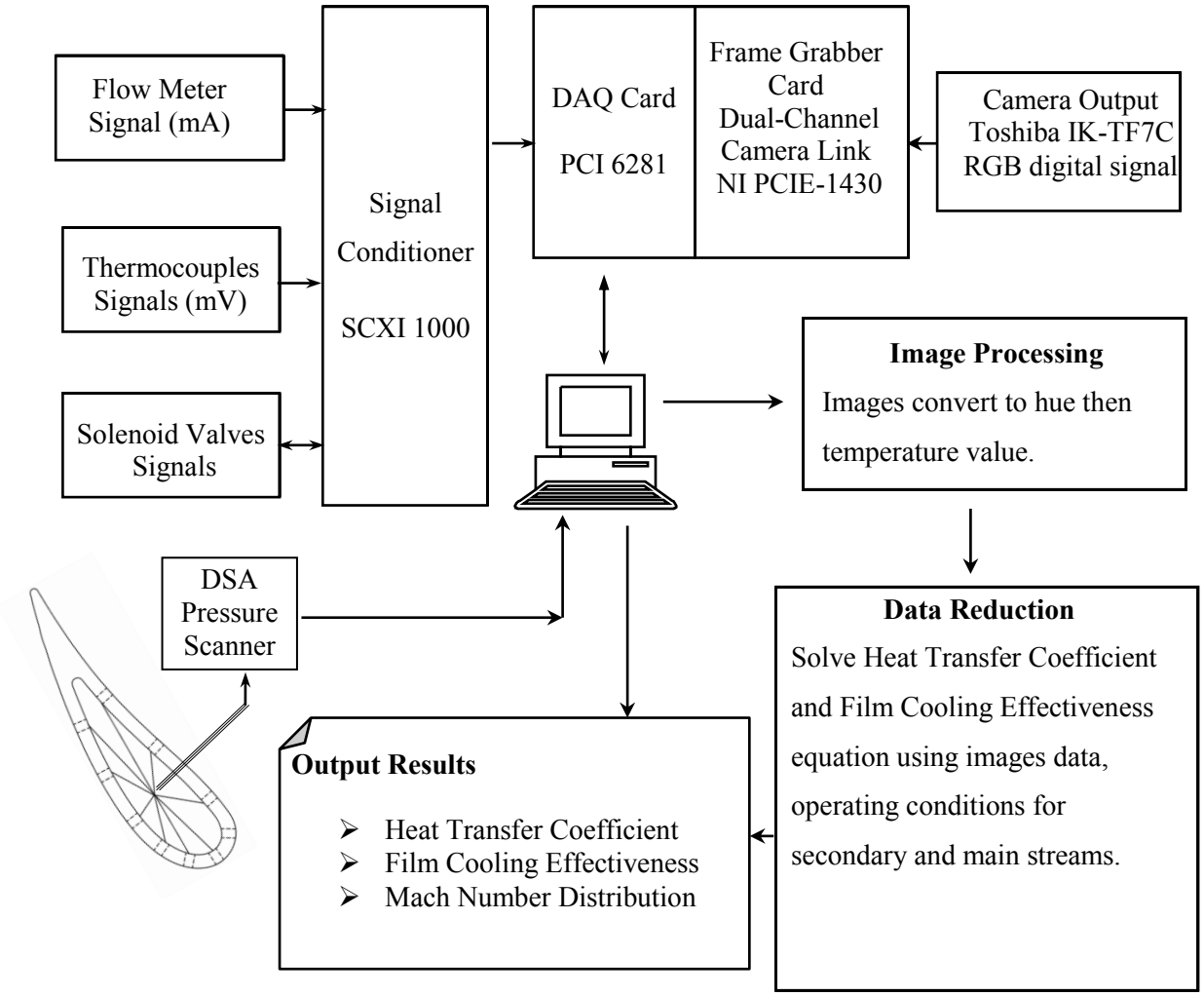

Figure 3.4, Schematic of the data processing system

3.4. Velocity Distribution Measurement Around the Airfoils

Determining the velocity and density distributions around the airfoil surface is essential in calculating the blowing ratio at the injection location. In order to scan the pressure distribution around the airfoil surface, pressure vanes are manufactured with thirteen pressure holes at different locations on the surface for the pressure tubes to be installed. One pressure tap is located at the stagnation line to measure the stagnation pressure and the rest of pressure taps are distributed on both pressure and suction sides. A DSA3217/16PX-10psid Scanivalve pressure transducer is used for this purpose. The pressure scanner channels are connected with the pressure taps on the vane surface using urethane (URTH-063) flexible tubing with 1/16" internal diameter. Using the DSA Link 3.03 software, the differential pressure at different locations on the vane surface is recorded.

During each blow down test, the total pressure and Reynolds number at the test section inlet are maintained in a continuous and steady fashion for up to 20 seconds time intervals. The pressure at each point is recorded at a rate of 20 Hz and averaged throughout the running time period. The inlet pressure to the test section is measured one axial chord length upstream of the vane leading edge. Since isentropic flow is assumed, Eq. (3.1) can be used to calculate the Mach number distribution around the vane surface, based on the measured pressure ratios at each tap location.

$$\frac{P_o}{P} = (1 + \frac{\gamma - 1}{2} M^2)^{\frac{\gamma}{\gamma - 1}} \tag{3.1}$$

Same as the pressure, the total temperature is assumed constant along the main flow streamlines and it can be calculated using the isentropic equations for incompressible flow. The

total temperature could be calculated from the Mach number and the measured temperature at a five chords distance upstream the vane leading edge using Eq. (3.2).

$$\frac{T_o}{T} = (1 + \frac{\gamma - 1}{2} M^2) \tag{3.2}$$

3.5. Thermochromic Liquid Crystals (TLC) Calibration

The calibration procedure that is applied in this study is the same for both vane and flat plate investigations. Narrow band TLC sheets with a temperature range from 20^{o}C to 25^{o}C are used to map the temperature distribution along the target area. Two thermocouples are used, one on the front part of the heater and one on the rear part, to capture the average heater surface temperature. While slightly increasing the power supplied to the heater through a DC regulator (BK PRECISION 1623A) and waiting proper time to achieve steady state, N-number of images are captured and a corresponding number of surface temperatures are recorded. The calibration target is placed in the same location of the test target and is illuminated using a high intensity light. A flexible fiber optic guide is used to get a uniform incident light distribution on the target area. The CCD camera, with 1024 × 768 pixel resolution, is placed as perpendicularly to the midpoint of the target area as possible. Using an in-house MATLAB code, any further captured images during the experiments are converted to the corresponding temperature distributions. The surface area of the TLC sheet is divided into several regions of interest and each region of interest is a square of n × n pixels. During the analysis each region of interest is considered separately. The precision of measurements is dependent on the size of the region of interest. The number of pixels is selected based on many factors such as the quality of images and the available processing time. The calibration of the TLC is carried out every time the set-up is changed and intermittently between tests, every few days, to ensure that the camera and the light positions

remain unchanged. The flat plate test area is much larger than the corresponding area of the vane surface. As a result, a flat Aluminum calibration target is used to ensure a homogeneous surface temperature distribution. Two heaters (Omega, KH-308/2P), with a maximum power output of 1.55W/cm^2, are used to supply a uniform heat flux to the TLC sheet during the calibration process. The two heaters are installed in a groove in the bottom surface of the calibration target, opposite to the test surface, to ensure a uniform heat distribution.

The surface curvature of the vane pressure and suction sides needs to be correlated to achieve more precise measurements. A uniform rectangle grid of 5 mm spacing is drawn on the vane surface to account for this effect. The vane is placed inside the cascade and an image is captured using the same camera setting. The x-distances between grid lines are measured as a number of pixels at different locations along the vane surface and correlated to the actual linear distance. This correlation shows less number of pixels on the curved surface early downstream, Cx < 50 % than later downstream, Cx > 50 %. This means that the measured distances early upstream, using the image, are shorter than the actual distances. A correlation should be applied to accurately predict the real distance. The z-distances are also verified and found to present uniform linear measurements along the vane span.

3.6. Data Reduction

The current investigations are being conducted with the transient liquid crystal technique. The technique requires a uniform initial target surface temperature that is exposed rapidly to the main and the secondary flows for a limited time period, Fig. 3.5. The TLC response to temperature changes is in the range of milliseconds. The test duration is chosen short enough to ensure that the heating pulse penetration into the surface is small compared to the wall thickness. Using these test conditions, the one dimension heat conduction assumption in a semi-infinite solid

medium could be applied. An analytical model of the transient surface temperature is then used to obtain the film cooling performance in terms of the cooling effectiveness and the HTC.

Equation (3.3) is the one dimensional transient heat conduction equation. Solving this equation using the initial and boundary conditions in Eq. (3.4) gives the system temperature as a function of the HTC and the thermal properties of the vane material, Eq. (3.5).

$$\rho C_p \frac{\partial T}{\partial t} = \frac{\partial}{\partial y}\left(k \frac{\partial T}{\partial y}\right) \tag{3.3}$$

$$\left.\begin{array}{l} @ \;\; t = 0, \qquad T = T_i \\ @ \;\; y = 0 \quad h\left(T_w - T_f\right) = -k \dfrac{\partial T}{\partial y} \\ @ \;\; y = \infty \quad T = T_m = T_i \end{array}\right\} \tag{3.4}$$

$$\frac{T_w - T_i}{T_f - T_i} = 1 - exp\left(\frac{h^2 \alpha t}{k^2}\right) erfc\left(\frac{h\sqrt{\alpha t}}{k}\right) \tag{3.5}$$

where $T_{w,}$ is the wall temperature and is measured using the TLC, and T_i and T_m are the initial and the mainstream temperatures, respectively, and are measured using thermocouples. The material thermal properties, α and k are the thermal diffusivity and the thermal conductivity, respectively, and t is the time corresponding to a wall temperature T_w. Using the definition of the film cooling effectiveness, Eq. (3.6), the unknown film temperature in Eq. (3.5) could be replaced with the film cooling effectiveness. Now, the objective is to solve Eq. (3.5) for the two unknowns, the film temperature or the effectiveness and the HTC.

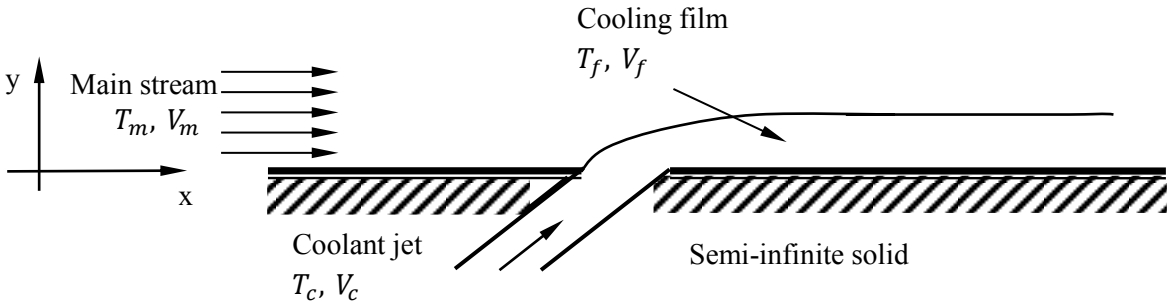

Figure 3.5, Flow conditions with film cooling injection

$$\eta = \frac{T_f - T_m}{T_c - T_m} \tag{3.6}$$

and hence

$$T_f = \eta T_c + T_m (1 - \eta) \tag{3.7}$$

One equation, Eq. (3.5), is not enough to determine two unknowns. As a result, two different time events are needed to construct two different equations from Eq. (3.5). Vedula and Metzegar (1991) proposed the two transient tests technique. During the two tests, the times needed to reach certain wall temperatures corresponding to different jet temperatures are recorded. In this case, the corresponding form of Eq. (3.5) will be

$$\frac{T_w - T_{i1}}{T_{f1} - T_{i1}} = \left[1 - exp\left(\frac{h^2 \alpha t_1}{k^2}\right) erfc\left(\frac{h\sqrt{\alpha t_1}}{k}\right)\right] \tag{3.8}$$

$$\frac{T_w - T_{i2}}{T_{f2} - T_{i2}} = \left[1 - exp\left(\frac{h^2 \alpha t_2}{k^2}\right) erfc\left(\frac{h\sqrt{\alpha t_2}}{k}\right)\right] \tag{3.9}$$

where t_1 is the time during the first test required to attain a certain wall temperature, T_w, and t_2 is the time during the second test required to attain the same wall temperature. By solving the two Eqs. (3.8) and (3.9) and by using the effectiveness definition of Eq. (3.6), the two unknowns are determined. In order to minimize the errors in the resulting effectiveness and HTC, the change in the main and secondary streams temperatures during the two tests should be minimized.

Another transient method was proposed by Licu et al. (2000). In their method, two time events are considered during the same transient test. Combining the two Eqs. (3.5) and (3.7) results in two Eqs. (3.10) and (3.11). The new of this method is that t_1 and t_2 are the times corresponding to two different wall temperatures, T_{w1} and T_{w2}, respectively, for the same coolant jet temperature.

$$\frac{T_{w1} - T_i}{\eta(T_c - T_m)} = \left[1 - exp\left(\frac{h^2 \alpha t_1}{k^2}\right) erfc\left(\frac{h\sqrt{\alpha t_1}}{k}\right)\right] \tag{3.10}$$

$$\frac{T_{w2} - T_i}{\eta(T_c - T_m)} = \left[1 - exp\left(\frac{h^2 \alpha t_2}{k^2}\right) erfc\left(\frac{h\sqrt{\alpha t_2}}{k}\right)\right] \tag{3.11}$$

As in the above described method of Licu et al. (2000), any variations in the main and secondary flow temperatures during the single transient test should be minimized in order to minimize the experimental error in the calculated effectiveness and HTC. However, it is very difficult to maintain constant main and secondary streams temperatures during the test. Duhamel's superposition theorem or the nonlinear least square regression analysis technique could be used to calculate the two unknowns while taking into account the variations in the secondary and the main streams temperatures. Hoffs (1996) and Lu (2007) used the regression analysis technique to reduce the experimental error for film cooling applications.

In order to apply the regression method, Eqs. (3.5) and (3.7) are combined into one equation, Eq. (3.12), in two unknowns, the effectiveness and the HTC. Now, the wall temperature can be determined in two different ways; first, by direct measurement using the TLC, and second, by calculating it from Eq. (3.12) based on assumed values of the effectiveness and the HTC that satisfy the condition in Eq. (3.13).

$$T_w - T_i = \left[1 - exp\left(\frac{h^2 \alpha t}{k^2}\right) erfc\left(\frac{h\sqrt{\alpha t}}{k}\right)\right] * [\eta(T_c - T_m) + T_m - T_i] \quad (3.12)$$

$$T_{w(ROI)}(\eta, h)\big|_{t=\tau} - T_{TLC(ROI)}\big|_{t=\tau} = 0.0 \quad (3.13)$$

A single transient test of 60 seconds at a rate of 5 Hz for a total number of 300 images *(N)* is considered in this study. Many trials were done to optimize the number of images needed so that the resulting effectiveness and HTC are independent of the number of images. The optimum solution is achieved by minimizing the least square error, ε, for each region of interest over the downstream film-cooling surface as follows

$$\varepsilon\,(\eta, h) = \frac{1}{2} \sum_{i=n}^{N} (T_{w(ROI)}(\eta, h)\big|_{t=\tau} - T_{TLC(ROI)}\big|_{t=\tau})^2 \quad (3.14)$$

where n is dependent on the time response of the secondary flow over the downstream TLC surface. Each region of interest has a different value of n, based on the flow conditions. For each test, different regions of interests are selected downstream of the film holes to determine the proper "n" values that could provide the minimum least square error, ε, in Eq. (3.14). A linear profile of "n" vs. x/d is used in the in-house Matlab code that is employed to calculate the effectiveness and the HTC. The "n" value increases in the downstream direction.

The same results obtained from the transient test could also be obtained from a steady state test. In this case, two different steady state experiments with different flow temperatures, and constant flow conditions for main and secondary streams, are needed. This method is not applicable in the current test facility as it is inadequate in attaining steady state conditions for the main flow for a sufficient period of time.

3.7. Experimental Uncertainty in Thermal Measurements

Uncertainty analysis is based on 95% confidence level and determined using the methodology of Klien and McClintock (1953). The average estimated uncertainties in the measured temperatures (thermocouples and TLC), flow rate, pressure, thermal diffusivity and thermal conductivity, are; $\mp$ 2%, $\mp$ 3%, $\mp$ 3%, $\mp$ 2% and $\mp$ 3%, respectively. The uncertainties of the instruments are based on the manufacturer specifications. Both the effectiveness and the HTC are functions of various flow parameters and as a result, the HTC could be presented in the form

$$h = f(T_w, T_m, T_c, T_i, t, \alpha, k, Br) \tag{3.15}$$

Hence, the uncertainty in the HTC is dependent on the uncertainties of all of the above mentioned parameters. In this case, the uncertainty in the HTC could be presented as the root mean square of the summation of the squares of the relative uncertainties of the measurement quantities. The resulting equation in this case will be in the form

$$Uh = \pm\sqrt{\left(\frac{\partial T_w}{T_w}\right)^2 + \left(\frac{\partial T_c}{T_c}\right)^2 + \left(\frac{\partial T_i}{T_i}\right)^2 + \left(\frac{\partial T_m}{T_m}\right)^2 + \left(\frac{\partial t}{t}\right)^2 + \left(\frac{\partial \alpha}{\alpha}\right)^2 + \left(\frac{\partial k}{k}\right)^2 + \left(\frac{\partial Br}{Br}\right)^2} \tag{3.16}$$

or

$$Uh = \pm\sqrt{(UT_w)^2 + (UT_c)^2 + (UT_i)^2 + (UT_m)^2 + (Ut)^2 + (U\alpha)^2 + (Uk)^2 + (UBr)^2} \tag{3.17}$$

Equation (3.17) is the main equation used to calculate the uncertainty for all measured quantities such as; the blowing ratio, the Mach number, the effectiveness, the HTC, and the

NHFR. As a result, the estimated uncertainties for blowing ratio, Mach number, effectiveness HTC, and NHFR are; $\mp$ 6%, $\mp$ 5%, $\mp$ 8%, $\mp$ 12% and $\mp$ 14%, respectively

3.8. Validation of Test Facility and Methodology

3.8.1. Flat Plate Measurements Validations

The work of Wright et al. (2011) was chosen to validate the present work. The reasons behind choosing the work of Wright et al. (2011) are; 1) they applied test conditions that are very close to those applied throughout the present study, 2) they presented acceptable validation of their work with previous works, 3) they implemented a different thermography technique, the transient Pressure Sensitive Paint (PSP) technique, from the one implemented throughout the present study, the transient TLC technique. The third reason allows verifying the effect of changing the thermography technique on the results. Two schemes were manufactured and investigated, a circular hole scheme and a fan-shaped one. Throughout their analysis, Wright et al. (2011) applied a relatively low Reynolds number, 0.7E5. Such range of Reynolds numbers is accompanied with high uncertainty level in the measured parameters using the current test facility. This is due to two reasons; the first is related to the TLC sheets used for wall temperature measurements and the second is related to a design problem in the test target. The presence of the TLC sheet edge in front of the scheme exit results in an enhanced jet distribution in the lateral direction which accordingly reduces the centerline effectiveness. To overcome this challenge, the TLC sheet was impeded in a groove machined on the surface in order to integrate with the surface and reduce the disturbance. However, some complications incurred from the presence of the groove and as a result, the surface was flushed and the groove was removed again. Moreover, the test section is designed so that the film cooling scheme can be replaced without changing the whole test target in order to minimize efforts during experiments and manufacturing costs. This

resulted in the presence of a small gap between the location of the scheme exit and the TLC sheet which works as an obstacle in front of the injection schemes. The impact of the previously mentioned obstacle decays with increasing Reynolds number due to the enhanced jets strength.

Figure 3.6 is a comparison of the centerline and spanwise-averaged effectiveness of one row of circular hole schemes over a flat plate with the work of Wright et al. (2011). From the figure, good agreement is noticeable at both blowing ratios, for centerline and laterally averaged effectiveness, along the downstream area. The agreement in the average effectiveness close to the injection location at $Br_b = 1.0$ is not as good as the one obtained at $Br_b = 0.5$. This is due to the presence of jet lift off at $Br_b = 1.0$ and the presence of the previously mentioned obstacles in front of the injection location. The impact of the TLC edge is represented in the enhanced effectiveness close to the injection location, $x/d < 3.0$, as the TLC sheet thickness enhances the attachment of the jet to the surface, because it reduces the actual vertical penetration distance of the jet, perpendicular to the surface.

The effectiveness performance of one row of fan-shaped schemes is presented in Fig. 3.7. Two Reynolds numbers were investigated; the first is a low Reynolds number, 0.7E5, applied by Wright et al. (2011), and the second is a high Reynolds number, 1.24E5, and is the one applied for all flat plate investigations conducted throughout this study. From the figure, good agreements in the centerline and laterally averaged effectiveness are noticeable at high and low blowing ratios with the high Reynolds number case. However; with the low Reynolds number case the agreement is limited to the laterally averaged effectiveness. This proves the aforementioned point regarding the effect of the presence of the TLC sheet and the small gap in front of the scheme exit. For low Reynolds number cases, the secondary jet is weak and the effect of any disturbance in front of the jet has a significant impact on the resulting effectiveness.

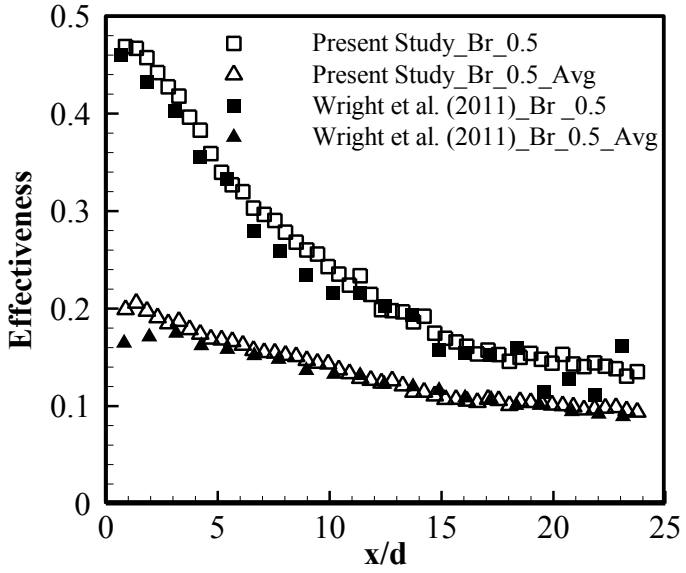

a) $Br_b = 0.5$

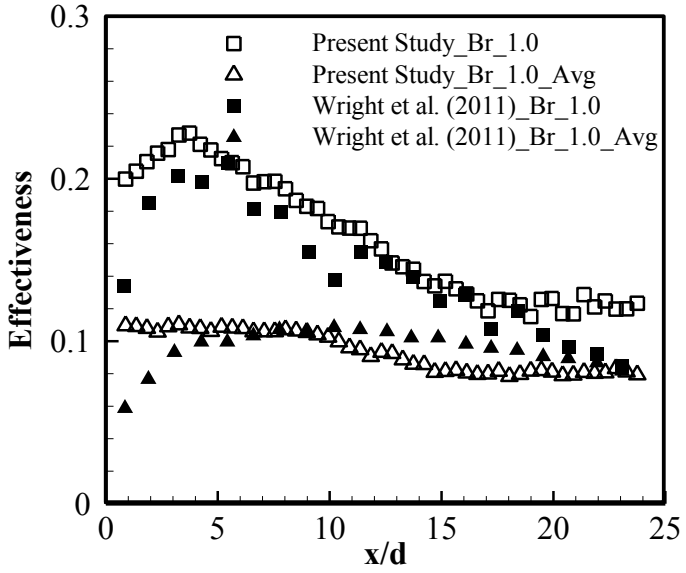

b) $Br_b = 1.0$

Figure 3.6, Centerline and laterally averaged effectiveness comparison downstream one row of circular hole schemes between present study and the work of Wright et al. (2011)

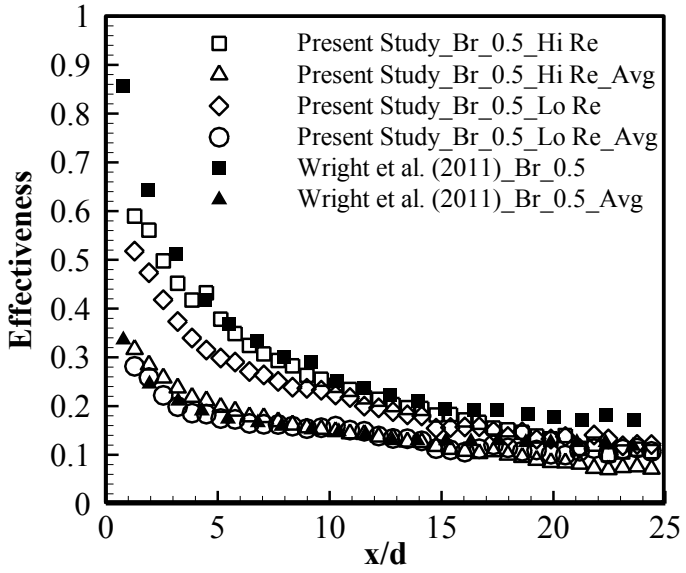

a) $Br_b = 0.5$

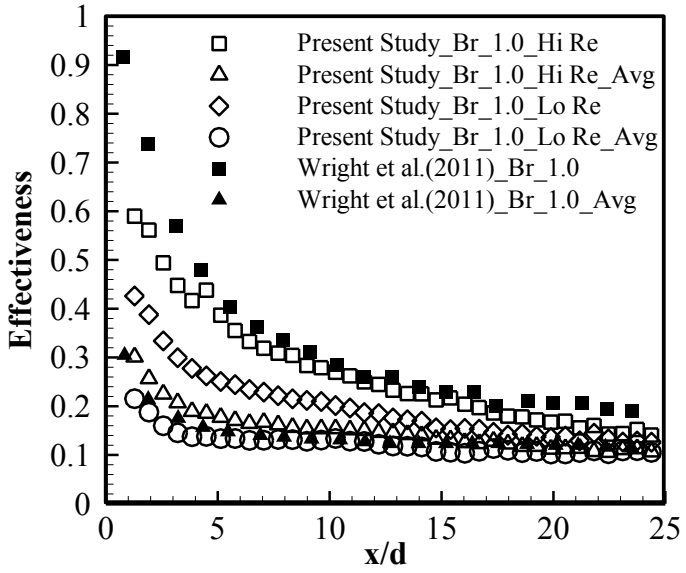

b) $Br_b = 1.0$

Figure 3.7, Centerline and laterally averaged effectiveness comparison downstream one row of fan-shaped schemes between present study and the work of Wright et al. (2011)

3.8.2. Vane Measurements Validation

Before proceeding to the investigations of the new scheme, the test facility and test methodology were validated. The test section of Chappell et al. (2010) was manufactured and both pressure and film cooling measurements were conducted. The geometrical properties of the vane used with Chappell et al. (2010) are listed in Table 3.1. All geometrical and flow parameters in the reference work were considered and applied while manufacturing and testing the current test section. The authors of the reference work applied density ratios from 1.73 to 1.92 by employing foreign gases; however, due to space and cost limitations, the density ratio considered throughout this validation study was close to unity. Previous investigations showed that the effect of density ratio is not significant and is limited to the cases of low blowing ratios, Wright et al. (2011).

By scanning the pressure distribution around the vane surface, the Mach number distribution was determined. The agreement in the Mach number distribution between the current work and the work of Chappell et al. (2010), Fig. 3.8, confirms the validity of the current test section for film cooling performance validation. The discrepancy on the suction side Mach number between present and reference works is clear at two locations, namely, number 2 and 3 from the trailing edge. Further investigations of the sources of this discrepancy showed that it is a result of a defect on the vane surface at this location. However, the performance everywhere else, especially at the region of interest, on both pressure and suction sides is very good.

The film cooling performance of two rows of circular hole schemes in the gill region of the suction side in staggered arrangement with a total number of thirteen holes was investigated. The holes are located on the suction side at distances of 15 and 25% of the axial chord. Chappell et al. (2010) used the transient Infra-Red (IR) technique throughout their investigations. However, in the present study, the transient TLC technique was applied. This adds one advantage to the

validation as it shows the impact of the thermography technique on the obtained results. The film cooling effectiveness and the HTC comparisons between the current and the reference studies are shown in Figs. 3.9a and b, respectively. Regarding the effectiveness performance, good agreement between present and reference works is noticeable in Fig. 3.9a. The agreement in the case of $Br_b = 1.2$ is good all over the downstream area while for $Br_b = 0.9$ the agreement is not good after $x/d > 30$ and for $Br_b = 0.6$ the agreement is not good after $x/d > 20$. Such performance could be related to the effect of using different density ratios between present and reference studies as the effect of density ratio is clear with low blowing ratios and decays by increasing the blowing ratio. Moreover, the trend of the effectiveness performance of the double rows staggered circular hole schemes of the present investigations is in agreement with the corresponding results of circular hole schemes over flat plate. The optimal effectiveness accompanies $Br_b = 0.6$ and then a reduction in effectiveness is observable by increasing the blowing ratio from 0.6 to 0.9 and from 0.9 to 1.2. In the present study and because of the thermography technique applied, the TLC technique, the authors were unable to determine the effectiveness or the HTC values in the region between $x/d = 0.0$ and $x/d = 10$ due to the presence of the injection schemes. Chappell et al. (2010) were able to measure in this region because they used the IR technique. Regarding the HTC, Fig. 3.9b, the agreement between the present results and those of Chappell et al. (2010) is quite good, considering the difficulties accompanying the measurements in the gill region of the suction side.

The comparisons in Figs. 3.6-3.9 validate the experimental apparatus and procedures employed

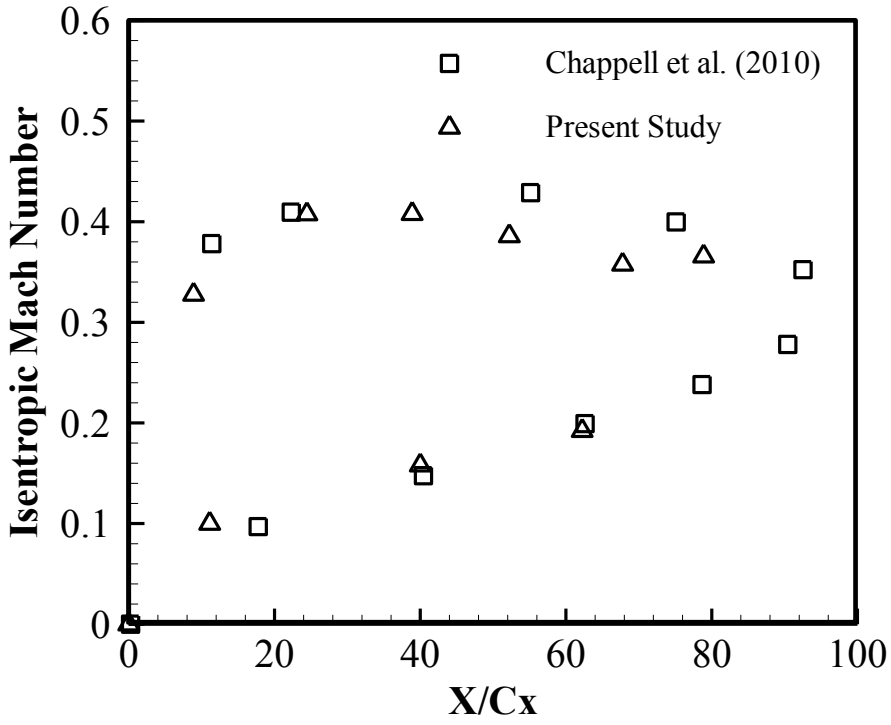

Figure 3.8, Mach number comparison between present and reference work of Chappell et al. (2010)

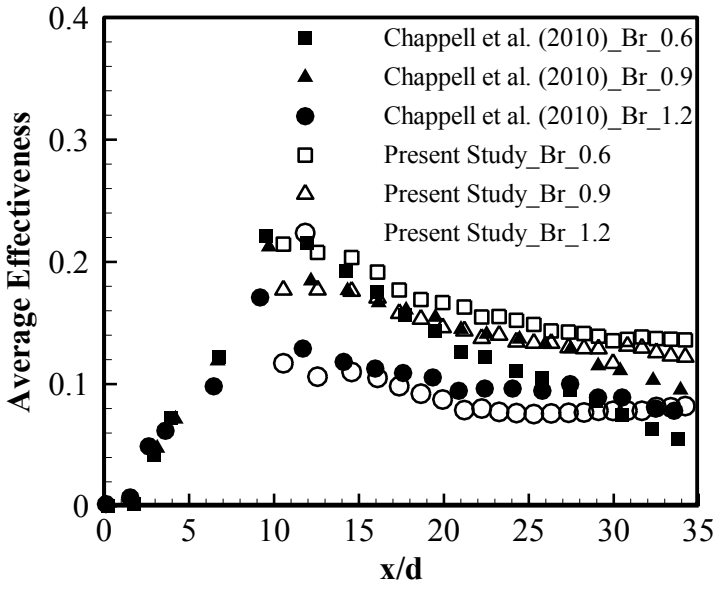

a) Laterally averaged effectiveness at different Br_b

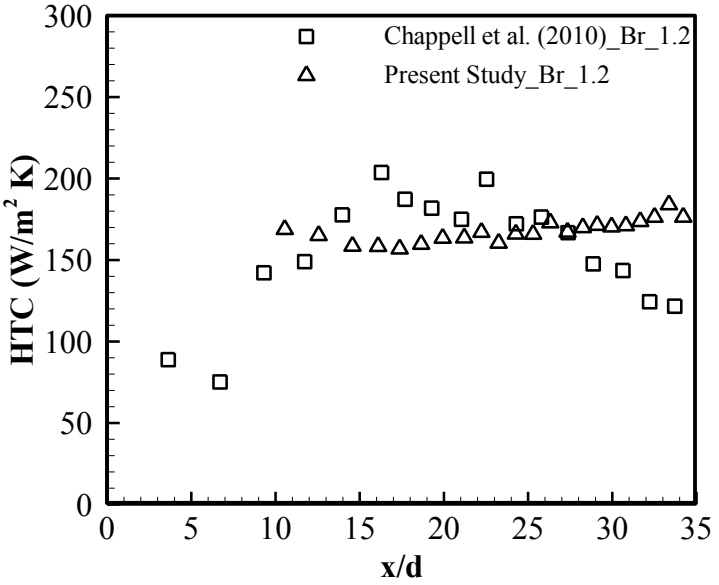

b) Heat transfer coefficient at $Br_b = 1.2$

Figure 3.9, Laterally averaged effectiveness and HTC comparison between present and reference work of Chappell et al. (2010)

3.9. Stereoscopic Particle Image Velocimetry (PIV) System

PIV is a non-intrusive flow mapping technique that uses particles immersed in the fluid to enable flow tracking. The medium is seeded with tracer particles that are sufficiently small to follow the flow closely. The basic components needed are a digital camera that captures the particles displacement at two distinct instants of time and a light source that illuminates the particles. In PIV, the displacement of particle patterns between subsequent images is determined by dividing the images into rectangular sections named interrogation areas. The displacement is found by cross correlation of corresponding interrogation areas in two subsequent recordings. Maximum correlation occurs when the particle image patterns of the two recording match best. This results in the average displacement within one interrogation area, Δx, and Δy. Since the time Δt between two subsequent recordings is known, the velocity per interrogation area can be determined. Advanced PIV codes use iterative methods to improve the accuracy by pre-shifting the interrogation areas with the displacement from a previous PIV computation.

In stereoscopic PIV, 3D PIV, two cameras record the same area from two different points of view. For each vector in a 3D vector map, the three true displacements, Δx, Δy and Δz, are reconstructed from the corresponding two dimensional displacements, Δx and Δy, from both cameras. A drawback of this setup is the mismatch between the best plane of focus, which is parallel to the image plane and the object plane. In order to overcome this drawback a Scheimpflug arrangement is used to tilt the image plane relative to the lens such that the object plane, the plane of the imaging lens, and the image plane intersect at one common line. As all other imaging techniques, calibration is essential to enable the computation of the velocity field. A well-defined calibration grid is used and images are taken with both cameras. By comparing known marker positions with corresponding marker positions on each camera image, model parameters are adjusted to give the best possible fit.

3.9.1. The PIV System

Fig. 3.10 is a schematic of the test facility with the PIV system installed. A commercial stereoscopic PIV system by Dantec Dynamics is used. The system consisted of a New Wave Research Solo XT 120 Nd:YAG dual cavity pulsed laser with a 532 nm wavelength that is capable of achieving 120 mJ/pulse at an approximate pulse rate of 15 Hz. Light sheet optics converted the single beam output into a light sheet of variable thickness. Two HiSense MkII 12 bit digital output CCD cameras, of 1344 x 1024 pixel resolution and a maximum image pair capture rate of 5.67 Hz, are employed. A Nikon objective lens, mounted to each camera, provided focal and illumination adjustments. A seeding generator containing 3 arrays of Laskin nozzles is used to seed the flow with oil aerosol of 1 μm mean diameter. Two National Instruments NI-IMAQ PCI-1426 frame grabber cards are used in conjunction with each camera to capture and store the images. A National Instruments NI-DAQ PCI-6601 timer board is used to synchronize the camera imaging with the laser pulses. A double layer target with calibrated dot spacing is used for spatial calibration. Commercial software, the Flow Manager software, is used for image processing and analysis.

The two cameras and the laser supply are installed on a traverse, Fig. 3.11. This was to facilitate the set up adjustments and ensure fixed relative distance between the cameras and the laser while changing the measurement location at any direction. A Scheimpflug arrangement is used to tilt the image plane relative to the lens plane to avoid the mismatch between the best plane of focus, which is parallel to the image plane, and the object plane. The bottom plate of the test section is painted black to reduce the light reflections and hence the measurements uncertainty. All walls that are not in front of the laser beam or the cameras lens were covered with black paper sheets for the same previous reason.

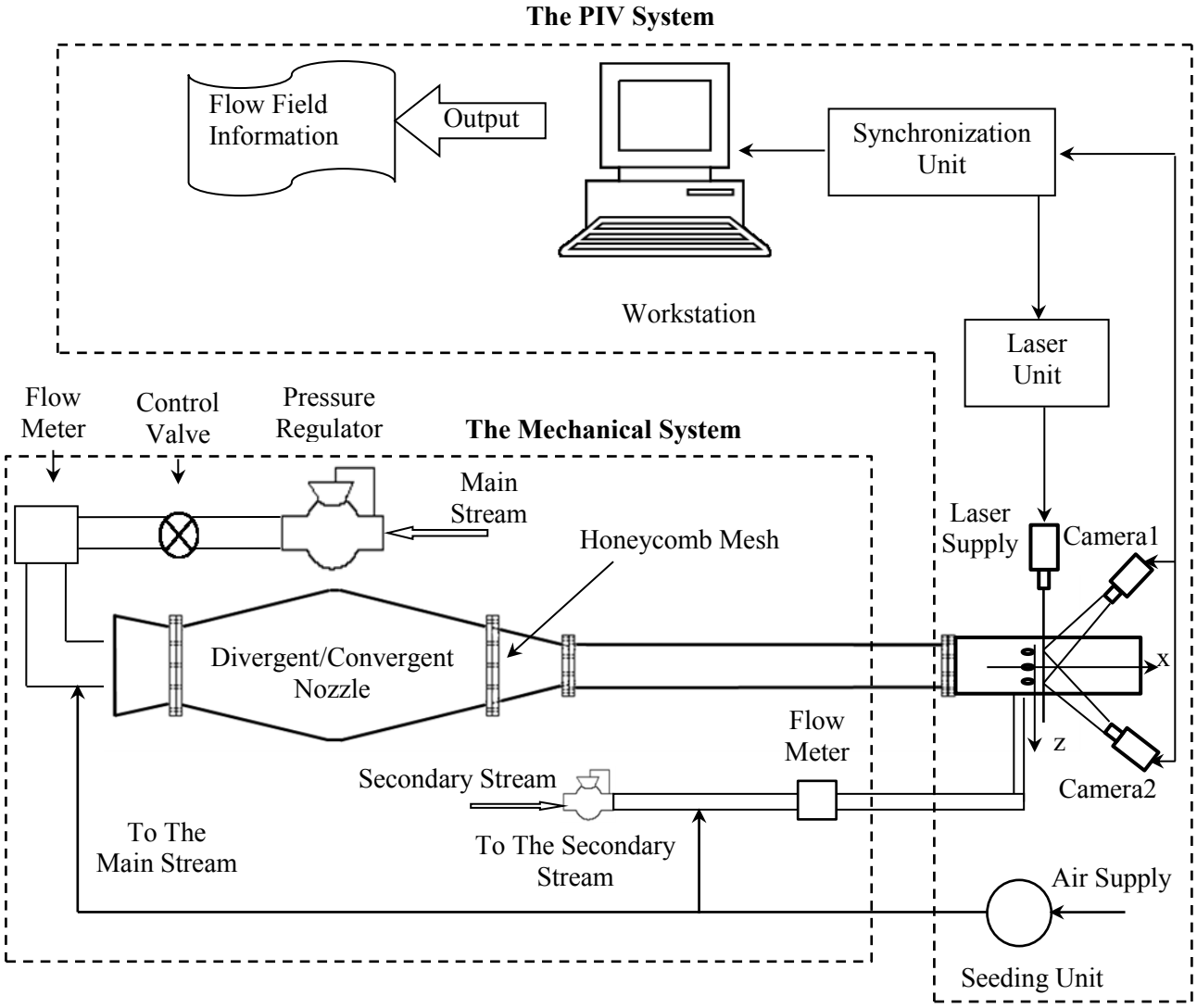

Figure 3.10, Schematic diagram of the test facility when switched to PIV investigations

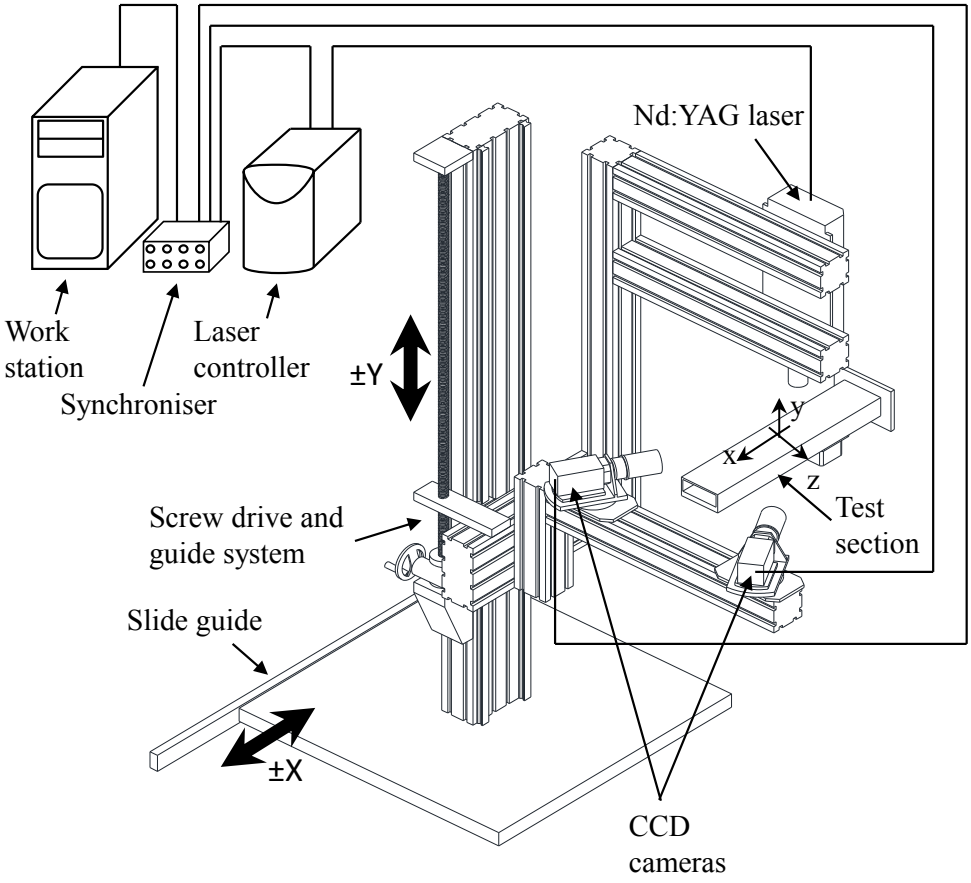

Figure 3.11, PIV system details

3.9.2. PIV Calibration

For 2D PIV measurements, a ruler is located in the camera plane of focus and an image is captured. Using this image, a scaling factor is defined to the Flow Manager software to be used with further captured images during the experiments to convert the pixel displacements to the corresponding distances in mm. For 3D measurements, a single sided double layer, rectangular calibration target, manufactured by Dantec Dynamics, is used. The dot matrix is located on a 7.5cm x 9.5cm aluminum plate, painted black, with 2 mm spacing between top and bottom layers. The dot matrix is comprised of 62 small, 3mm diameter, dots with a single large, 5mm, dot located at the center. The calibration target definition is included in the Flow Manager library as part of the Image Model Fit (IMF) algorithm. The cameras are then positioned such that their lines of sight are directed towards the target by displacing their axes by approximately 30^o from the centerline of the test section. The overlapping area between the two cameras fields of view defined the final combined field of view. The Scheimpflug arrangements of the two cameras are tilted 5^o outwards to achieve optimal images focus. The 5^o was calculated using Eq. (3.18) as follows

$$\alpha = \arctan\left(\frac{f.\tan(\theta)}{D_o - f}\right) \tag{3.18}$$

where f is the lens focal length, D_o is the distance between lens optical center and the target and θ is the mounting angle of camera body, which is 30 degree in present investigations.

In order to obtain optimal contrast between the white dots and the black background of the calibration target, local lighting is used to illuminate the calibration target surface. Two images of the calibration target, one taken from each camera, are then captured. Using the Image Model Fit (IMF) algorithm in the Flow Manager software the original image captured from each camera is

then converted to a binary black and white image. In the black and white image, neighboring pixels of identical color are grouped as objects, for example each dot corresponded to an object. The area and centroid position of each object are then calculated by the software. Objects with areas below a minimum specified value or touching the image boundary are discarded as high-frequency noise. The IMF algorithm then proceeds to recognize valid objects, or dots, from a library of standard calibration target values. This procedure results in grid, for each image, that corresponds to the relative size and orientation of the calibration target dot matrix. The image is then said to be spatially calibrated. The dual cavity laser delivers two pulses, with as low as 1 μs time interval between pulses, which are synchronized with each image pair. Two sequential images per camera are needed to produce a single vector field and these two images are referred to as the image pair. The pulse timing, *dt*, is the time interval between these two images.

3.9.3. Data Reduction

After establishing the calibration and selecting the time interval between the two images per frame, the system is said to be appropriately ready to conduct measurements. In the present study, the effect of number of frame pairs on the resulting flow field parameters was investigated and a number of 60 frame pairs was found optimal for results stability and time of processing. The post processing of images to produce vector maps is handled by the software provided by the manufacturer, the Flow Manager software. The adaptive correlation technique provides increased dynamic range and is used for data processing through the current work. A 32 x 32 interrogation area size is used throughout the analysis. A 3 x 3 pixel moving average filter is used to replace spurious vectors by a locally averaged value of neighboring vectors.

In all flow field figures, all velocity components are normalized with the average mainstream velocity across the test section without secondary stream injection, V_{avg}. The latter is calculated by dividing the volume flow rate of the mainstream by the test section cross sectional

area. Meanwhile, the total dimensionless vorticity, ω^*, is calculated by normalizing the vorticity using the scheme base diameter and the average mainstream velocity as shown in Eq. (3.19). Previous investigations, Li et al. (2011), was proven that the x-axis vorticity ω_x is the main component in the total vorticity downstream film cooling schemes, and this was proven also during the present study. However, the total vorticity is presented in all flow field figures as the main aim of the study is the vortical structure in general and not in a specific direction.

$$\omega^* = \frac{\omega}{V_{avg}/D} \tag{3.19}$$

3.9.4. Validation of PIV Measurements

The mainstream velocity distribution in the y-direction is determined using both 2D and 3D PIV measurements and compared with the analytical power law velocity distribution for fully developed turbulent flow inside ducts, Eq. (3.20), Munson et al. (2006),

$$V(y) = V_c\left[1 - \left(\frac{y}{h/2}\right)\right]^{1/n} \tag{3.20}$$

where V_c is the centerline velocity at the centerline of the test section in the y-direction that is determined using Eq. (3.21). h, is the test section height, 54mm for the current test section. And n, is a polynomial coefficient and determined based on the mainstream Reynolds number, Munson et al. (2006). For the 1.16E5 Reynolds number applied throughout this study, the exponent n was found about 7.3.

$$V_c = \frac{V_{avg}(n+1)(2n+1)}{2n^2} \tag{3.21}$$

Figure 3.12 is the mainstream velocity ratio comparison between experimental measurements and analytical calculations. From the figure, good agreement between the experimental, 2D and 3D, measurements and the analytical predictions is noticeable. Moreover, for y/d < 0.4, the agreement between theoretical predictions and 2D measurements is better than the agreement between theoretical predictions and 3D measurements. The latter is a result of a limitation accompanying 3D measurements. The 3D calibration target used during the current study is manufactured with large dots diameter and wide dots distribution. In order to be able to capture on image sufficient number of dots for calibration, a minimum distance between the cameras and the imaging plane must be maintained. This is not the case with 2D measurements as there is not a minimum distance that should be maintained between the camera and the imaging plane.

Figure 3.13 is the 3D velocity distributions downstream a circular hole scheme in the present work and the reference, Bernsdorf et al. (2008), work at two different blowing ratios. In the figure, the color contours represents the main, x-axis, velocity component and the vectors represent the in-plane velocities, *v* and *w*. The only geometrical difference between the present scheme and the reference one of Bernsdorf et al. (2008) is the inclination angle of the scheme. Throughout the present study an inclination angle of 35^o was used while Bernsdorf et al. (2008) used a 30^o one. The value of the inclination angle affects mainly the timing of jet lift off, and the distance that the jet lifts away from the surface. From Figs. 3.13a and b, good agreement is noticeable between the velocity distributions of the present study and the reference work at Br_b = 1.0 and Br_b = 2.0. Minor differences in the velocity distribution at the jet core area are observable

at Br_b = 1.0, Fig 3.13a. The latter is attributed to the effect of the inclination angle, as jet lift off starts to appear at Br_b = 1.0 with the 35^o inclination angle case. The jet downstream the 30^o inclination angle scheme shows better attachment capabilities at Br_b = 1.0. At Br_b = 2.0, the effect of jet lift off more pronounced than Br_b =1.0. The distance between the jet core and the surface of the 35^o scheme is larger than the corresponding distance of the 30^o scheme. However, the same main velocity contours and in-plane velocity vectors distributions are observable between present and reference results. This confirms the validity of the present facility and methodology for flow field investigations.

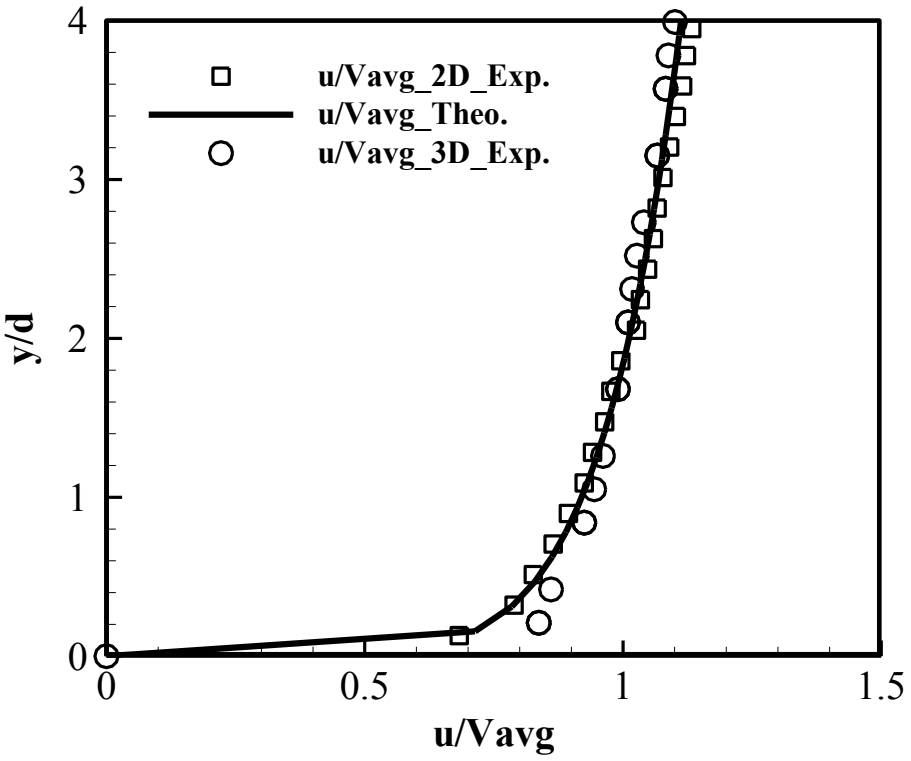

Figure 3.12, Experimental 2D and 3D velocity comparison with theoretical

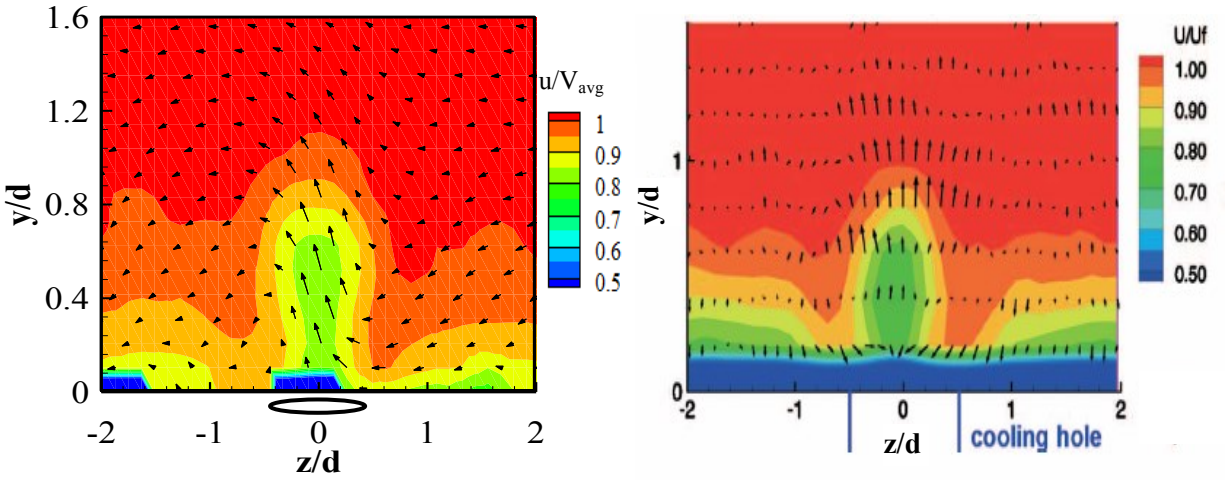

a) $Br_b = 1.0$

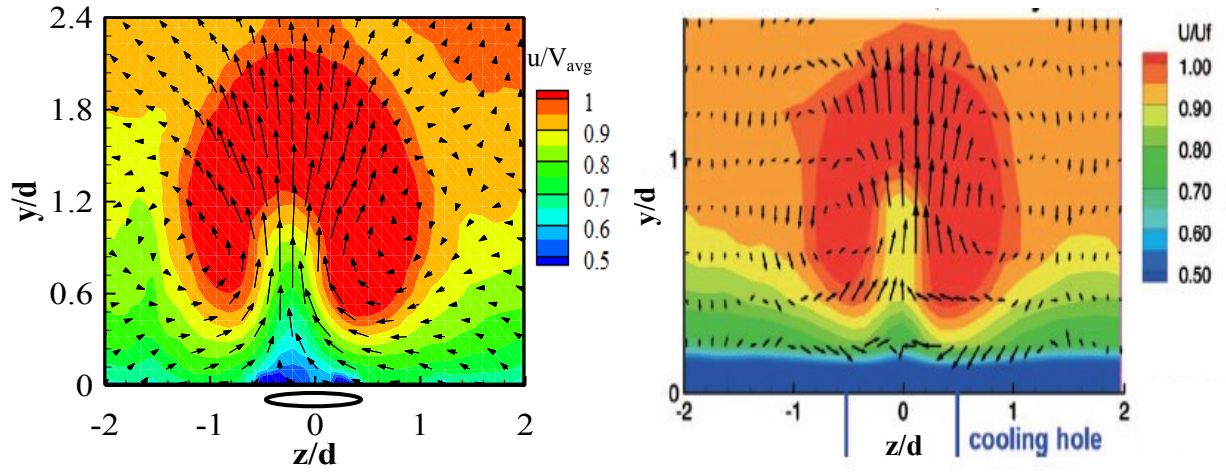

b) $Br_b = 2.0$

Present Work Bernsdorf et al. (2008)

Figure 3.13, 3D velocity distribution comparison between present work and the work of Bernsdorf et al. (2008) downstream a circular hole scheme at x/d = 4.0

Chapter 4

Film Cooling Performance of the Micro-Tangential-Jet Scheme; Effectiveness

4.1. The Micro-Tangential-Jet (MTJ) Film Cooling Scheme

The MTJ scheme, Fig. 4.1a, is a new film cooling scheme designed in a way to combine micro-film cooling and tangential injection together to achieve optimal film cooling performance. The scheme consists of two main parts, a circular supply micro-tube and a shaped exit parallel to the vane surface. The shaped exit of the scheme starts with a circular cross section. Lateral expansion angles are then applied in both directions and a relatively constant height is maintained throughout the scheme yielding a squared exit. The purpose of the lateral expansion angle is to speed-up the formation of a continuous film close to the injection location. The geometrical ratios and locations of the MTJ scheme on both pressure and suction sides are presented in Table 1. Applying tangential injection to actual airfoil surfaces is limited due to the expected aerodynamic losses resulting from adding excess material on the airfoil surface. With the aid of micro-film cooling and by carefully selecting the location of the scheme on the surface such added material could be kept at a minimum. The selected scheme height in this study is 600 μm. This height is relatively large but this is very close to the minimum height that can be manufactured with an acceptable accuracy using the available manufacturing techniques.

The performance of one row of holes of the MTJ scheme is investigated at three different blowing ratios on the pressure side; 0.5, 1.0 and 1.5, and four different blowing ratios on the suction side; 0.25, 0.375, 0.5 and 0.625. The total number of holes on the pressure side is 13

Table 4.1, MTJ scheme geometrical properties

	Location (% X/Cx)	Base diameter (d, μm)	Length (L)	Width (W)	Height (S)	Lip thickness (t)	Pitch (p)	lateral angle (α)
Pressure side	7.5	600	2.5d	3d	1d	0.35d	5d	23
Suction side	38.3	600	2.5d	4d	1d	0.35d	6.5d	32.5

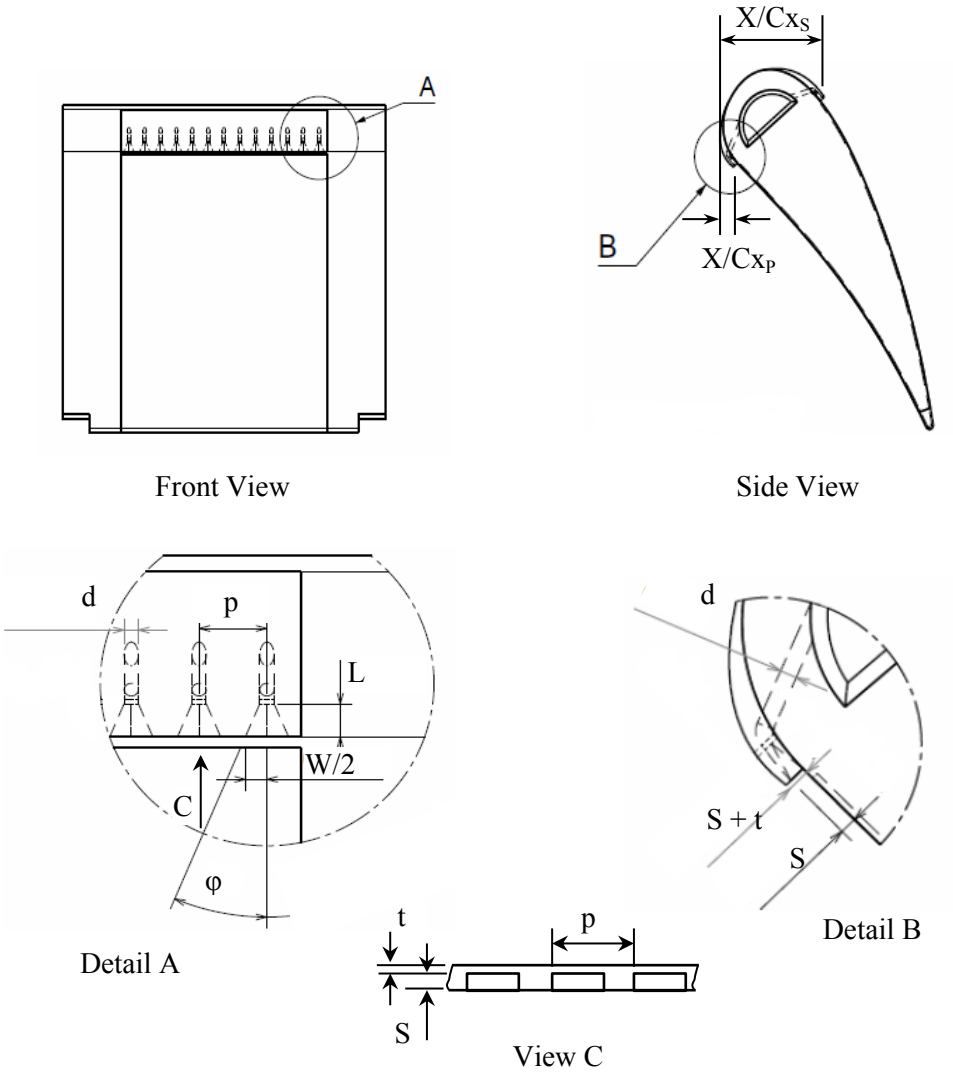

a) The Micro-Tangential-Jet Scheme

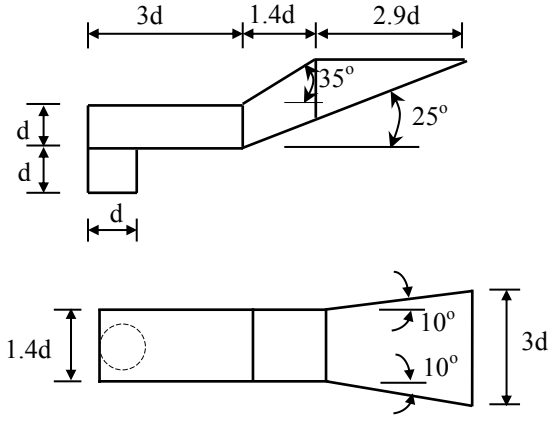

b) The Louver scheme

Figure 4.1, Micro-Tangential-Jet and Louver schemes geometrical details

while the total number of holes on the suction side is 11. For the performance of the MTJ scheme to be compared with that of normal shaped schemes, the performance of one row of the louver scheme, Fig. 4.1b, is investigated on both pressure and suction sides of the same airfoil. The louver scheme is a normal shaped scheme with internal 90^{o} bend that combines the benefits of impingement cooling upstream the injection location to the enhanced film cooling benefits of shaped schemes in the area downstream of it. The louver scheme showed enhanced film cooling performance, compared to other shaped schemes, when investigated over an airfoil vane pressure and suction sides, Elnady et al. (2010). In order to limit the number of variables to the effect of the scheme exit shape only, the coolant amounts supplied to the louver scheme are the same as those supplied to the MTJ scheme to cover the same spanwise area of the airfoil surface.

4.2. Mach Number Distribution Around the Vane Surface

The effect of the MTJ scheme on the flow characteristics around the vane surface is investigated. Two pressure vanes, Fig. 3.2b, are manufactured for this purpose, one with the MTJ scheme on both pressure and suction sides and the other without. Fig. 4.2 is the Mach number comparison between the two cases. It is clear from the figure that the maximum distortion in the Mach number distribution due to the presence of the MTJ scheme is less than 10% and is limited to the area surrounding the scheme exit on the suction side only. Furthermore, there is no change in the Mach number distribution on the pressure side. The small height of the MTJ scheme is the main contributor to such performance. The MTJ scheme exit location on the pressure side is very close to the stagnation line, X/Cx = 7.5%, and the flow velocity in this region is small. The effect of the added material on such small velocity is small as well. Contrarily, on the suction side the location of the MTJ scheme exit is at X/Cx = 40% and the velocity is high at this region and as a result, the added material results in instantaneous change in the velocity. After passing the region

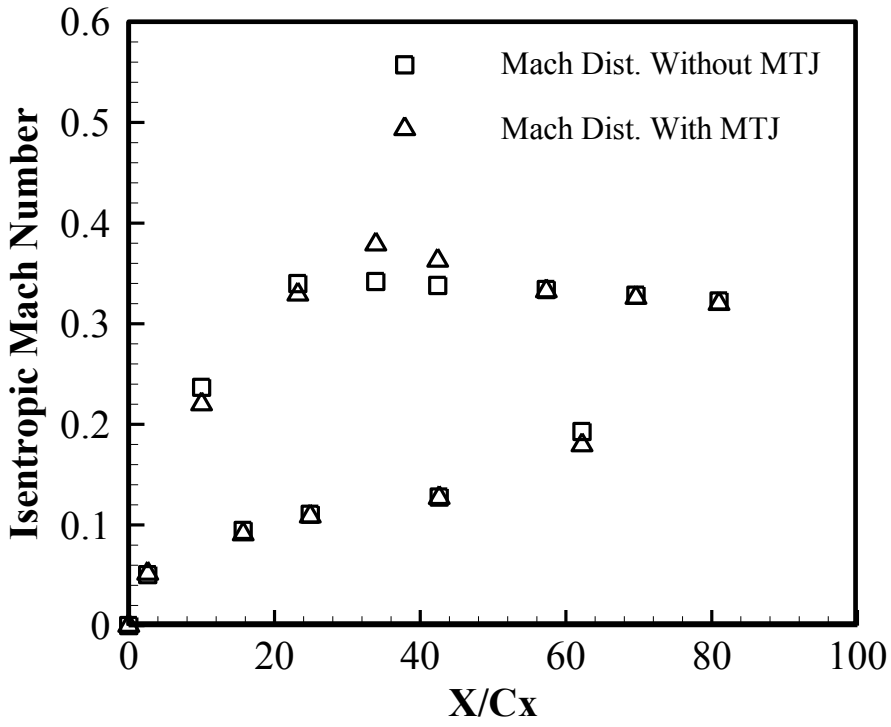

Figure 4.2, Mach number distribution around the vane surface, with and without MTJ scheme

of the scheme exit on the suction side, the velocity returns back to its normal distribution.

4.3. Pressure Side Film Cooling Effectiveness

In general, the MTJ scheme showed great effectiveness performance on both pressure and suction sides. High effectiveness values for long downstream distances and excellent lateral jet spreading are recorded. Figure 4.3 is the film cooling effectiveness contours of the MTJ scheme compared to the corresponding contours of the louver scheme at the same blowing ratios. The amount of coolant supplied to the louver scheme is the same as that supplied to the MTJ at certain blowing ratio. The aim was to consider a certain spanwise area that is being covered by the coolant from the MTJ schemes, and compare it to the corresponding area that is covered by the louver schemes. A number of five MTJ holes and four louver holes was the optimal selection. This is why, only five holes in the region around the mid-span of the surface, from the thirteen holes of the pressure side, are considered during this study. The high pressure on the pressure side and the lateral expansion angles of the scheme help combining the separate jets from separate holes and perform a continuous film after a short distance from the injection location. For blowing ratios 0.5 and 1.0, Figs. 4.3a and b, the contours looks if they are resulting from a continuous slot scheme; however, at blowing ratio 1.5, small traces of separate jets appears in the region of $x/d < 10$. The latter is a result of the increased secondary jets momentum. As a result, the coolant jet is concentrated more in front of the scheme exit and hence increases the cooling effect in this region more than the regions between adjacent jets. It is also noticeable that the variation in effectiveness contours in the region close to the scheme exit is negligible when increasing the blowing ratio; however, for $x/d > 10$ the increase in the effectiveness with blowing ratio increase is noticeable.

By comparing the contours of the louver and the MTJ schemes, the difference between

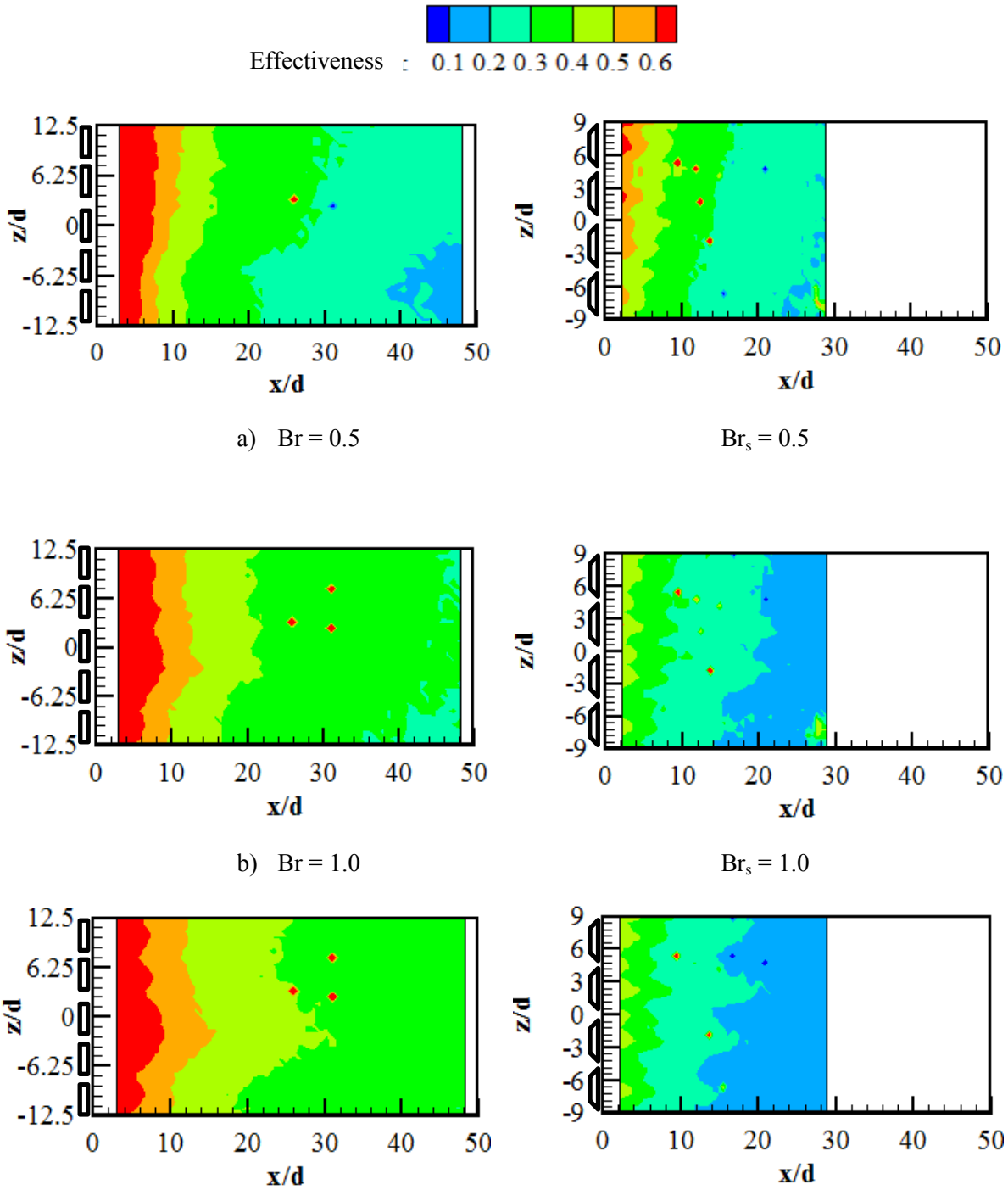

a) Br = 0.5 Br_s = 0.5

b) Br = 1.0 Br_s = 1.0

c) Br = 1.5 Br_s = 1.5

MTJ Scheme Louver Scheme

Figure 4.3, Pressure side effectiveness contours for the MTJ and the Louver schemes at different blowing ratios

both is noticeable from many points. First, the effectiveness values, especially at high blowing ratio, the effectiveness of the MTJ scheme is more than twice that of the louver scheme. Second, the penetration depth, as the MTJ jets penetrate deeper than those of the louver scheme. Third, the trend of the effectiveness change when the blowing ratio is changed. The effectiveness increases in the case of MTJ scheme by increasing the blowing ratio; however, it decreases with the louver scheme with blowing ratio increase. The increased effectiveness in the case of the MTJ scheme by increasing the blowing ratio is expected as it is due to the increased coolant amount with the absence of jet-lift off. In the case of the louver scheme, the coolant amounts supplied throughout the current study are higher than the corresponding quantities usually supplied under the same blowing ratios. This is a result of using the same coolant amount principle; the amount of coolant supplied to the louver scheme is the same as the corresponding amount supplied to the MTJ scheme at certain blowing ratio. Usually, the coolant amounts supplied to a shaped scheme are the same as those supplied to a circular hole scheme with the same base diameter. Based on this, the coolant amounts currently supplied to the louver scheme corresponds to Br_b of 1.0, 2.0 and 3.0. Previous investigations showed that a Br_b close to 1.5 is optimal for the louver scheme with its present geometrical ratios. When increasing the blowing ratio beyond this value the performance starts to be reversed. This explains why the louver scheme showed reversed effectiveness trend with blowing ratio increase.

Figure 4.4 presents the centerline and the spanwise-averaged effectiveness performance of the MTJ scheme with dimensionless downstream distance, x/d. From the figure, the area downstream the scheme exit could be divided into three regions, based on the rate of decay in the centerline and spanwise-averaged effectiveness. The first region starts directly after the scheme exit and up to x/d = 10. In this region, sudden reduction in the effectiveness is observed. This could be related to the increased turbulence resulting from the vortices generated behind the scheme lip and those resulting from the velocity gradient between the jet and the main stream.

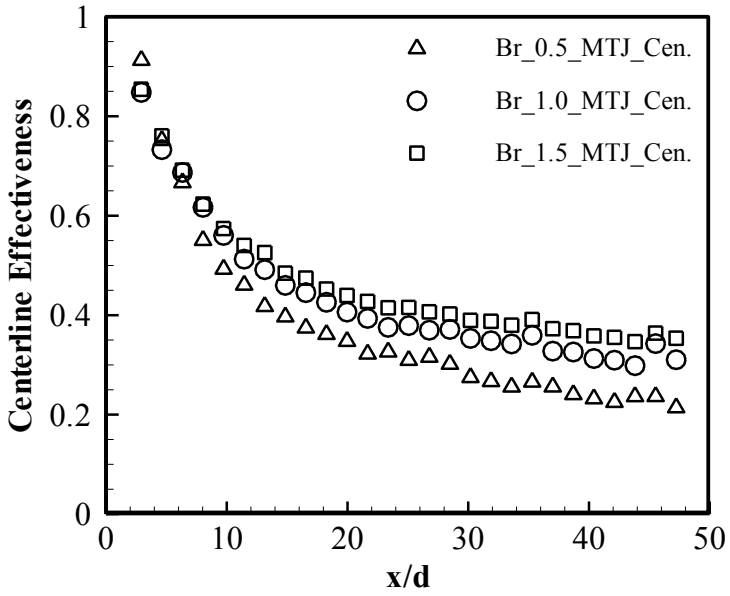

a) Centerline effectiveness

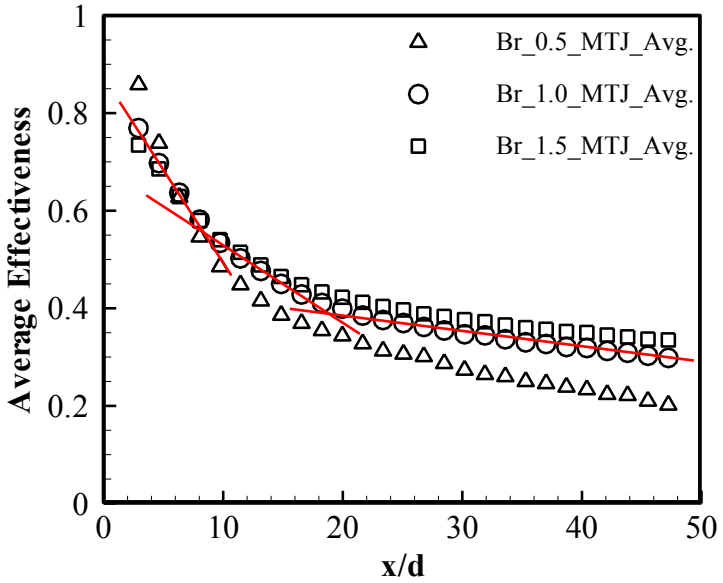

b) Spanwise-averaged effectiveness

Figure 4.4, Pressure side centerline and spanwise-averaged effectiveness comparison at different blowing ratios

The second region starts from x/d = 10 and up to x/d = 20, and is characterized by a moderate rate of effectiveness decay. In this region, the effect of the vortices generated behind the scheme lip is almost vanished and the vortices generated by the velocity gradient between the two streams are dominant. The last region starts at x/d = 20 and up to the end of the region of interest. This region is characterized with a very small rate of decay in the effectiveness. Away of the injection location and once the uniform 2-D film is developed the rate of mixing between the jet and the main stream is very low because the vortices generated behind the scheme lip and those resulting from the velocity gradient become very weak. It is also noticeable from Fig. 4.4 that the rate of effectiveness enhancement with increasing the blowing ratio from 1.0 to 1.5 is less than that resulting from increasing the blowing ratio from 0.5 to 1.0. With the absence of jet lift off, the effectiveness is expected to increase all the time by increasing the blowing ratio due to the increased coolant amount. Such relation is non-linear; because the increase in the coolant amount is accompanied with enhanced vortex structure downstream the injection location. This in turn increases the mixing between the two streams. When the blowing ratio increases from 0.5 to 1.0, the gain in effectiveness of the increased coolant amount is higher than the loss resulting from the strengthened vortices; however, with the blowing ratio increase from 1.0 to 1.5, the gain in effectiveness of the increased coolant amounts is less than the loss resulting from the strengthened vortices.

The previously mentioned performance is supported with the results of the flow visualization study downstream the MTJ scheme presented in chapter 6 of the present study. The flow field visualizations showed that; as blowing ratio increases, the strength of the vortex structure downstream the MTJ scheme significantly increases. The enhanced vortices affect the scheme performance from two points; first, they enhance the mixing between the main and the secondary streams and hence reduce the effectiveness, and second, they enhance the HTC performance and reduce the overall scheme performance. The main contributor to the enhanced

mixing between the two streams is the vortex generated in the shear layer between the two streams.

By comparing the performance of the MTJ scheme and that of a continuous slot scheme, many points of similarity are observed. Stollery and El-Ehwany (1965) divided the area downstream the injection slot into three regions. The first is a very small region named the potential core region at which the wall temperature is almost the same as the jet temperature and the effectiveness is close to unity. In the second region, the flow characteristics are very close to those of a wall-jet flow. And far downstream the flow is very close to a normal fully developed boundary layer flow. The first region is not so clear in the present study because there is a gap of about three hole diameters distance between the MTJ scheme exit and the beginning of the region of interest because of the TLC sheet installation limitations. The second region, sometimes referred to as the mixing region, is clear in the case of the MTJ scheme and starts from the beginning of the region of interest and up to x/d of about 20. Supplying the secondary stream as separated jets in the case of the MTJ scheme increases the area of interaction between the two streams and hence the rate of mixing between them, compared to continuous slot schemes. The third region, the 2-D film region is very similar between the two schemes, the MTJ and the continuous slot schemes, because of the similarity in the flow characteristics in this region. This is also observable from the PIV measurements. The region very close to the injection location is characterized with high secondary stream velocity and enhanced turbulence. With increasing downstream distance, the rate of turbulence decays and separate jets join together and perform a continuous film. Far downstream, the flow is very close to normal boundary layer flow.

One important observation from Figs. 4.3 and 4.4 is the penetration distance of the MTJ jets. The presented values of the x/d is about 50 and the effectiveness values at the end of the region of interest are still close to those at x/d = 15. This means that the generated film is maintained in the downstream direction. This was also observed visually during the experiments;

however, the view angle of the camera did not allowed imaging after x/d = 50. The small height of the jet, the micro height, is the main contributor in this case. Although the 600μm slot height is not very small, it showed excellent performance from jet penetration point of view. Gau et al. (2009) stated that a micro jet is characterized by the absence of the boundary vortices accompanying macro jets which allows it to penetrate deeper in the main stream than macro jets. Consequently, it is expected that decreasing the slot height would give better results from jet penetration point of view. The plan was to investigate smaller slot heights; however, due to manufacturing limitation a height of 600μm was selected as a start point to this research work.

Figure 4.5 is the local spanwise effectiveness comparison downstream the MTJ scheme at different streamwise locations and different blowing ratios. From the spanwise effectiveness comparison at x/d = 3 at different blowing ratios, it is noticeable that increasing the blowing ratio affects the uniformity of the coolant film in the spanwise direction. The latter results in more concentrated coolant amount in the region in front of the scheme exit due to the increased jet momentum in the streamwise direction. Meanwhile, the amount of coolant directed towards the intermediate locations between adjacent jets does not change too much with blowing ratio increase. At x/d = 20, the uniformity in the 2-D film is clear at all blowing ratios and it is clearer with high blowing ratios. It is observable that the rate of jet decay decreases by increasing the blowing ratio as a result of the enhanced jets strength due to the increased coolant amount.

The quantitative enhancement in the effectiveness performance of the MTJ scheme compared to the louver scheme at Br = 1.0 is clear from Fig. 4.6. The centerline and spanwise-averaged effectiveness of the MTJ scheme are twice as those of the louver scheme, all over the streamwise area, Fig. 4.6a. This is confirmed from the spanwise effectiveness comparison of Fig. 4.6b as the spanwise effectiveness values for the louver scheme at x/d = 3 are the same as those of the MTJ scheme at x/d = 20. This shift in performance between the two schemes is attributed to the direction of secondary jet injection. Supplying the secondary jet with an angle with the main

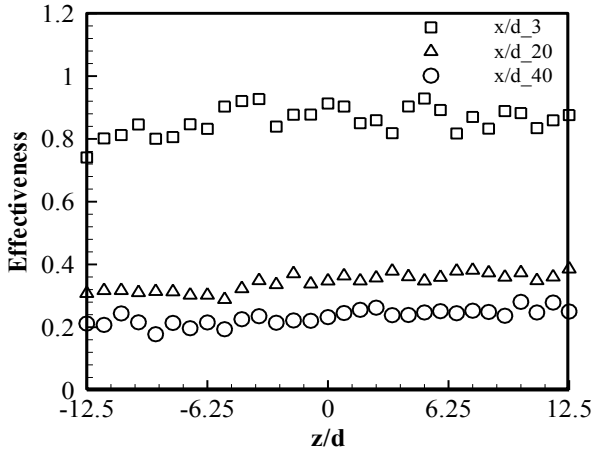

a) Br = 0.5

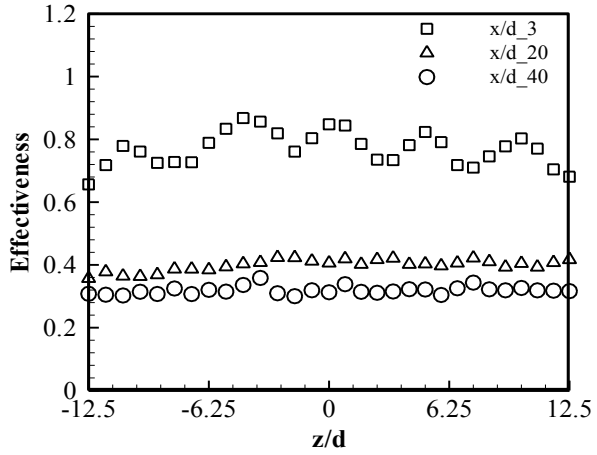

b) Br = 1.0

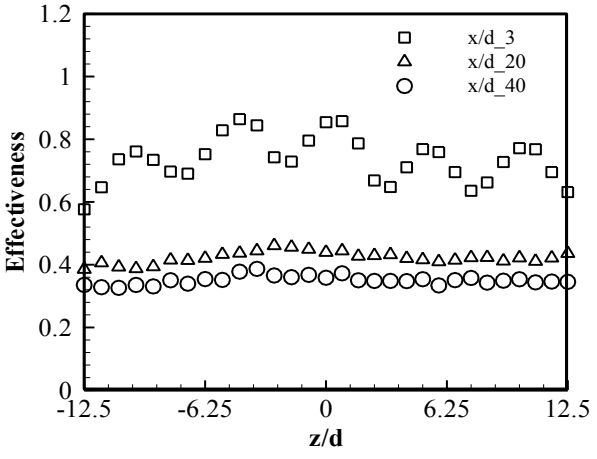

c) Br = 1.5

Figure 4.5, Pressure side spanwise effectiveness for the MTJ scheme at different streamwise locations

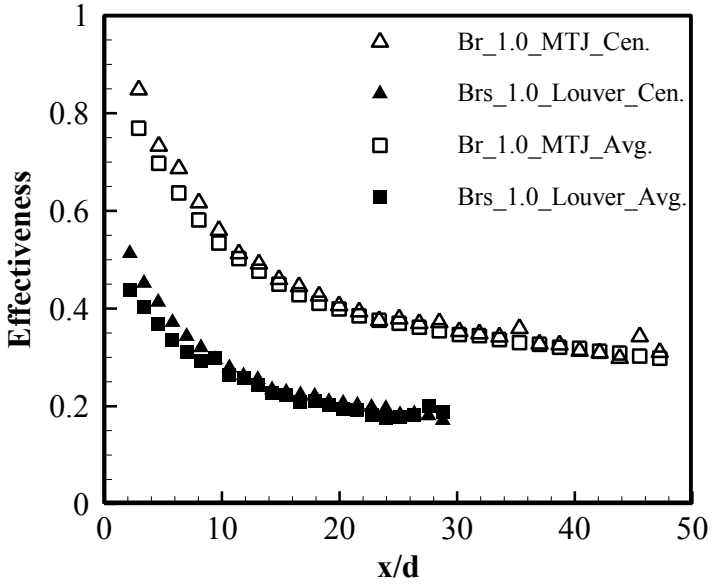

a) Streamwise direction

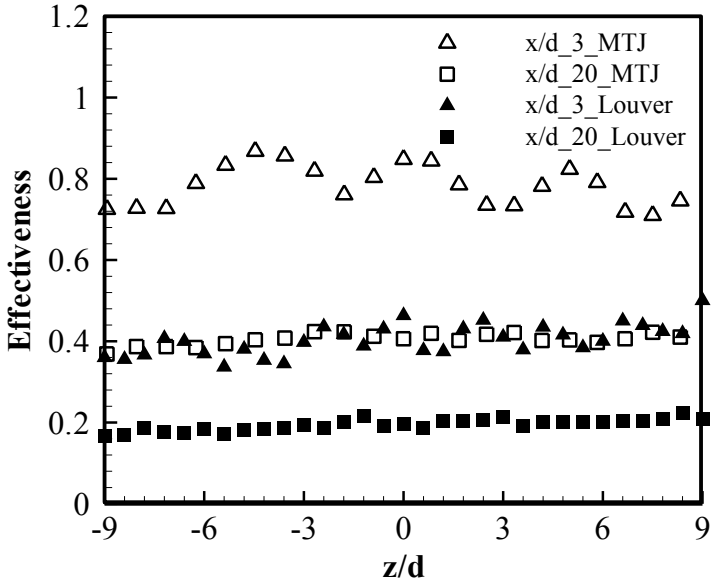

b) Spanwise direction

Figure 4.6, Pressure side, streamwise and spanwise effectiveness comparisons between MTJ and louver schemes at Br (MTJ) and Br_s (louver) = 1.0

stream direction, results in strong Counter Rotating Vortex pair (CRVP). This in turn enhances the mixing between the two cross streams. The flow visualization study showed the presence of a weak CRVP, compared to the circular hole scheme case, downstream the MTJ scheme. However, the vortex generated in the shear layer between the two streams in the case of the MTJ scheme is expected to be the main contributor on the film cooling performance of the scheme.

4.4. Suction Side Film Cooling Effectiveness

The performance of the MTJ on the suction side was investigated at four blowing ratios calculated based on the scheme exit area. The MTJ scheme design on the suction side is the same as that on the pressure side except for the width of the scheme exit; it is 4d on the suction side and 3d on the pressure side. The low pressure on the suction side helps the secondary stream to penetrate deeper distances in the main stream than the pressure side; however, it decreases its lateral spreading capabilities. Changing the width of the scheme exit affects the jet lateral spreading, the wider the exit the better the lateral spreading. Due to high velocities on the suction side, and since the blowing ratio is being calculated based on the exit area of the scheme, the minimum selected blowing ratio is 0.25 and the maximum is 0.625. During the experiments it was difficult to supply blowing ratios more than 0.625 because of the high pressure drops inside the scheme supply micro tubes. Here again, the louver scheme is used for comparison purposes to show the enhancement in the effectiveness of the MTJ scheme compared to traditional inclined angle shaped schemes.

Figure 4.7 is the film cooling effectiveness contours comparison between the MTJ and the louver schemes. In the figure, the performance of four MTJ holes is compared with the corresponding performance of three louver holes, to cover the same spanwise area. The contours show great performance for the MTJ scheme, high effectiveness values and excellent lateral

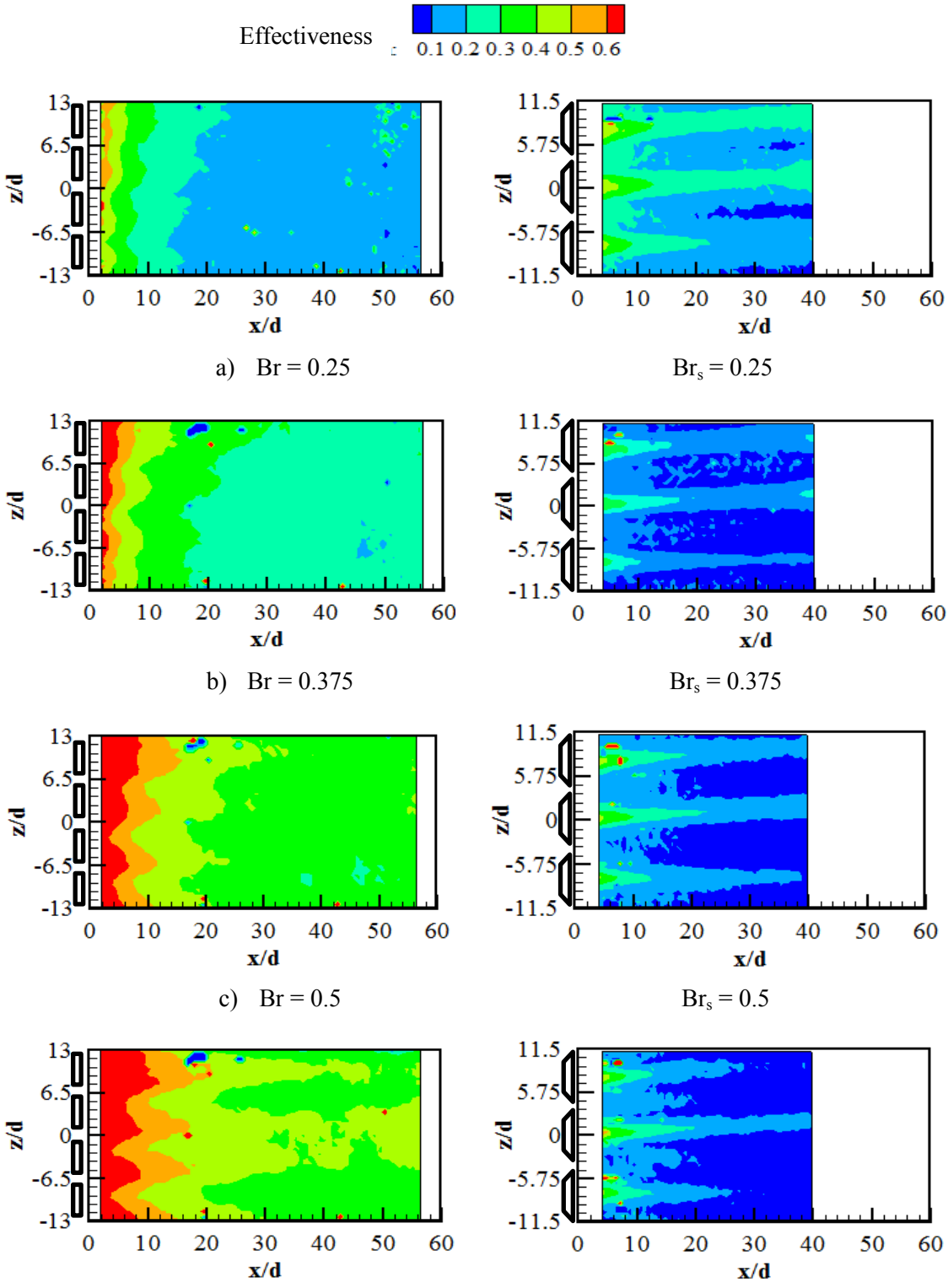

Figure 4.7, Suction side effectiveness contours for MTJ and Louver schemes

coverage. Similarly to the pressure side, as the blowing ratio increases, the inertia of the jets increases. The latter results in relatively concentrated coolant amount in front of the scheme exit, compared to the areas between adjacent jets. Which in turn enhance the effectiveness in front of the injection locations than the intermediate regions between adjacent jets. It is also noticeable that, the effectiveness downstream the MTJ scheme is enhancing with blowing ratio increase. However, and for the same reason mentioned in the case of the pressure side, the louver scheme showed reversed performance with increasing blowing ratio. It was mentioned in the case of the pressure side that a blowing ratio around 1.5 resulted in optimal effectiveness performance, for the current louver scheme exit dimensions. Since the pressure over the suction side is lower than that over the pressure side, a blowing ratio less that 1.5 is expected to be optimal. Beyond that blowing ratio, jet lift off appears and reversed effectiveness performance is expected. The currently supplied coolant amounts to the louver correspond to Br_b of 1.3, 2.0, 2.7, and 3.3, based on the scheme base diameter. This means that, the 1.3 blowing ratio, or the 0.25 one based on the current calculation method, is the optimal blowing ratio or close to the optimal blowing ratio. This explains why the effectiveness decreases with increasing blowing ratio with the louver scheme. Significant differences in the lateral jet spreading are also noticeable from the Fig. 4.7. In front of the louver scheme very clear jet traces are observable. Meanwhile, such traces are limited to a very short distance in front of the injection location downstream the MTJ schemes.

The centerline and spanwise-averaged effectiveness at different blowing ratios are shown in Fig. 4.8. The effectiveness increases as the blowing ratio increases; however, the rate of effectiveness increase slows down when the blowing ratio changes from 0.5 to 0.625. Due to the difficulty in applying blowing ratios beyond 0.625 it is difficult to judge if the decreasing rate of effectiveness improvement is due to the increased mixing between the two streams or due to some other factors. Different from the pressure side, the effectiveness on the suction side starts

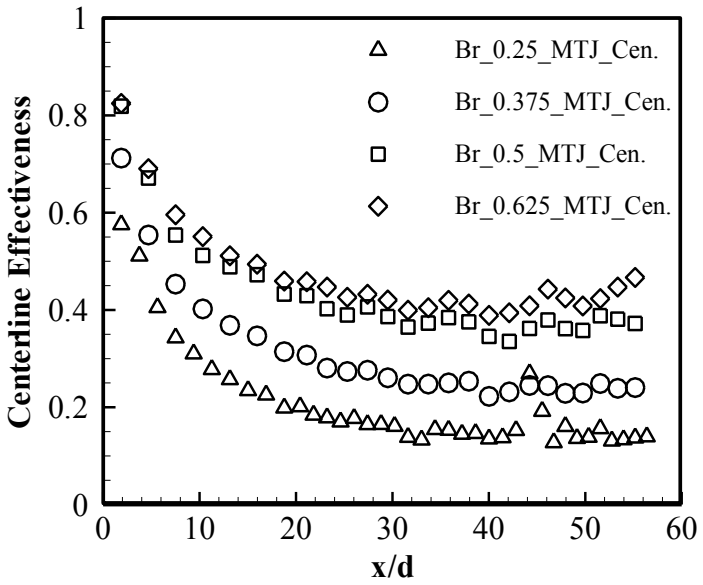

a) Centerline Effectiveness

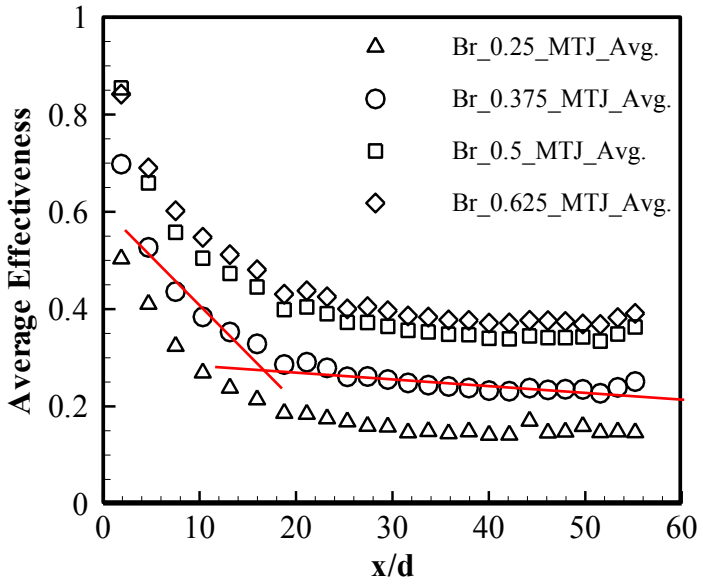

b) Spanwise-averaged Effectiveness

Figure 4.8, Suction side centerline and spanwise-averaged effectiveness comparison at different blowing ratios

increasing from the scheme exit till the end of the region of interest. On the suction side the pressure is low and as a result the attachment of the main stream on the surface is very weak. With the secondary stream being injected parallel to the surface the rate of mixing between the two streams is at minimum. On the suction side, the area downstream the scheme exit could be divided into two regions, instead of three as the case of the pressure side. The first region, is characterized with a high rate of effectiveness decay and this is the region directly after the scheme exit until x/d = 20. This region is the mixing and advection region in which the vortices behind the scheme lip and those resulting from the velocity gradient between the two streams are strong. The second region is between x/d > 20 till the end of the region of interest. The latter is characterized with a very low rate of effectiveness decay. This gives an indication that a 2-D film is performed and the rate of mixing between the two streams is at minimum. The reduced mixing rate is also a result of the low pressure on the suction side and the tendency of the mainstream to lift off the surface. The trend of performance observed in Fig. 4.8 for the MTJ scheme is not unique and it is observed with the louver scheme as well. This means that the flow characteristics over the suction side are the main contributor to such performance.

Figure 4.9 is the spanwise effectiveness comparison for the MTJ scheme at different streamwise locations and blowing ratios. The performance at Br = 0.625 is not presented in the figure because it is almost the same as that of Br = 0.5. It is noticeable from the figure that the fluctuations in the spanwise effectiveness distribution at x/d = 4 increase as the blowing ratio increases which is expectable due to the increased jet momentum. Meanwhile, a reduction in the effectiveness values is noticeable with moving from positive spanwise location to negative side. The latter is a result of non-uniform secondary jet distribution across the schemes as a result of the pressure drop inside the schemes supply micro tubes. The effect of pressure drop increases with blowing ratio increase due to the increased coolant amount.

The quantified enhancement in the effectiveness performance of the MTJ compared to that

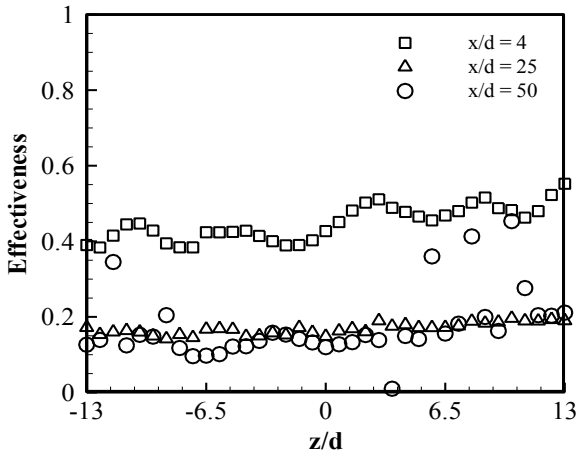

a) Br = 0.25

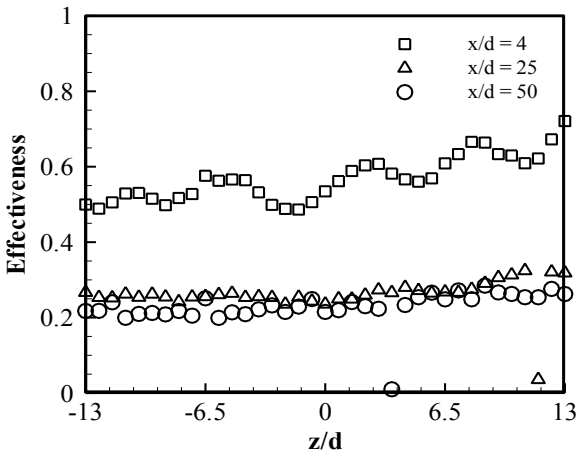

b) Br = 0.375

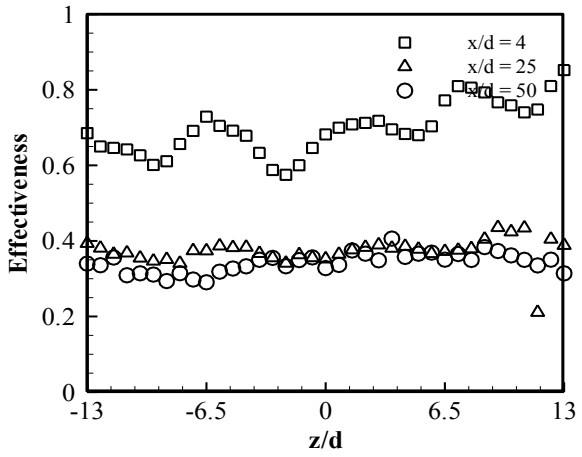

c) Br = 0.5

Figure 4.9, Suction side spanwise effectiveness for the MTJ scheme at different streamwise locations

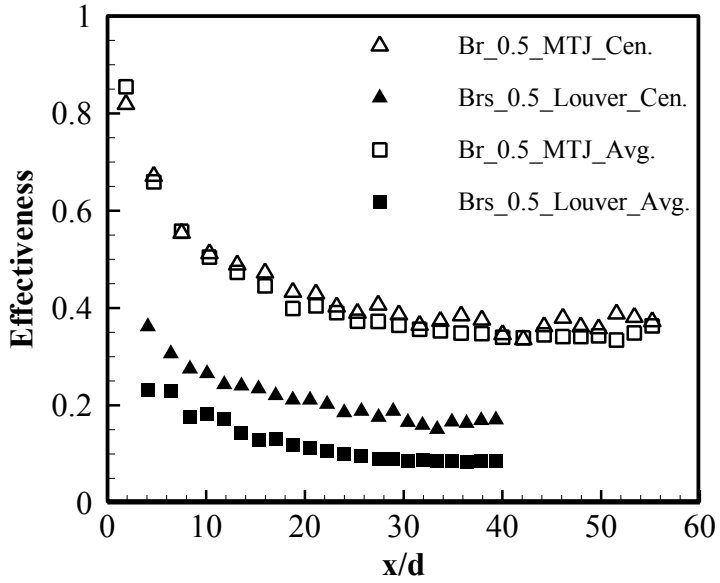

a) Streamwise direction

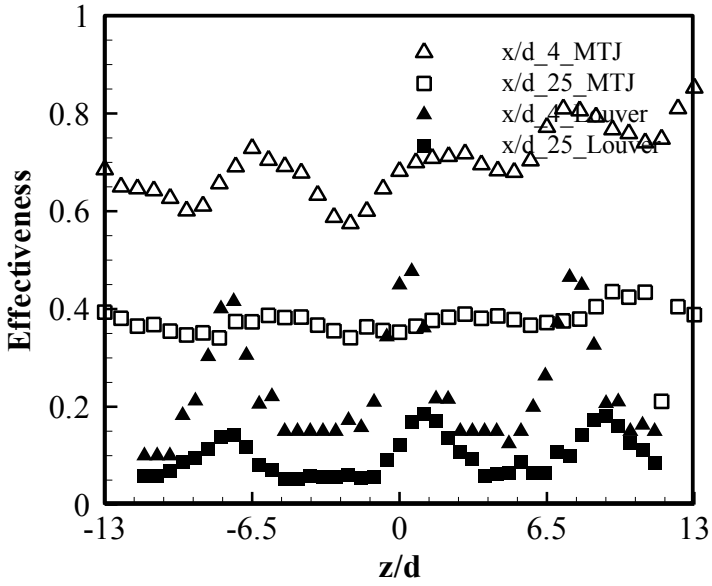

b) Spanwise direction

Figure 4.10, Suction side, streamwise and spanwise effectiveness comparisons between MTJ and louver schemes at Br (MTJ) and Br_s (louver) = 0.5

of the louver scheme is clear in Fig. 4.10. In the figure, the streamwise and spanwise effectiveness comparison between the MTJ and the louver schemes at blowing ratio 0.5 are presented. The effectiveness values at the end of the region of interest in the case of the MTJ scheme equal the maximum effectiveness at the beginning of the region of interest in the case of the louver scheme. Besides, the enhanced effectiveness is accompanied with lateral spreading enhancement which helps reduce the thermal stresses. This is clear from both streamwise and spanwise effectiveness distributions, Figs. 4.10a and b, respectively.

4.5. Comparison With Previous Work

The works of Chappell et al. (2010), Waye and Bogard (2007), Colban et al. (2006) and Dittmar et al. (2003) were found comparable to the present study. The comparison between the present study and the previous works is carried out at the minimum and the maximum blowing ratios applied in each study. This represents the limits of the achieved effectiveness by the proposed schemes. The suction side spanwise-averaged effectiveness comparison between one row of the MTJ schemes (the present study), two rows of axial fan-shaped schemes (Chappell et al. (2010)), and one row of circular hole schemes impeded in a narrow trench (Waye and Bogard (2007)), are presented in Fig. 4.11. It was mentioned earlier that the blowing ratios calculated for the MTJ scheme were calculated based on the scheme's exit area while those in the reference studies were calculated based on the scheme base diameter. As a result the values of blowing ratios applied during this study with the MTJ scheme are small compared to those applied in previous studies. When the performance of the MTJ scheme at Br = 0.25 is to be compared with the performance of other schemes at low blowing ratio, Fig. 4.11a, the one row of the MTJ scheme showed better film cooling effectiveness performance than the two rows of the axial fan-shaped schemes and comparable performance to the narrow trench scheme. Based on this, it

could be concluded that at low blowing ratio the MTJ scheme shows comparable performance to the previously proposed shaped schemes. At Br = 0.375 and Br = 0.625, great enhancement in the film cooling effectiveness is observed compared to other schemes, Fig. 4.11b. It is worth mentioned that the performance of the MTJ scheme at Br = 0.625 is not the maximum while for the reference studies the presented blowing ratios showed the maximum effectiveness performance and in some cases reversed trend is observed.

Figure 4.12 is the pressure side spanwise-averaged effectiveness comparison between the MTJ and one row of axial fan shaped schemes of Colban et al. (2006) and another one row of axial fan-shaped schemes of Dittmar et al. (2003). Similar to the suction side, the presented blowing ratios in the figure are the lower and upper limits of effectiveness. The trend of performance of the fan-shaped scheme is close to that of the louver scheme. The MTJ scheme showed great enhancement in the effectiveness with low and high blowing ratios compared to the axial shaped scheme.

4.6. Summary

The film cooling effectiveness performance of one row of the Micro-Tangential-Jet (MTJ) scheme is investigated on both pressure and suction sides of a gas turbine vane using the transient TLC technique. The investigations were carried out at three different blowing ratios on the pressure side 0.5, 1.0 and 1.5 and four different blowing ratios on the suction side 0.25, 0.375, 0.5 and 0.625. All blowing ratios were calculated based on the MTJ scheme exit area. The average density ratio during the investigations was 0.93, and the Reynolds Number was 1.4E5, based on the free stream velocity and the main duct hydraulic diameter (1.2E5 based on the vane true chord). The pitch to diameter ratio of the cooling holes is 5 on the pressure side and 6.5 on the suction side. The turbulence intensity during all investigations was 8.5%. The results of the new

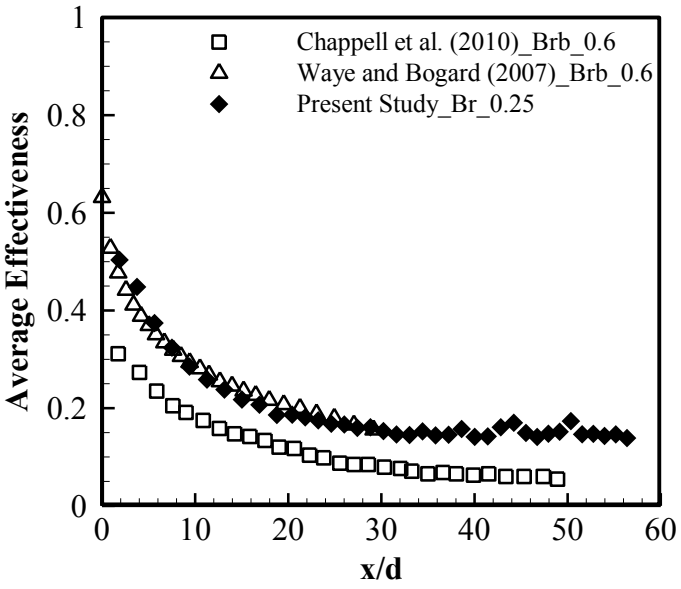

a) Low blowing ratio

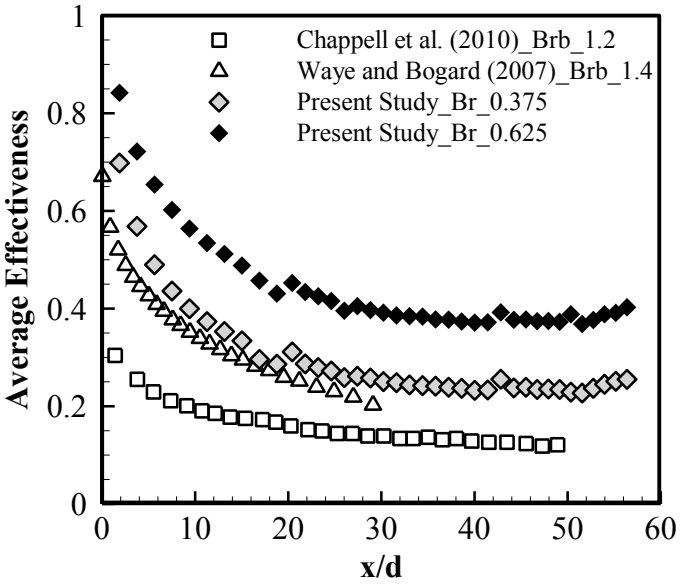

b) High blowing ratio

Figure 4.11, Suction side spanwise-Averaged effectiveness comparison between the MTJ scheme and previously published work

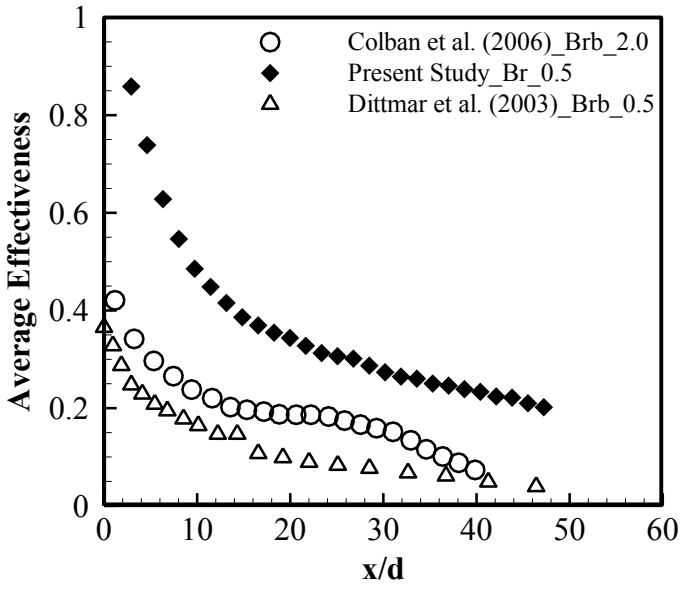

a) Low blowing ratio

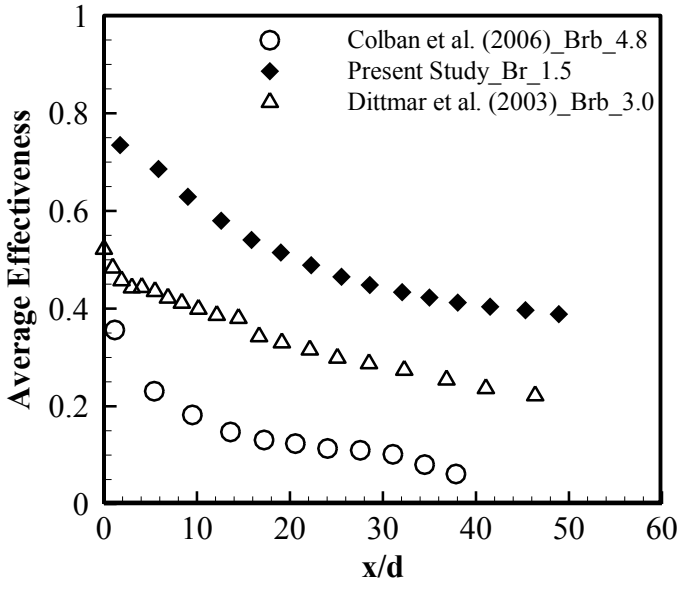

b) High blowing ratio

Figure 12, Pressure side spanwise-Averaged effectiveness comparison between the MTJ scheme and previously published work

scheme were compared with those of the louver scheme with the same coolant amounts were supplied for both. Comparison with previous works is also presented.

The change in the Mach number distribution around the airfoil surface due to the presence of the MTJ scheme was investigated and minor defects were observed. The investigations showed superior film cooling performance for the MTJ scheme compared with traditional shaped schemes. The superiority of the MTJ scheme performance is represented in high effectiveness values and excellent lateral jet spreading that provides optimal surface protection. The performance of tangential injection over actual airfoil surfaces was found close, qualitatively, to that observed over a flat plate. A 2-D coolant film was observed through the results, and is a property of continuous slot schemes only. The presence of this 2-D film layer helps minimize the rate of mixing between the two streams and provides uniform thermal loads on the surface. The small scheme height helped the secondary stream to penetrate long distances inside the mainstream, and hence cover large areas of the airfoil surface. The rate of effectiveness decay on the suction side was observed to be less than that of the pressure side while the lateral jet spreading on the pressure side was observed to be better than that of the suction side. The main disadvantages of the MTJ are the increased pressure drop across the scheme, especially at high blowing ratios and the expected thermal stresses in the region of the scheme exit because of the very thin lip of the scheme.

Chapter 5

Film Cooling Performance of the Micro-Tangential-Jet Scheme; Heat Transfer Coefficient

5.1. Pressure and Suction Sides HTC Without Film Cooling

To clarify the effect of the MTJ scheme on the HTC performance over the airfoil surface, the HTC performance is presented as a ratio of the HTC with to without film cooling (ho). The calibration vane, Fig. 3.2c, was used to determine the HTC distribution on the vane surface without film cooling. A uniform heat flux, $q"$, was applied using the heater. The corresponding steady state wall temperature distribution, T_w, was recorded using the TLC sheet that was placed on top of the heater. Thermocouples were used to record the main stream temperature, T_m. Using Newton law of convection, Eq. (5.1), ho is calculated as follows

$$ho = q"/(T_w - T_m) \tag{5.1}$$

Figure 5.1a, is the spanwise-averaged HTC without film cooling on both pressure and suction sides. The different flow nature on both sides, Fig. 5.1b, results in noticeable difference in the HTC performance of the two sides. On the pressure side the HTC starts decreasing from the beginning of the region of interest until x/d = 15 and then it remains almost constant until the end of the region of interest. The region of interest on the pressure side is very close to the leading edge, it starts at X/Cx = 7.5%. The area of the leading edge is characterized with high turbulence levels and as a result the HTC is at maximum in this region. As x/d increases, the flow becomes less turbulent and a reduction in the HTC is recorded. After x/d = 15, the effect of the leading

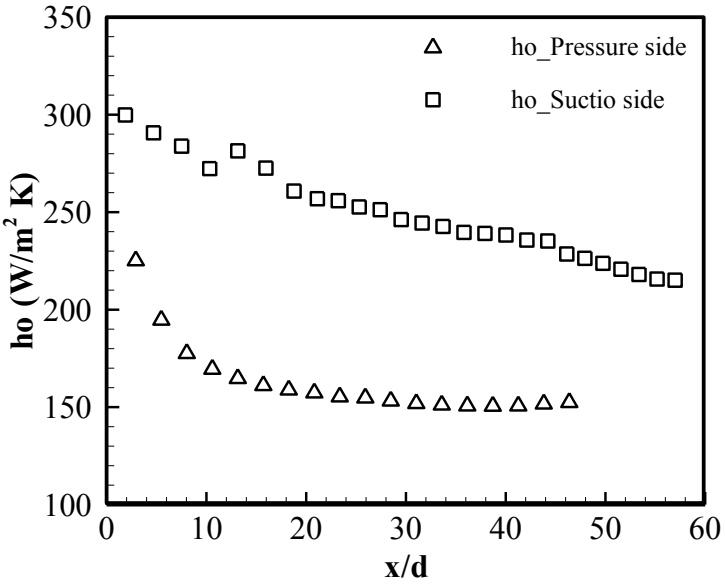

a) HTC (ho) without film cooling

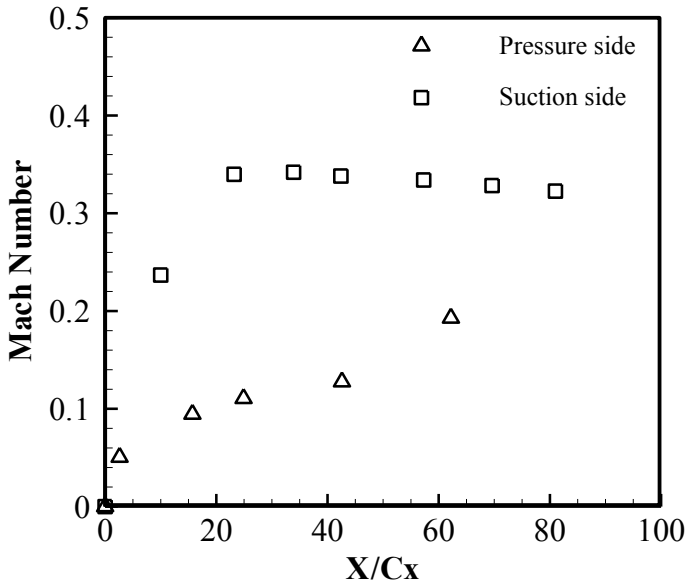

b) Mach number distribution without MTJ scheme

Figure 5.1, Spanwise-averaged HTC (ho) and Mach number distributions without film cooling on pressure and suction sides

edge turbulence vanishes. The normal reduction in the turbulence level as a result of the moving away from the leading edge area is followed with an accelerating flow that tends to increase the turbulence again. The resultant of these two effects is the constant HTC values observed in this region, from x/d = 15 to the end of the region of interest. On the suction side, the case is different because the region of interest is far from the leading edge; it starts at X/Cx = 40%. Starting at x/d = 20, the change in the flow velocity is minor with mild reduction in the direction of the trailing edge, Fig. 5.1b. The flow velocity in this region is high enough for the flow to be turbulent. As a result, the HTC performance is close to that of a flow over a flat plate under uniform flow velocity condition. Consequently, the HTC decreases with increasing x/d.

5.2. Pressure Side HTC Ratio With Film Cooling

Figure 5.2 presents the HTC ratio contours of the MTJ scheme compared with the corresponding contours of the louver scheme. From the figure, uniformity in the HTC ratio distribution for the MTJ scheme at different blowing ratios is noticeable. For blowing ratios 0.5 and 1.0 the increase in the HTC ratio is limited to the region directly after the scheme exit which is a result of the increased turbulence in this region. For the rest of the region of interest, the HTC ratio is almost unity. By increasing the blowing ratio from 1.0 to 1.5, an increase in the HTC ratio is observed all over the region of interest which is a result of the increased coolant amount supplied and the corresponding increase in the turbulence intensity over the surface. The PIV investigations downstream the MTJ scheme over flat plate supports the previous conclusion. Increasing the blowing ratio results in great enhancement in the vortex structure downstream the scheme. When this performance is to be compared with that of the louver scheme, noticeable difference is observable. The strong CRVP generated from the velocity gradients between the main and the secondary streams results in increased HTC ratios. The effects of these vortices are

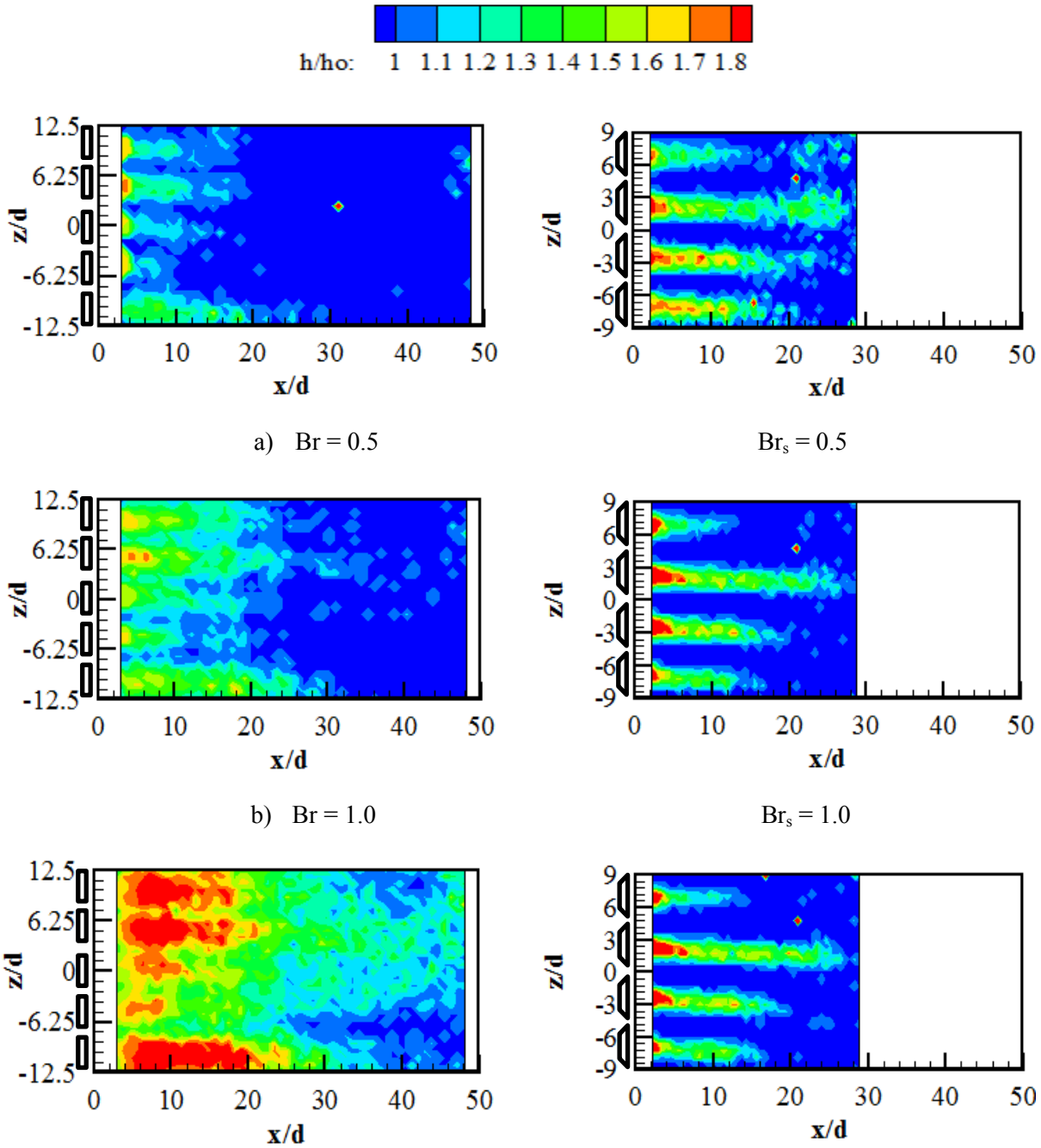

a) Br = 0.5

Br_s = 0.5

b) Br = 1.0

Br_s = 1.0

c) Br = 1.5

MTJ Scheme

Br_s = 1.5

Louver Scheme

Figure 5.2, Pressure side Normalized HTC contours for the MTJ and the Louver schemes

limited to the strong jets areas and no CRVP effects could be noticed in the regions between the holes. As a result, the HTC ratio is almost unity in the regions between the holes. The performance of the HTC ratio downstream the louver scheme is explainable based on the flow field characteristics downstream the circular hole scheme. The PIV investigations in chapter 6 showed that the vortex strength downstream discrete–holes schemes is maximum around the coolant jet. The latter is because of the maximum velocity gradient between the two stream is in this region. The difference between the louver scheme and the circular one will be in the value of the vortex strength; however, the vortex structure is expected to be similar due to the similarity in coolant jet injection method. The resultant is the presence of peaks and lows in the HTC ratio distribution in the lateral direction which leads to non-desirable thermal stresses. Slight increase in the HTC ratio in the region close to the scheme exit is observed by increasing the blowing ratio. The jet lift-off results in a slight reduction in the jets trace lengths in the streamwise direction and thicknesses in the spanwise direction.

The centerline and spanwise-averaged HTC ratios of the MTJ scheme at different blowing ratios are presented in Fig. 5.3. For blowing ratios 0.5 and 1.0 the performance of both is similar from a trend point of view. An increase in the HTC ratio of about 20% for the case of Br = 1.0, in comparison to the case of Br = 0.5, for $x/d < 20$ is also noticeable. For $x/d > 20$ at Br = 0.5 and for $x/d > 25$ at Br = 1.0, the HTC ratio for both cases is unity. This means that the effect of the MTJ scheme on the HTC ratio for blowing ratios lower than unity is limited to the region close to the injection location. This can be explained based on the experimental findings of Harrison et al. (2009) and Dees et al. (2010). They stated that the presence of the film cooling schemes results in boundary layer transition from laminar to turbulent, which results in increased HTC. From the Mach number distribution on the pressure side, Fig. 5.1b, it is noticeable that the flow velocity is low all over the surface. The presence of the MTJ scheme resulted in turbulence enhancement and hence increased HTC ratio at the region following the scheme exit. Beyond $x/d = 20$, the

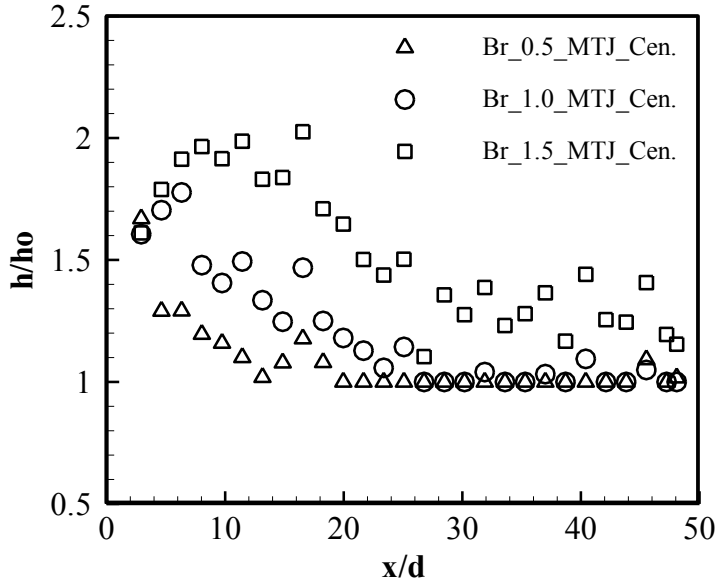

c) Centerline HTC ratio

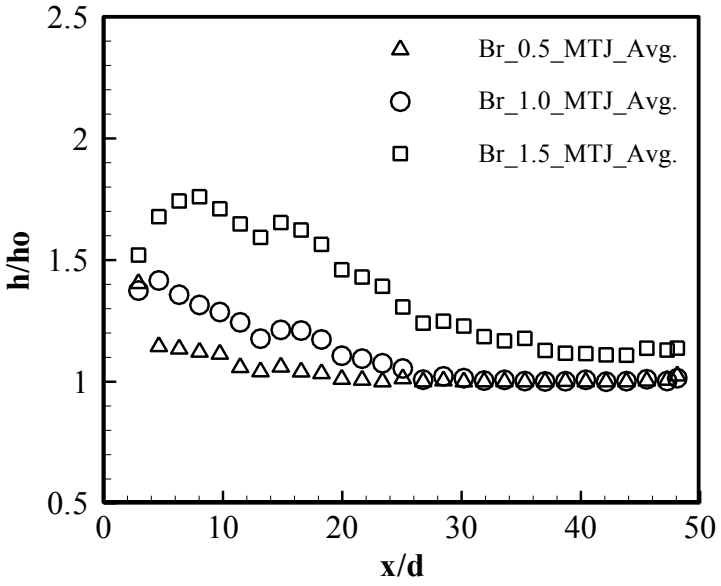

d) Spanwise-averaged HTC ratio

Figure 5.3, Pressure side centerline and spanwise-averaged HTC ratios at different blowing ratios

boundary layer re-laminarizes, which reduces the HTC ratio. The behavior of the boundary layer described above is based on the HTC performance observations and previous studies carried out over similar geometries. However, this could not be confirmed until flow visualization investigations around the vane surface are conducted. In addition to the boundary layer transition, the scheme lip increases the turbulence because it works as a backward ramp in the flow direction. The region aft of the lip is a re-circulation region characterized with vortices of strength dependent on the flow conditions and lip height. Enhanced turbulence downstream the MTJ scheme is observed through the PIV investigations. The turbulence rate decays with downstream distance from the injection location.

From the figure, an increasing decreasing trend of the HTC ratio is observed at Br = 1.5. The HTC ratio increases from the beginning of the region of interest until x/d = 8.0. Then, a similar trend to that observed at Br = 0.5 and at Br = 1.0 is recorded. For Br > 1.0, a vortex opposite in direction, counter clockwise, to the one in the re-circulation region after the lip, which is a clock wise, is created. This is a result of the increased jet velocity in comparison to the main stream velocity. The strength of the counter clock wise vortex decays away from the hole exit as a result of the shear between the two streams. At x/d = 8 the effect of the vortex vanishes completely. A similar effect is recorded in a very small region after the scheme exit, x/d < 4, at Br = 1.0. The increase in secondary stream velocity at Br = 1.0 is a result of the velocity distribution at the scheme exit, which is dependent on the shear on the internal walls of the scheme. The increase in HTC performance at Br = 1.5 is a result of the increased coolant amounts and the increased turbulence. The latter is due to injecting the secondary stream at a velocity much higher than the main stream velocity.

To quantify the comparison between the MTJ and the louver schemes, the centerline and the spanwise averaged HTC ratios are presented in Fig. 5.4 at Br = 1.0. It is observable that the centerline HTC ratio for the two schemes is almost the same for the whole region of interest

except the region directly after the schemes exit, x/d < 5. At x/d < 5, an increase in the HTC ratio for the louver scheme is recorded. For an inclined angle shaped scheme, the interaction between the two cross streams is maximum at the scheme exit, hence the strength of the generated vortices in this region is maximum as well. The spanwise-averaged HTC ratio of the louver scheme is lower than that of the MTJ scheme. This difference is a result of the non-uniform distribution of the HTC ratio of the louver scheme in the spanwise direction, as noticed from the HTC ratio contours, Fig. 5.2.

5.3. Pressure Side Net Heat Flux Reduction (NHFR)

The Net Heat Flux Reduction (NHFR) is used to evaluate the net performance of a scheme. The NHFR, Eq. (5.4), combines the effectiveness and the HTC ratio, by comparing the heat flux passing through the surface with film cooling q''_f, Eq. (5.2), to the corresponding one without film cooling q''_o, Eq. (5.3). The term θ in Eq. (5.4) is a dimensionless temperature and can be calculated from Eq. (5.5). The reciprocal of θ is φ, the overall cooling effectiveness. The value of φ ranges between 0.5 and 0.7 for a typical airfoil cooling system. In the current study, φ is selected as 0.6 which is the choice of most of the previous studies. The values of the NHFR calculated using Eq. (5.4) are expected to be one of three; the first is when the NHFR is less than zero, negative film cooling. In this case film cooling has a detrimental effect and the heat flux passing through the surface with film cooling is higher than that without film cooling. The second is when the NHFR is greater than zero and less than one, positive film cooling. In this case, film cooling is effective and a reduction in the heat flux without film cooling occurs. The third is when the NHFR is greater than one, hyper film cooling. In this case, the overall cooling effectiveness is higher than the assumed value of φ which is 0.6.

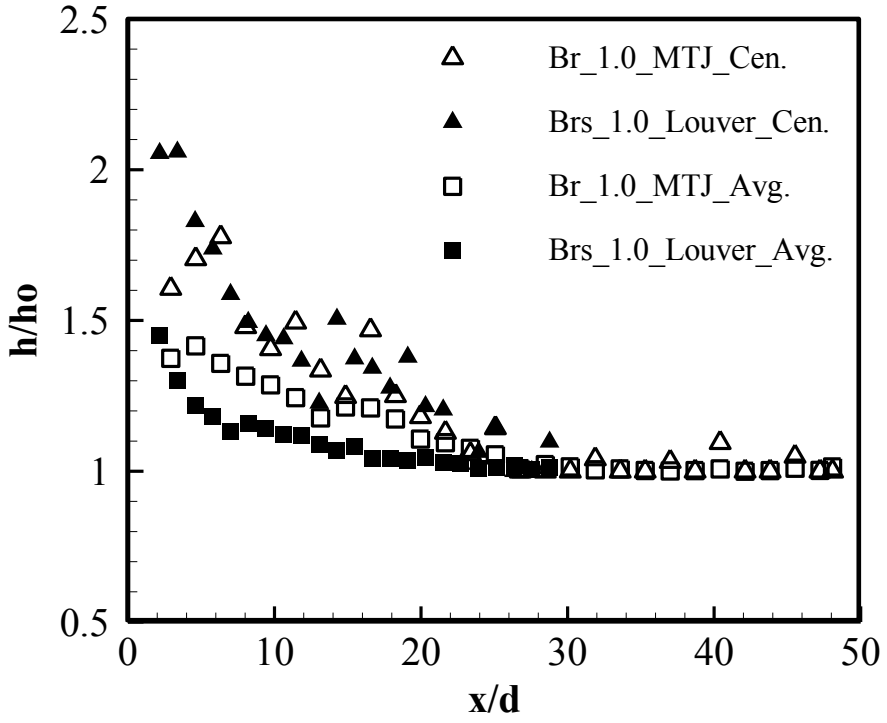

Figure 5.4, Pressure side HTC ratio comparisons between MTJ and louver schemes at Br (MTJ) and Br_s (louver) = 1.0

$$q_f^{"} = h_f\,(T_f - T_w) \tag{5.2}$$

$$q_o^{"} = h_o\,(T_m - T_w) \tag{5.3}$$

then

$$NHFR = 1 - \frac{q_f^{"}}{q_o^{"}} = 1 - \frac{h_f}{h_o}(1 - \eta\theta) \tag{5.4}$$

where

$$\theta = \frac{T_m - T_w}{T_m - T_c} \tag{5.5}$$

The NHFR distribution on both pressure and suction sides is calculated using the detailed effectiveness results presented in the previous chapter, and the HTC results of the current chapter. Fig. 5.5 is the NHFR contours on the pressure side for the MTJ and the louver schemes at different blowing ratios. The MTJ scheme shows superior uniform lateral surface coverage. Enhancement in the NHFR performance is observed when the blowing ratio is increased from 0.5 to 1.0. Similar NHFR contours are observed for Br =1.0 and 1.5. The contours of the louver scheme show the effect of the non-uniform HTC distribution on the net performance of the scheme. The effectiveness distribution downstream the louver scheme is relatively uniform. However, the HTC is not uniform due to the presence of the CRVP around the jet. At some locations over the surface, the NHFR values are below zero which is an indication of negative film cooling performance. Such areas increase in size with blowing ratio increase due to the HTC ratio augmentation that is accompanied with reduction in the effectiveness. The performance of the louver scheme described here is somehow contradicting the performance of normal shaped schemes in literature. The latter is because the coolant amounts currently being supplied to the

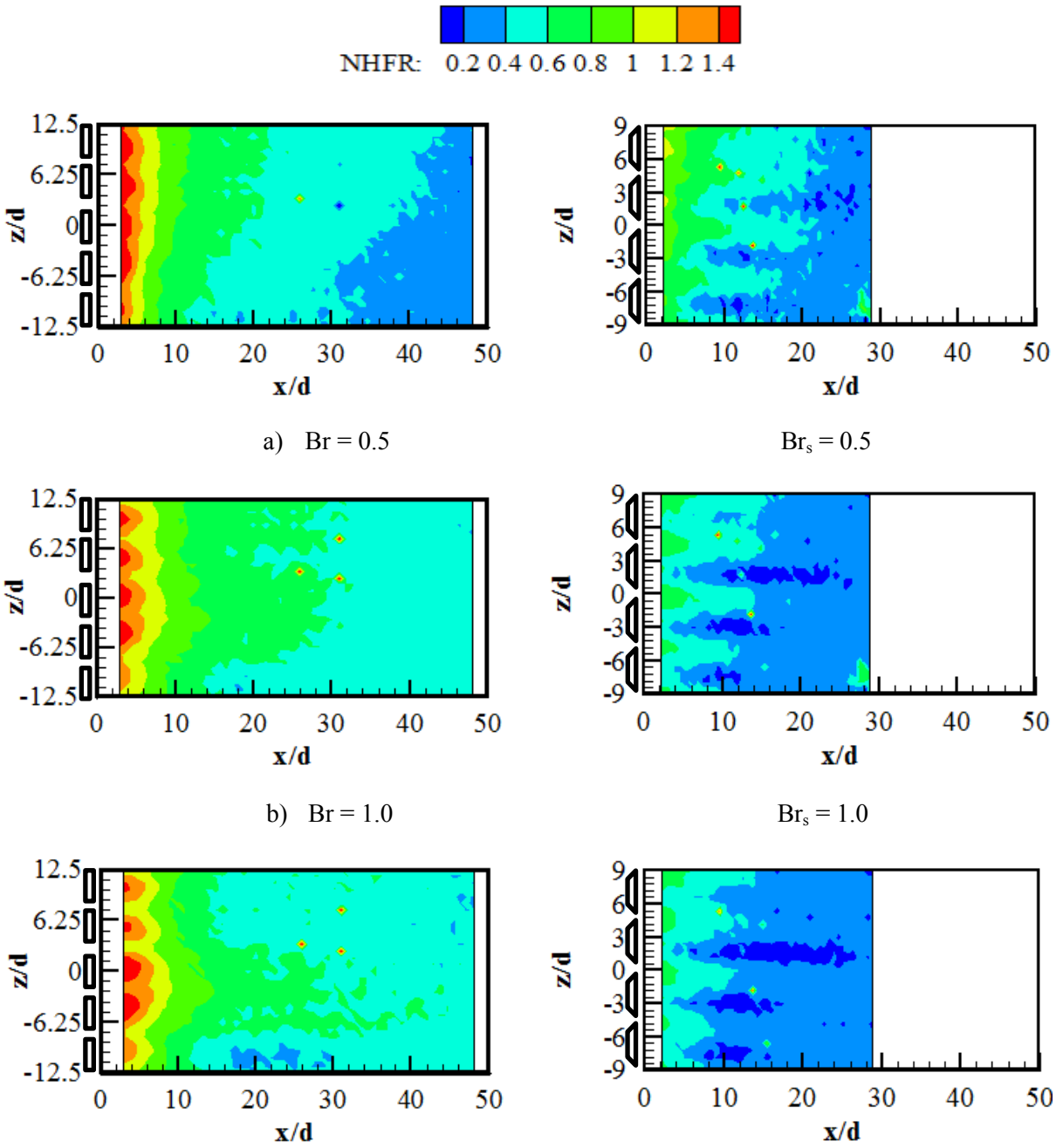

a) Br = 0.5 Br_s = 0.5

b) Br = 1.0 Br_s = 1.0

c) Br = 1.5 Br_s = 1.5

MTJ Scheme Louver Scheme

Figure 5.5, Pressure side NHFR contours for the MTJ and the Louver schemes

louver scheme are larger than the amounts normally supplied if the blowing ratio was calculated based on the scheme base diameter. This was explained in details in chapter 4.

Figure 5.6 presents the centerline and spanwise-averaged NHFR for the MTJ scheme. In the region close to the hole exit, x/d < 8, hyper film cooling is observed. This means that the overall cooling effectiveness is higher than the 0.6 that was assumed during the data reduction. In this region and when x/d < 20 rapid reduction in the NHFR is noticeable as a result of the reduction in the cooling effectiveness, the mixing and advection region. From *x/d* > 20 until the end of the region of interest the NHFR is almost constant with a small rate of reduction, especially at Br = 1.0 and 1.5. Furthermore, at Br =1.0, the NHFR is higher than the NHFR at Br = 1.5. However, the effectiveness of Br =1.5 is higher than the effectiveness of Br = 1.0. This is because the augmentation in HTC ratio as a result of blowing ratio increase from 1.0 to 1.5 is higher than the increase in effectiveness. It can be concluded that a blowing ratio of unity is optimal for the MTJ scheme on the pressure side. It is worth mentioning that a blowing ratio of unity is the optimal blowing ratio for continuous slot schemes as well.

By comparing the NHFR performance of the MTJ scheme with that of the louver scheme, Fig. 5.7, at Br = 1.0, an enhancement higher than 100% in both centerline and spanwise-averaged NHFR is observed all over the region of interest. Both the louver and the MTJ schemes showed uniform NHFR distribution across the span, as observed from Fig. 5.5. This is reflected in the close values of the centerline and the laterally averaged NHFR presented in Fig. 5.7. Enhancing the net film cooling performance while maintaining uniform lateral spreading, is a great advantage of the MTJ scheme. The drop in the NHFR in the region from the injection location and up to x/d < 15 is not preferable from thermal stresses point of view. However, injecting secondary stream from a row of shaped schemes at a location before x/d = 15, is expected to solve this problem.

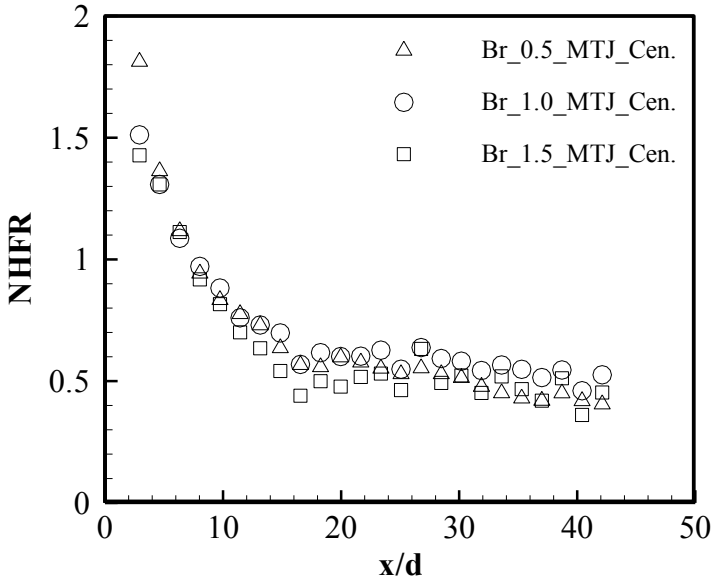

a) Centerline NHFR

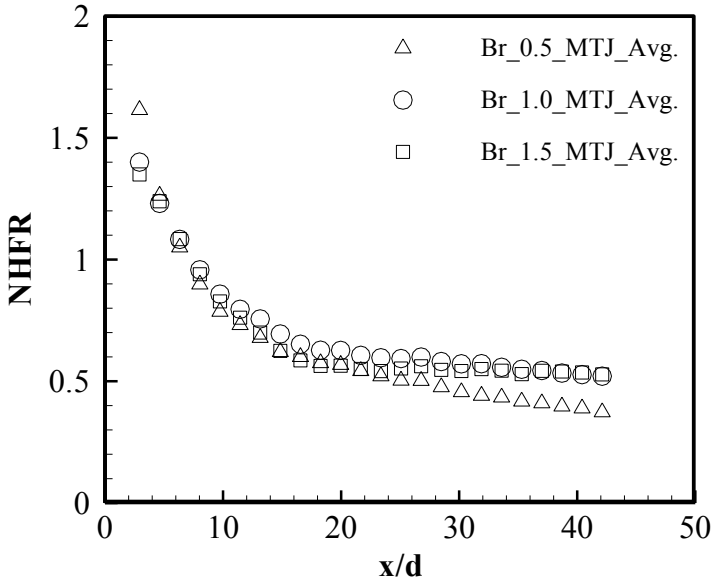

b) Spanwise-averaged NHFR

Figure 5.6, Pressure side centerline and spanwise-averaged NHFR for the MTJ scheme at different blowing ratios

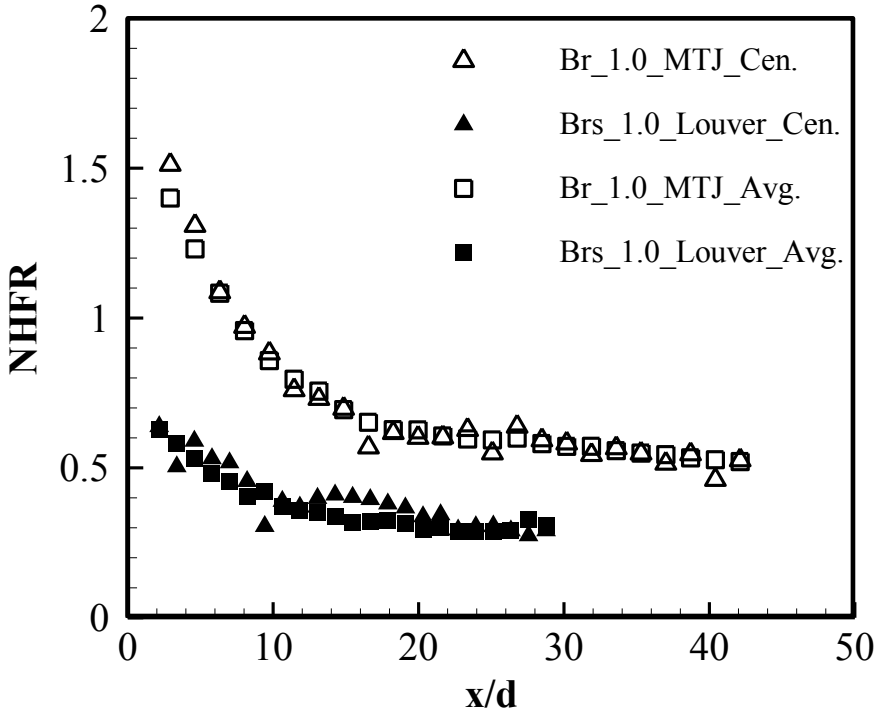

Figure 5.7, Pressure side, NHFR comparisons between MTJ and louver schemes at Br (MTJ) and Br_s (louver) = 1.0

5.4. Suction Side HTC Ratio With Film Cooling

Figure 5.8 presents the HTC ratio contours for the MTJ scheme on the suction side at different blowing ratios and the corresponding contours of the louver scheme. It is observed that the HTC ratio augmentation on the suction side is lower than the rate of HTC ratio augmentation on the pressure side. This agrees with the previously mentioned observation; the flow on the suction side is turbulent in the region of X/Cx > 20%. The HTC performance presented in Fig. 5.8 is in excellent agreement with the findings of Harrison et al. (2009) and Dees et al. (2010). The turbulent flow on the suction side results in high HTC without film cooling, Fig. 5.1a, and hence the presence of the MTJ scheme does not significantly changes the flow characteristics over this surface. With Br = 0.25, the increase in the HTC ratio is limited to a very narrow region directly after the scheme exit. The length of this region increases slightly in the streamwise direction with increasing blowing ratio.

At Br = 0.625 minor changes in the performance trend are observed. This is a result of the presence of some residual material inside a number of holes which results in slight non-uniformity in the coolant distribution across the schemes. In effect, the vanes used in the present study were manufactured using the Stereo Lithography Rapid Prototyping (SLRP) technique. During the manufacturing process, some residual material falls inside the holes. Efforts have been implemented to clean the schemes from such residual materials; however, due to the small dimensions of the scheme, the 100% clean level was not achievable. For low blowing ratios, the pressure drop across the schemes is small and the effect of such residual materials is at minimum; however, increasing the blowing ratio increases their effect. By examining the performance of the louver scheme on the suction side, similar performance to that on the pressure side is observed; increasing the blowing ratio increases the HTC ratio and the area covered with the jet decreases.

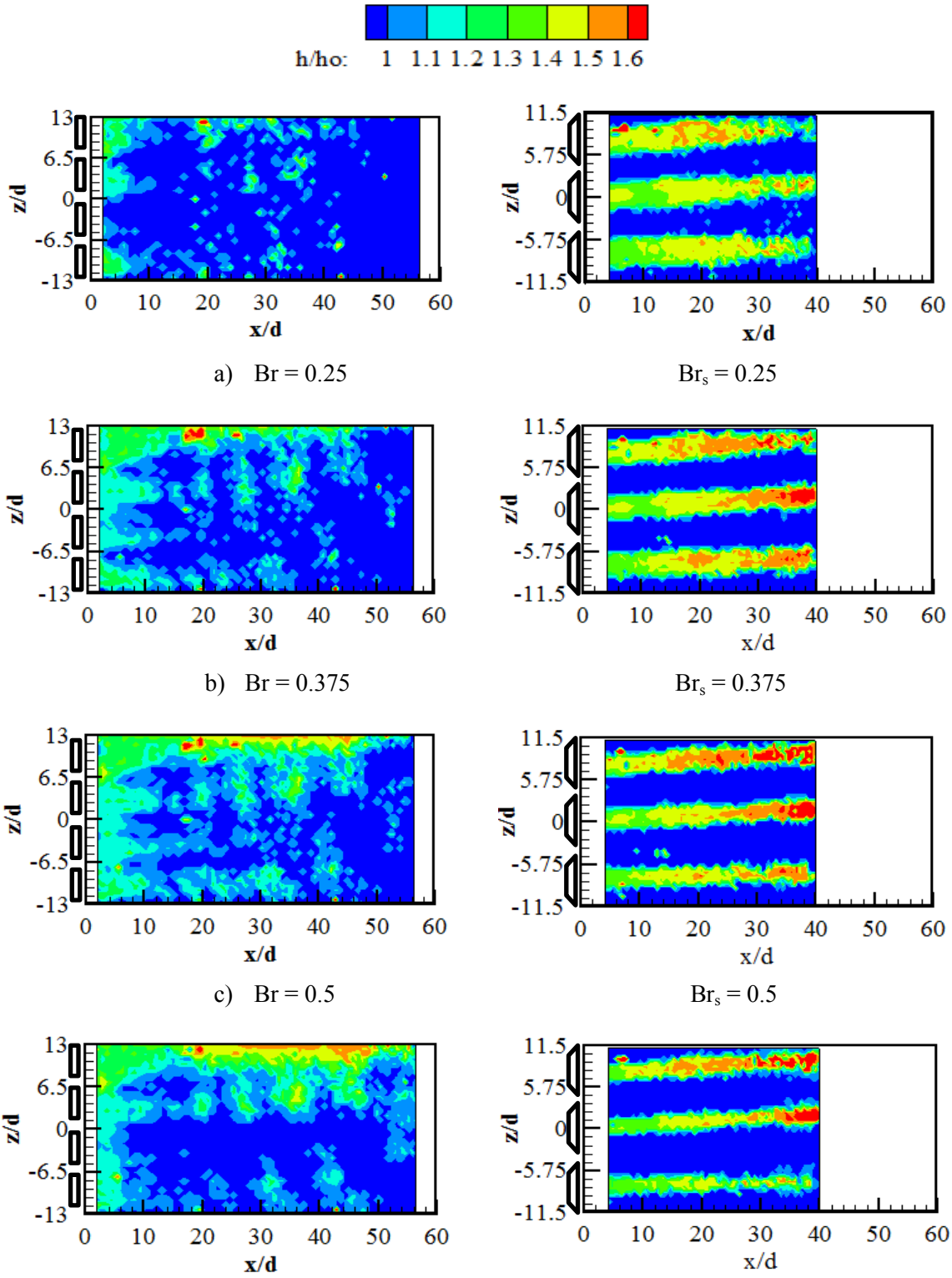

Figure 5.8, Suction side normalized HTC contours for MTJ and Louver schemes

Quantitatively, no significant differences are observable in both centerline and spanwise averaged HTC ratios downstream the MTJ scheme over the suction side with blowing ratio increase, Fig. 5.9. From the figure, the centerline HTC ratio is almost unity all over the region of interest at all blowing ratios except in the region when $x/d < 10$. In this region, the interaction between the two streams, main and secondary, besides the presence of the scheme itself result in enhanced turbulence and accordingly enhanced HTC ratio. The performance trend of all blowing ratios is the same, no increasing-decreasing trends are observable as the case of the pressure side with Br = 1.5. This is because all investigated blowing ratios are less than unity.

When the HTC ratio performance of the MTJ scheme is compared with the corresponding performance of the louver scheme at Br = 0.5, noticeable differences are observed, Fig. 5.10. The centerline HTC downstream the louver scheme is almost constant at all downstream locations. When this HTC is normalized with the HTC without film cooling that has a decreasing trend with downstream distance towards the trailing edge, the result is the increasing centerline HTC ratio trend of the louver scheme. It is also noticeable from the figure that the non-uniform HTC ratio distribution in the spanwise direction results in a gap between the centerline and the spanwise averaged HTC ratios of the louver scheme. The same performance was also observed on the pressure side. Unlike the centerline HTC ratio, the average HTC ratio of the louver scheme is almost constant all over the region of interest. A reduction in the centerline and the spanwise averaged HTC ratio for the MTJ scheme compared with the louver scheme is observed in the figure. This behavior reflects the great benefits of the MTJ scheme as it enhanced the effectiveness values and the lateral spreading and reduced the HTC ratio, compared to inclined angle shaped schemes.

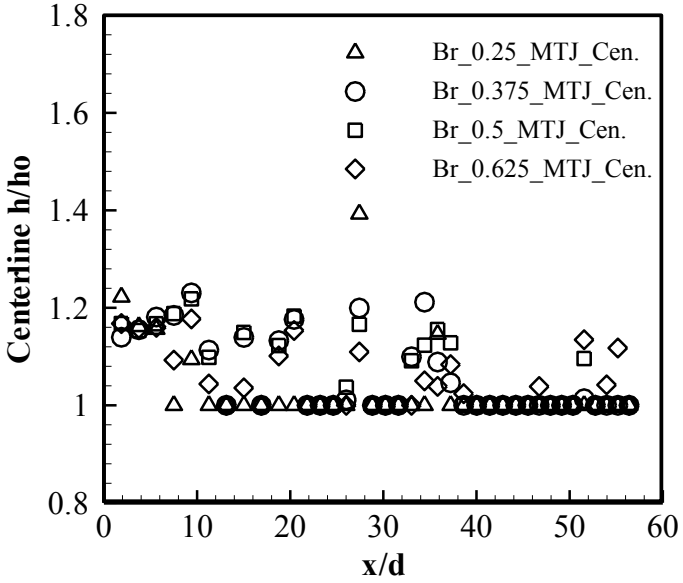

a) Centerline HTC ratio

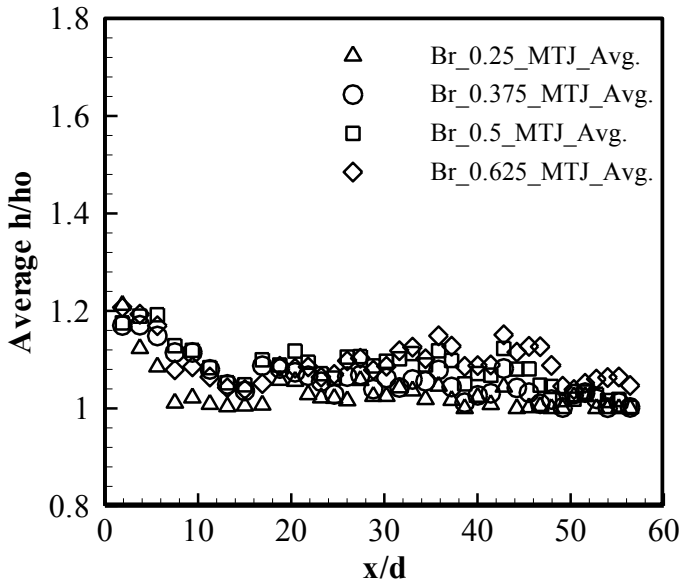

b) Average HTC ratio

Figure 5.9, Suction side centerline and spanwise-averaged h/ho comparison at different blowing ratios

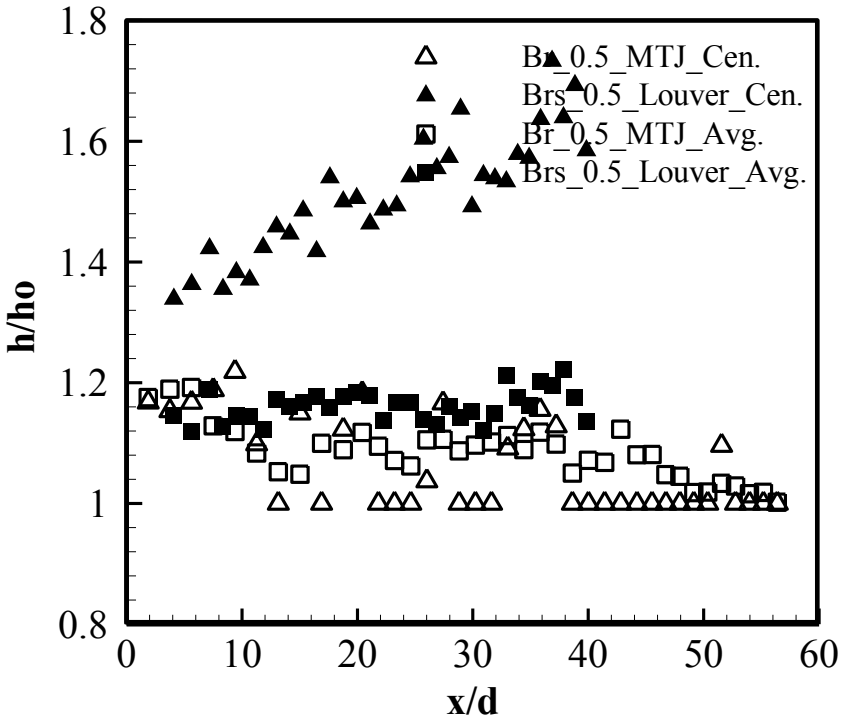

Figure 5.10, Suction side HTC ratio comparisons between MTJ and louver schemes at Br (MTJ) and Br_s (louver) = 0.5

5.5. Suction Side NHFR

The increase in the HTC ratio on the suction side due to the presence of the MTJ scheme is very small and is limited to the region directly after the scheme exit. As a result, the NHFR contours are very similar to the effectiveness contours as observed in Fig. 5.11. Unlike the pressure side, there is no hyper film cooling on the suction side at low blowing ratios. Hyper film cooling is limited to a very narrow region after the scheme exit at Br > 0.5. The performance of the louver scheme on the suction side is not as good as that on the pressure side. The low pressure on the suction side increases the jet lift off capability of the inclined jet and results in low cooling performance shown in Fig. 5.11. The latter is confirmed with the continuous reduction in the NHFR values with increasing blowing ratio.

From the centerline and the spanwise averaged NHFR downstream the MTJ scheme shown in Fig. 5.12, a NHFR of more than 60% is achieved at Br = 0.625 all over the region of interest. From Fig. 5.13, an enhancement of more than 100% is recorded all over the region of interest in the centerline and spanwise-averaged NHFR of the MTJ scheme, in comparison to the enhancement observed with the louver scheme at Br = 0.5. For about two thirds of the region of interest, more than 55% spanwise-averaged NHFR was achieved by the MTJ scheme, whereas the louver scheme did not achieve more than 5% for about 50% of the region of interest. Meanwhile, the centerline NHFR of the louver scheme shows negative performance for $x/d > 25$. This is not the case all over the spanwise direction but this indicates that hot spots appear at some locations on the surface.

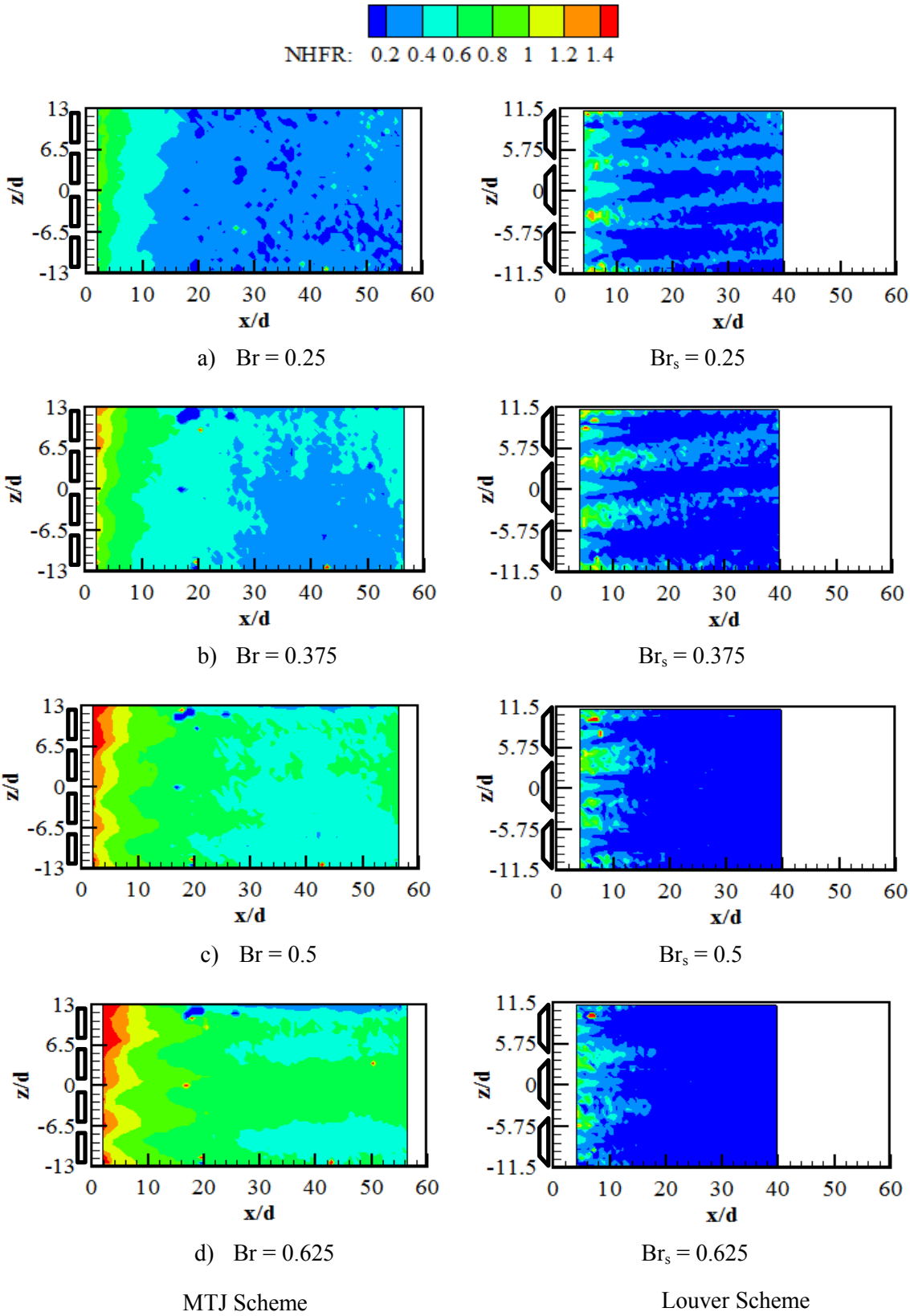

a) Br = 0.25 Br_s = 0.25

b) Br = 0.375 Br_s = 0.375

c) Br = 0.5 Br_s = 0.5

d) Br = 0.625 Br_s = 0.625

MTJ Scheme Louver Scheme

Figure 5.11, Suction side NHFR contours for the MTJ and the Louver schemes

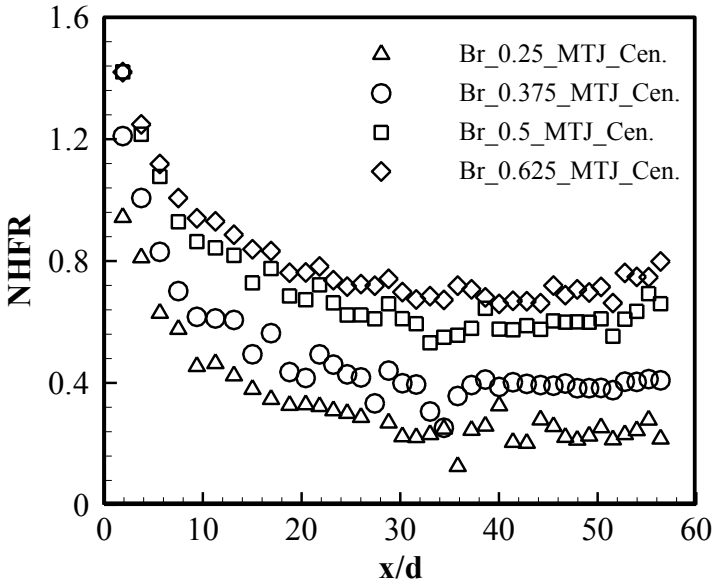

a) Centerline NHFR

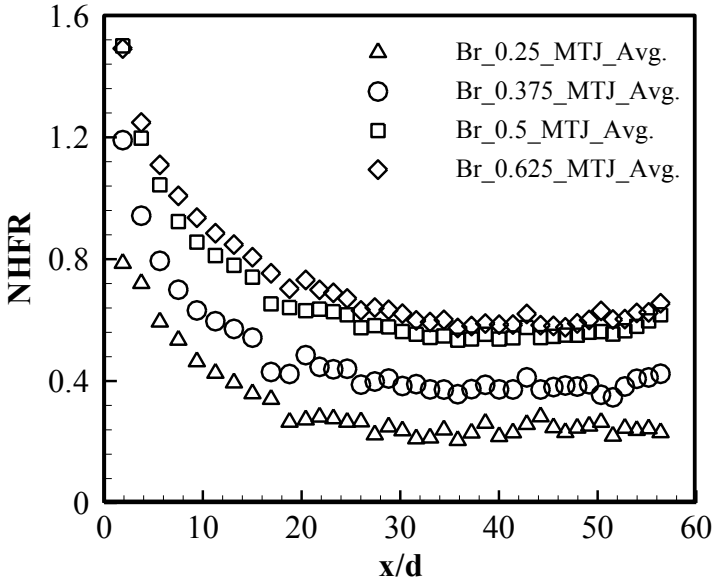

b) Spanwise-averaged NHFR

Figure 5.12, Centerline and spanwise-averaged NHFR for the MTJ scheme at different blowing ratios

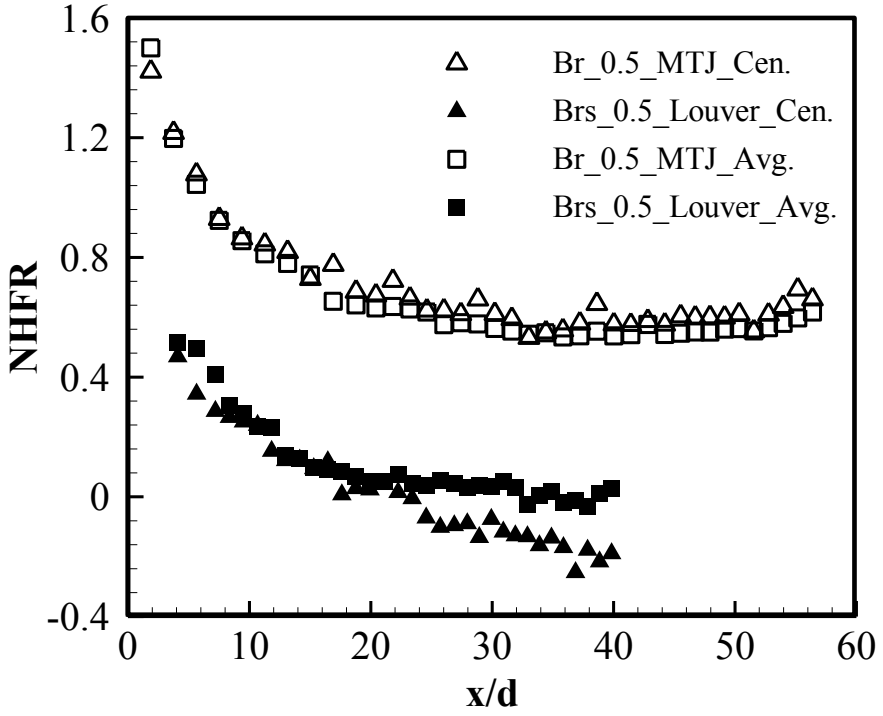

Figure 5.13, Suction side, NHFR comparisons between MTJ and louver schemes at Br (MTJ) and Br_s (louver) = 0.5

5.6. Spatially Averaged NHFR on Pressure and Suction Sides

The spatially averaged NHFR for the MTJ and the louver schemes on the pressure and suction sides is presented in Fig. 5.14. The spatially averaged NHFR is the algebraic mean of the NHFR distribution over the region of interest. The whole region of interest was considered while calculating the spatially averaged NHFR. On the pressure side, Fig. 5.14a, with increasing blowing ratio, an increasing-decreasing trend is observed with the MTJ scheme, while a decreasing trend is observed with the louver scheme. The figure confirms that the optimal performance for the MTJ scheme on the pressure side occurs at Br = 1.0. On the pressure side, the MTJ scheme achieved a maximum overall NHFR of about 70% with superior uniformity in the lateral jet spreading. On the suction side, Fig. 5.14b, the MTJ scheme showed an increasing NHFR trend with increasing blowing ratio. A maximum spatially averaged NHFR of about 70% is achieved at Br = 0.625 and the performance curve is still moving up .The slope of the performance curve decreased when the blowing ratio is increased from 0.5 to 0.625. This is an indicator that the optimal film cooling performance on the suction side will be at a blowing ratio close to unity, similarly to the pressure side. The same decreasing trend is observed for the louver scheme but with a higher negative slope than the pressure side. The increased slope is a result of the reduced pressure on the suction side and hence the increased tendency of the jet to lift off the surface. The decreased pressure on the suction side helps the tangential jet to penetrate longer distances and to cover a larger area than the normal inclined angle shaped schemes.

5.7. Comparison With Previous Work

The HTC ratio performance of the MTJ scheme is compared with the corresponding performance of the trench scheme of Harrison et al. (2009) on the suction side and the axial fan-shaped scheme of Dittmar et al. (2005) on the pressure side. In the present study, the MTJ scheme

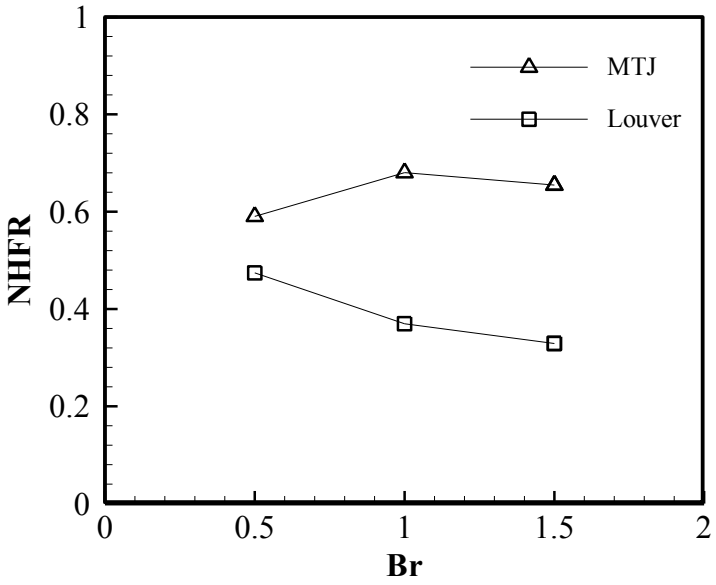

a) Pressure side

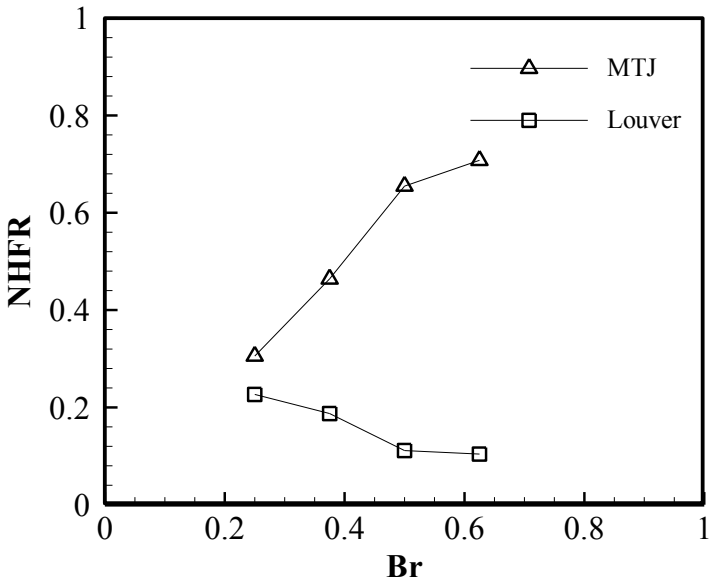

b) Suction side

Figure 5.14, Pressure and suction sides specially-averaged NHFR versus blowing ratio for the MTJ and the louver schemes with the same coolant amount supplied to both schemes

exit area was selected for blowing ratio calculations while in the work of Harrison et al. (2009) and Dittmar et al. (2005) the blowing ratios were calculated based on the scheme base diameter. As a result, the blowing ratios chosen from the reference works were selected based on the same coolant amount principle, as in the case of the louver scheme. So that in all figures, the coolant amounts supplied to the MTJ scheme, and the trench, or the fan-shaped are relatively close to each other. Fig. 5.15 is the suction side HTC ratio comparison between the trench and the MTJ schemes at low and high blowing ratios. The HTC performance of the trench scheme with tripped and un-tripped boundary layer conditions is presented. For both low and high blowing ratios, the MTJ scheme showed lower HTC ratio than the trench scheme with un-tripped boundary layer. This is attributed to the turbulent flow on the suction side of the present study especially in the region of interest and hence the presence of the scheme does not result in significant increase in the turbulence intensity over the surface. Meanwhile, with the work of Harrison et al. (2009), the flow was not fully turbulent and the presence of the scheme resulted in boundary layer transition to turbulence, hence high HTC augmentation is observed compared to the MTJ scheme. This is confirmed from the HTC performance of the trench scheme with tripped boundary layer; the HTC ratio in this case is very close to that of the MTJ scheme. In effect, the boundary layer before the scheme is fully turbulent due to the presence of the trip; hence, the presence of the scheme did not affect the turbulence level much. The results of the two schemes are very close because for both schemes, the coolant stream is supplied in a way that keeps the resulting vortices, especially the CRVP, at a minimum. If the HTC results for the louver scheme on the suction side are recalled, the effect of the CRVP is more significant and is represented in the increased spanwise-averaged HTC in comparison to that of the MTJ scheme.

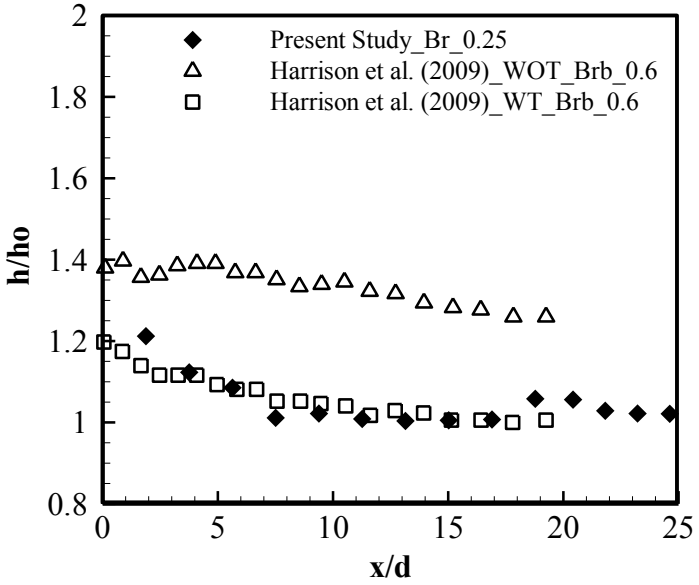

a) Low blowing ratio

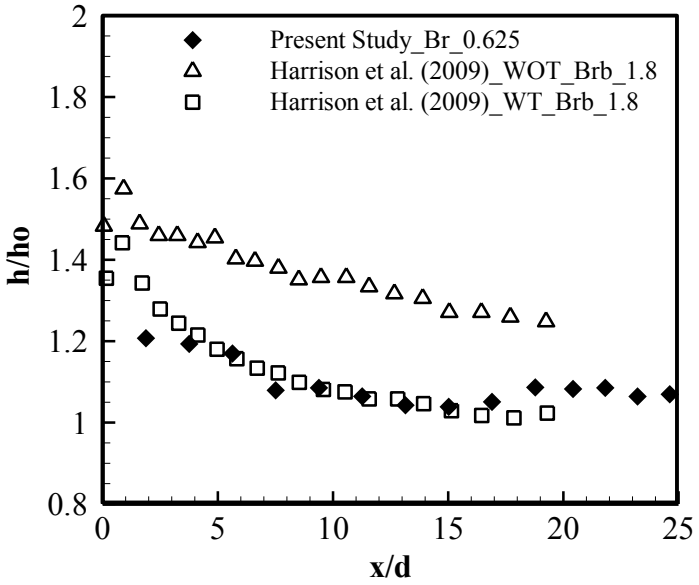

b) High blowing ratio

Figure 5.15, Suction side spanwise-Averaged HTC ratio comparison between the MTJ scheme and previous work

Figure 5.16 is the pressure side HTC performance comparison between the MTJ scheme and one row of axial fan-shaped schemes proposed by Dittmar et al. (2005). The same blowing ratio criterion used with the suction side is applied here with the pressure side. At low blowing ratios, the performances of both schemes are very similar. A slight increase in HTC ratio is observed downstream the fan-shaped scheme. At high blowing ratios, the HTC ratio downstream the MTJ scheme is very high compared to that downstream the fan-shaped scheme. As mentioned earlier, the location of the MTJ scheme on the pressure side is in a low velocity region. The presence of the MTJ scheme in this region results in significant changes in the flow characteristics especially at high blowing ratios. The latter results in higher HTC augmentations compared to other normal shaped schemes. For both low and high blowing ratios, the HTC downstream the fan-shaped schemes is almost constant all over the region of interest; a slight increase is recorded at $Br_s = 3.0$ than $Br_s = 0.5$ for $x/d > 20$. The augmentation in the HTC ratio far downstream is explainable and it is due to the increased blowing ratio and hence the enhanced turbulence. However, the performance close to the scheme exit is unexpected and could be related to the difficulty of capturing good quality temperature images close to the scheme exit because of the coolant lift off at this region.

5.8. Summary

The HTC performance of one row of a new film cooling scheme, the Micro-Tangential-Jet (MTJ) scheme, is investigated on both pressure and suction sides of a gas turbine vane using the transient TLC technique. The investigations were carried out at three different blowing ratios on the pressure side 0.5, 1.0 and 1.5 and four different blowing ratios on the suction side 0.25, 0.375, 0.5 and 0.625. The average density ratio during the investigations was 0.93, and the Reynolds Number was 1.4E5, based on the free stream velocity and the main duct hydraulic diameter

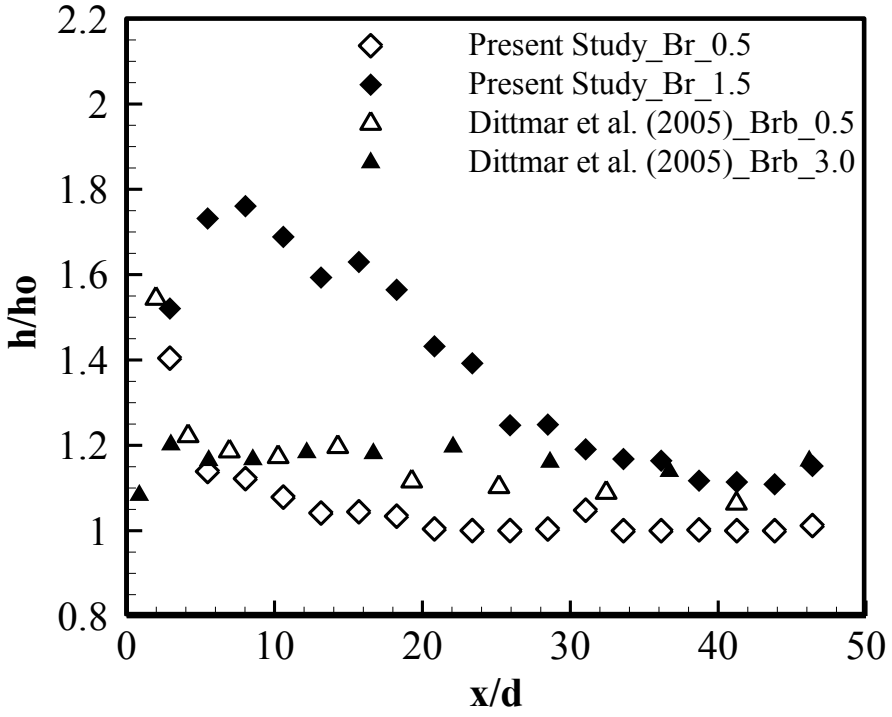

Figure 5.16, Pressure side spanwise-Averaged HTC comparison between the MTJ scheme and previous work

(1.2E5 based on the vane true chord). The pitch to diameter ratio of the cooling holes is 5 on the pressure side and 6.5 on the suction side. The turbulence intensity during all investigations was 8.5%. The results of the new scheme were compared to those of the louver scheme, which is an inclined angle shaped scheme. The same coolant amounts were supplied for both schemes.

The HTC performance of the MTJ scheme was presented as a ratio of the HTC with film cooling to that without film cooling. The MTJ scheme showed good HTC performance on both pressure and suction sides and no significant increase in the HTC ratio was recorded as a result of the presence of the MTJ scheme on the surface. The values recorded for the HTC ratio were comparable to the corresponding values recorded for the louver scheme on the pressure side, whereas on the suction side, the HTC ratio was reduced. The uniformly distributed HTC in the spanwise direction is one of the advantages of the MTJ scheme over the louver scheme since it helps reducing the thermal stresses on the surface. To judge the overall performance of the MTJ scheme, both the effectiveness, presented in a separate paper, and the HTC ratio were combined in the NHFR parameter. Based on the NHFR results, the MTJ scheme showed excellent enhancement in the film cooling performance on both pressure and suction sides. The investigations showed that a blowing ratio close to unity, based on the scheme exit area, provides an optimal film cooling performance with the MTJ scheme on both pressure and suction sides.

Chapter 6

Flow Field Characteristics Downstream the Micro-Tangential-Jet Scheme

Comprehensive flow field investigations downstream the MTJ scheme are essential to provide explanations of the observed promising effectiveness and HTC performances. To be able to conduct the flow field investigations downstream the MTJ scheme; a scaled up model is used. The scaling factor between the scaled-up MTJ and the MTJ schemes is 5:1 respectively. The geometrical ratios of the scaled up MTJ scheme applied through this study, are presented on the detailed views of the scheme in Fig. 6.1.

The flow field characteristics downstream one row of holes of the MTJ scheme and another row of circular hole schemes are investigated over a flat plate at the same test conditions. Three blowing ratios are considered through this study, 0.5, 1.0 and 1.5 at a density ratio of unity. The blowing ratios are calculated based on the MTJ and the circular hole schemes exit areas. The mainstream Reynolds Number was 1.16E5, based on the free stream velocity and the main duct hydraulic diameter. The turbulence intensity during all investigations was 8%, determined using the PIV technique.

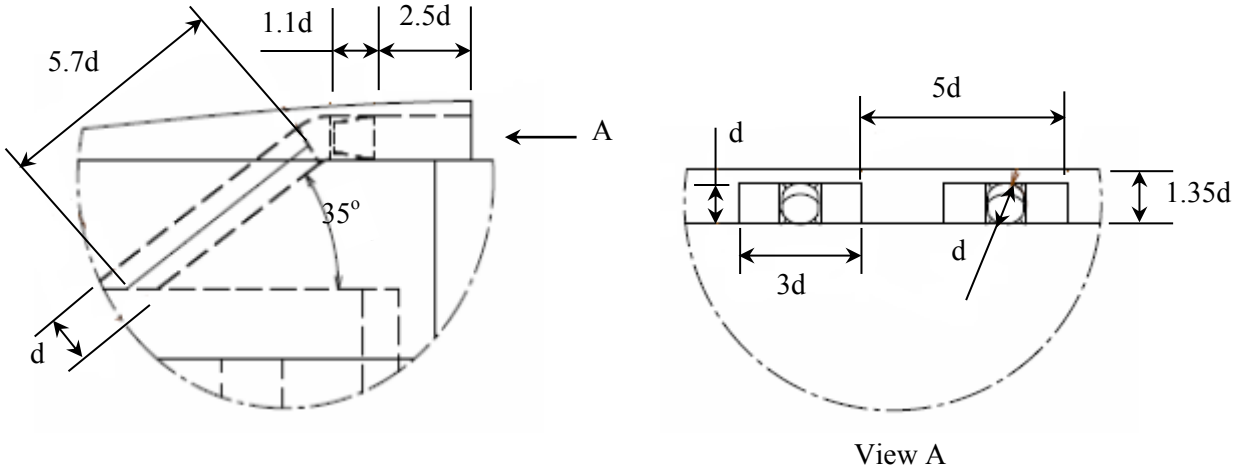

Figure 6.1, The Scaled-up MTJ scheme geometrical details

6.1. Velocity Distributions Downstream the MTJ Scheme with Injection

For the flow field characteristics downstream the MTJ scheme to be clarified, the performance of one row of circular hole schemes was investigated at the same test conditions. The main geometrical difference between the two schemes was the pitch to diameter ratio. The pitch to diameter ratio between MTJ schemes was 5 and it was 3 between circular hole schemes. This parameter affects the distance needed for adjacent jets to join and perform a continuous film, which is not being considered in the comparison between the two schemes. It is important also to mention that the schemes exit areas were chosen for blowing ratio calculations instead of the base diameter. The relatively small base diameter of the MTJ scheme resulted in non-clear performance when used for blowing ratio calculation. To overcome this challenge, the exit area of the scheme was chosen for blowing ratio calculation and the same criterion was applied to the circular hole scheme as well.

Figure 6.2 is the 3D velocity ratio contours comparison between the MTJ and the circular hole schemes close to the scheme exit, x/d = 2.0, at different blowing ratios. In the figure, the main x-axis velocity is represented with the color contours while the in-plane velocities are represented with the vectors. Three different velocity regions are observable from Fig. 6.2a for the MTJ scheme at Br = 0.5. Region (a), is the region in front of schemes injection slots which ends at y/d = 1.0. This region is characterized with high velocity gradients in the lateral direction, z-direction. It is also noticeable that the in-plane velocity components, *v* and *w*, are relatively high in this region and are directed towards the low velocity regions between adjacent holes. This is an indication that not far from the schemes exits the jets are expected to merge together and perform a continuous film. Region (b) is characterized with more uniform velocity distribution than region a, however; it is characterized with velocity gradients in the y-direction. The reason of this is the presence of the scheme lip which works as a backward ramp in the flow direction which results in flow recirculation and high turbulence. Region (c) could be considered as the mainstream region

where the change in the flow characteristics is at minimum. Noticeable differences are observable from Fig. 6.2a between the flow field downstream the MTJ scheme and the corresponding flow field downstream the circular hole scheme at Br = 0.5. The flow downstream the circular hole scheme is more uniform in the lateral direction as a result of the absence of the added material to manufacture the MTJ scheme. Moreover, the velocity distribution downstream the circular hole scheme in the y-direction is apparently divided into two regions; a low velocity region and a high velocity region. The low velocity region is the region close to the surface, $y/d < 0.8$, and it is occupied with the secondary jet. The high velocity region occupies the rest of the region of interest and represents the mainstream area and part of the boundary layer with enhanced velocity due to the injection of the secondary stream.

If the flow field downstream the MTJ is examined at higher blowing ratios, Br = 1.0 and 1.5, at the same downstream location, similar flow field characteristics as the case of Br = 0.5 are observable in Figs. 6.2b and c. However, three main observations are noticeable as follows; first, the areas of low velocity between adjacent schemes is vanishing by blowing ratio increase. This is a result of the increased lateral velocity component, which shortens the distance needed for separate jets to join and perform a continuous film. Second, the in-plane velocity gradients from the mainstream towards the secondary stream increases and the y-axis velocity component become more dominant with blowing ratio increase. The latter is a result of the increased secondary stream velocity and hence the shear in the interface region between the two streams. This in turn results in more mainstream entrainment inside the secondary stream area. Third, for all blowing ratios, all jets are totally attached to the surface with the film characteristics are being enhanced with blowing ratio increase. The change in the flow field characteristics downstream the circular hole scheme with blowing ratio increase is significant, as observed from Figs. 6.2b and c. At high blowing ratios, the secondary jet lifts-off the surface because of the increased jet

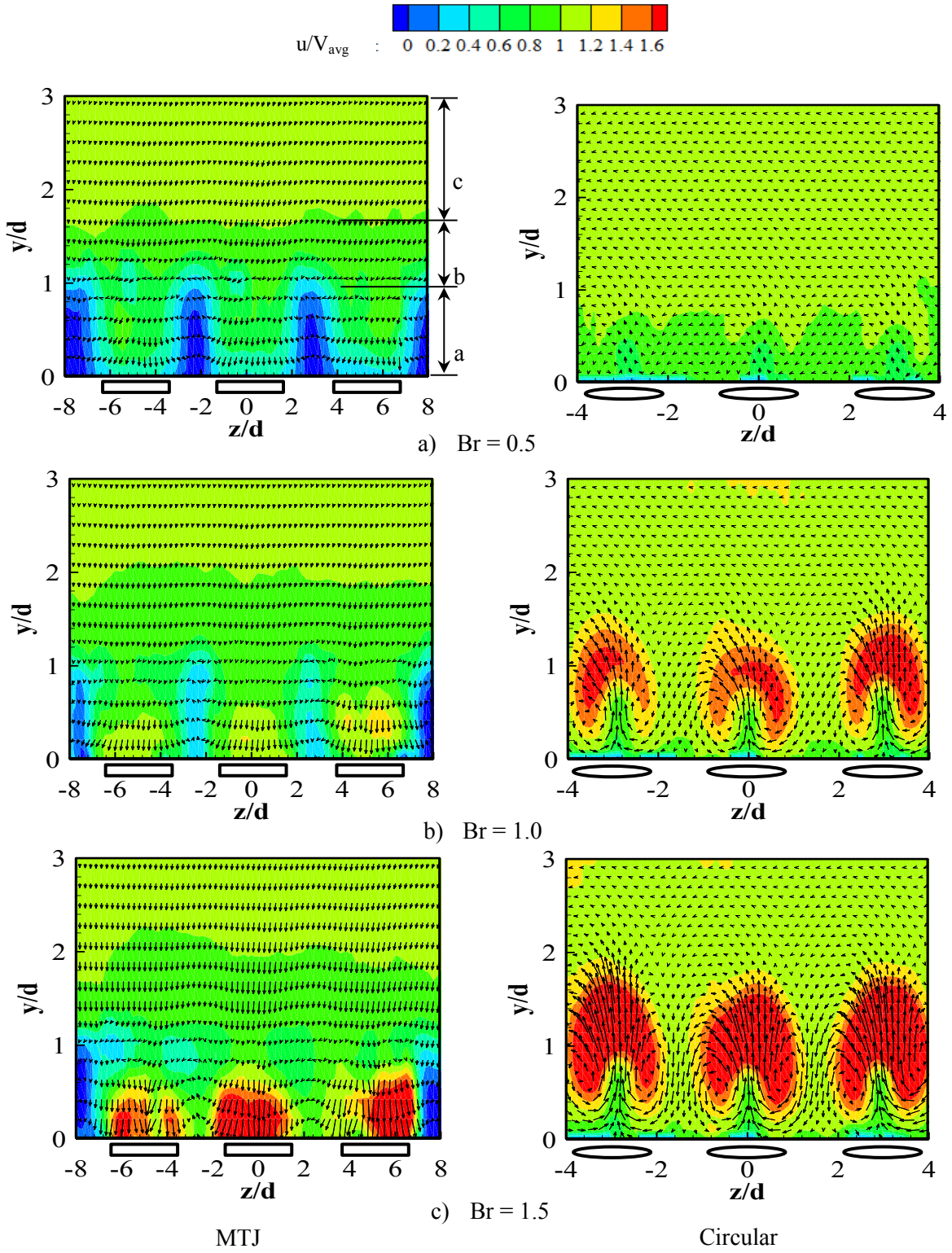

Figure 6.2, Velocity ratio distribution at x/d = 2.0 for the MTJ and the circular hole schemes at different blowing ratios

momentum. Once the secondary stream lifts off the surface, the mainstream surrounds it from all directions. One of the greatest effects of this is the increased in-plane velocity components that enhance the lift of the jet and allow more mainstream to be entrained beneath the jet.

To show the development in the flow field at further downstream distance, the velocity contours at x/d = 8, are presented in Fig. 6.3. From the figure, significant developments in the velocity distribution downstream the MTJ scheme are noticeable at Br = 0.5. The latter is represented in the reduced velocity gradients in the lateral direction. On the other hand, the flow field downstream the circular hole scheme did not changed too much with downstream distance from the injection location. The main observation regarding the flow field downstream the circular hole scheme is the change in the boundary layer height in lateral. This is an indication of poor lateral secondary jets spreading as the jet is concentrated in front of injection locations only. The formation of a clear continuous film with secondary stream injection using the MTJ scheme is clear from Figs. 6.3b and c. In Fig. 6.3b, Br = 1.0, a thin secondary jet layer is covering the majority part of the region of interest. In the intermediate locations between jets, upward directed in-plane velocity components are observable and they are more clear with Br = 1.5, Fig. 6.3c. The lateral expansion angles of the scheme direct part of the secondary jet toward the intermediate regions between adjacent schemes. As the blowing ratio increase, the amount of coolant directed towards those regions increase. The larger the lateral expansion angles, the faster the joining of adjacent jets and hence the formation of a continuous secondary film. However, increasing the angles beyond certain value will result in significant coolant amount loss, as is clear from Fig. 6.3c. Reducing the lateral expansion angles solves the problem of coolant loss; however, it will delay the formation of the continuous film. An optimal angle size must be carefully selected. When the performance of the circular hole scheme at downstream location is examined at high blowing ratios, Figs. 6.3b and c, a thick continuous film is observable. The film is not attached to the surface everywhere especially at Br = 1.5 due to the lift off that occurred close to the injection

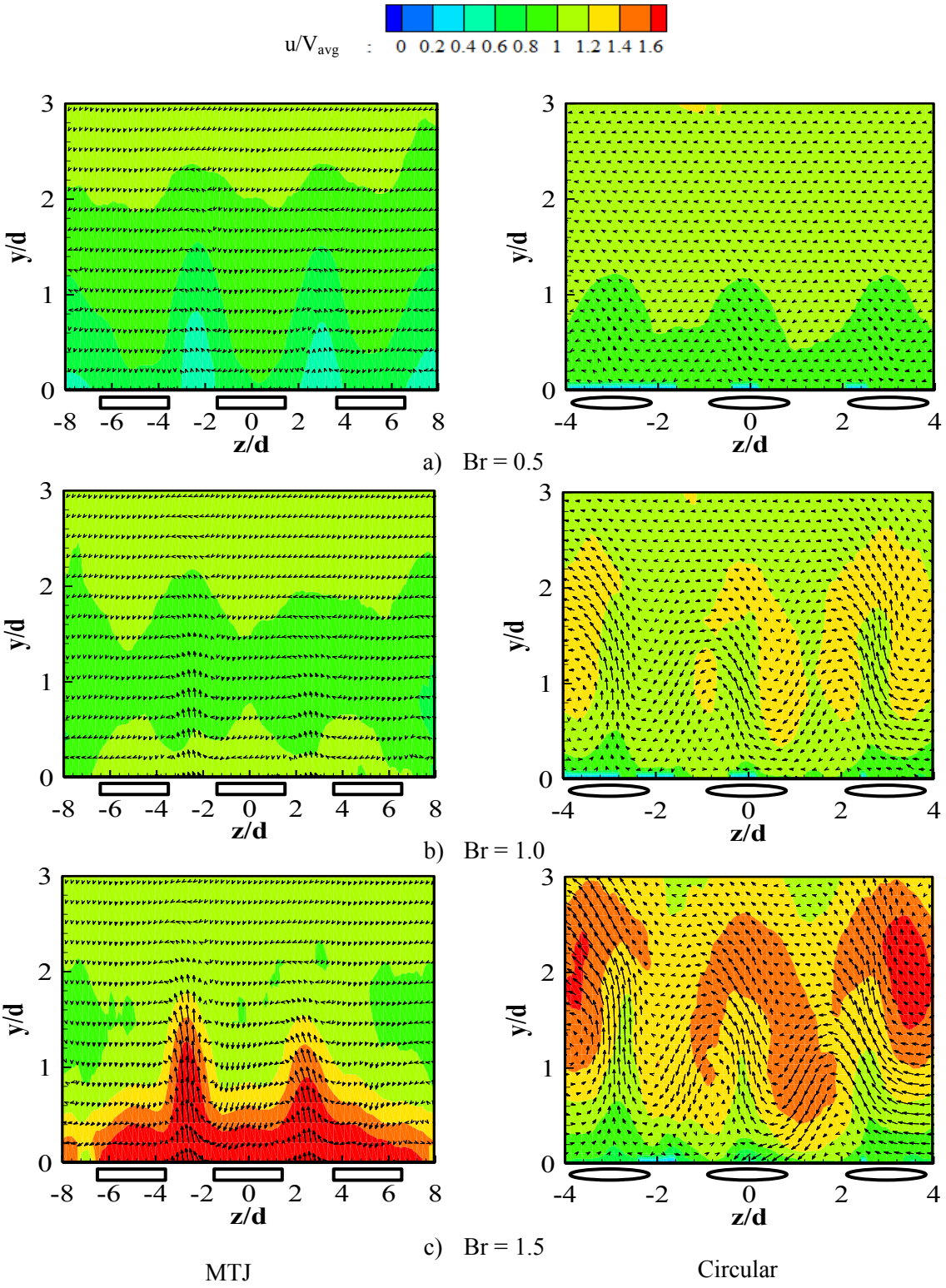

Figure 6.3, Velocity ratio distribution at x/d = 8.0 for the MTJ and the circular hole schemes at different blowing ratios

location. At further downstream location, the jet is expected to be totally reattached to the surface; however, no great film cooling performance is expected due to the entrainment of significant mainstream mass inside the film. Enlarged crescent shapes are still observable at the middle of the film which is an indication of the reduced velocity gradients between the two streams.

Figure 6.4 is the 2D velocity distributions with vertical distance, y-axis, at different downstream locations and blowing ratios. At low blowing ratio, Br = 0.5, the shear between the two streams tends to increase the secondary stream velocity. This is clear from the velocity development with downstream location, Fig. 6.4a, where far downstream, x/d = 16, the velocity distribution is almost a normal boundary layer one. With higher blowing ratios, Br = 1.0 and 1.5, the scenario is different, Figs. 6.4b and c. As observed from the figures, the secondary stream velocity is higher than the mainstream velocity for y/d < 1.0 at all downstream locations. This is an indication that the secondary stream is still strong enough to last for further downstream distances, while it is still fully attached to the surface. When a comparison is carried out between Figs. 6.4a, b and c, regarding the film thickness, it is obvious that the film thickness increases with blowing ratio increase. The latter, is a result of the increased coolant amount injected and the increased shear in the interface region between the two streams due to secondary stream velocity increase. It is also observable from Fig. 8b that the velocity of the secondary stream for Br = 1.0 is higher than the main stream velocity, at the time both are supposed to have the same value. As mentioned earlier, this is due to the effect of the scheme walls that result in non-uniform velocity distribution at the scheme exit with maximum velocity at the centerline. Also, an out of trend performance is observable in the case of x/d = 2.0 which is a result of a light reflection problem on the scheme material that affected the 2D measurements in the near injection location.

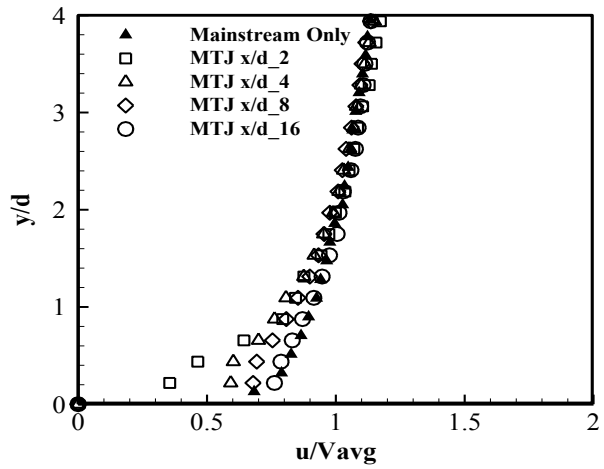

a) Br = 0.5

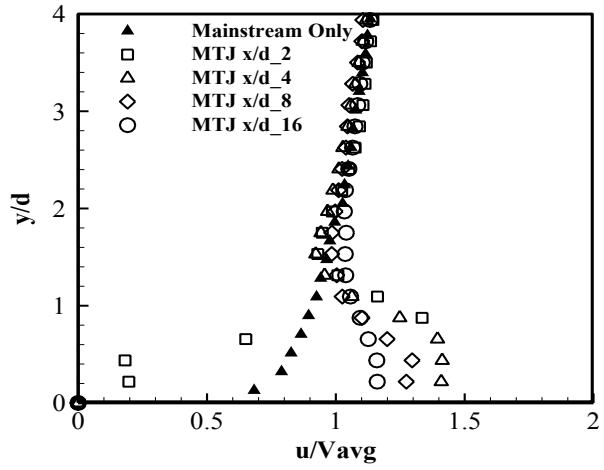

b) Br = 1.0

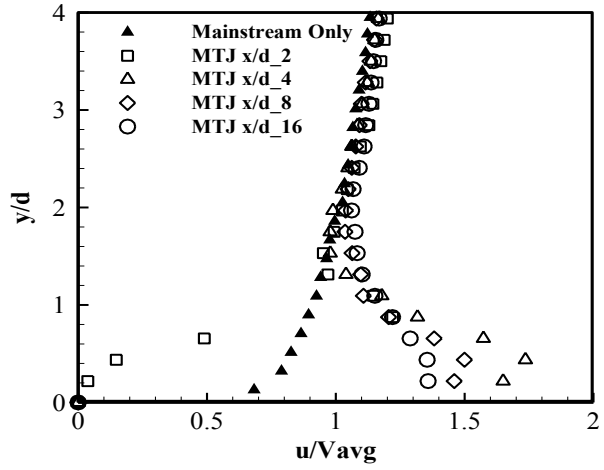

c) Br = 1.5

Figure 6.4, Mid-plane (z/d = 0.0) x-axis velocity ratio comparison for the MTJ scheme at Different downstream locations and blowing ratios

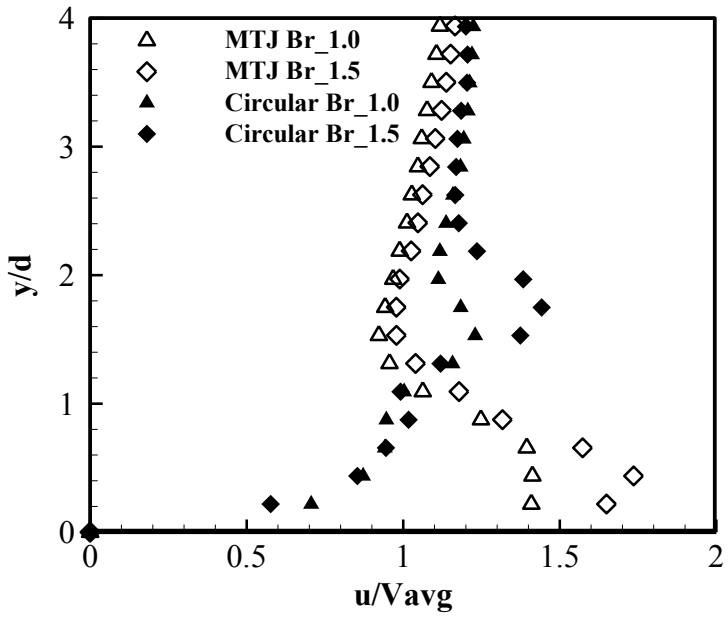

a) x/d = 4.0

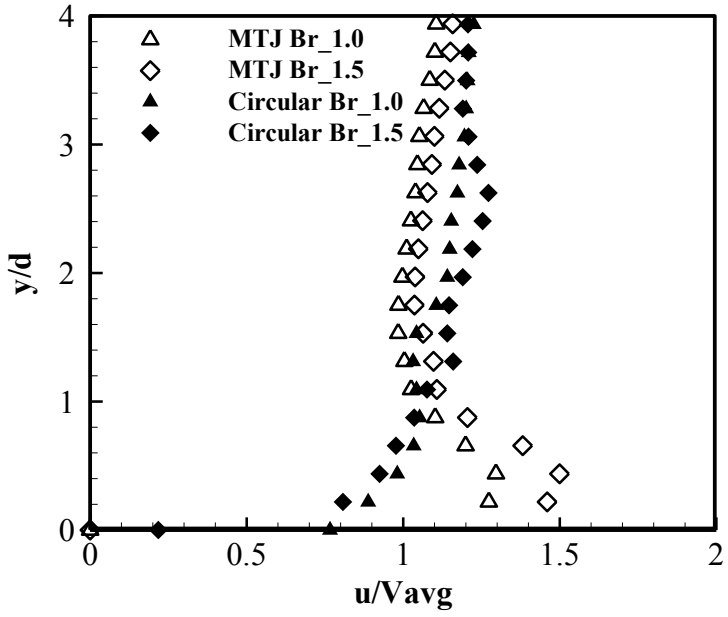

b) x/d = 8

Figure 6.5, Mid-plane (z/d = 0.0) x-axis velocity ratio comparison between the MTJ and the circular hole schemes at two downstream locations and blowing ratios

The difference between tangent and inclined jets injection is very clear in Figs. 6.5a and b. From the figure it is noticeable that the centerline of the jet resulting from the circular hole scheme with inclined injection is at a distance of about 2 hole diameters from the surface at the time the MTJ jet is totally attached to the surface regardless of the blowing ratio value. It is also observable from Fig. 6.5 that there is a difference in the mainstream velocity values downstream the two schemes. The increase in the mainstream velocity with the circular hole scheme case is a result of the increase in the coolant amount injected. The difference in the amount of coolant injected between the two schemes is a result of the difference in the exit area between the two schemes.

6.2. Vorticity Distributions Downstream the MTJ Scheme with Injection

The previously mentioned velocity distributions result in vorticity distributions that highly affect the HTC performance downstream the schemes and as a result affect the net film cooling performance. Fig. 6.6 is the dimensionless vorticity distributions comparison between the MTJ and the circular hole schemes in the near injection region, x/d = 2. It is clear from the figure that, as the blowing ratio increases the vortex intensity increases which is a result of the increased velocity gradients in the shear layer between the main and the secondary streams. Moreover, it is noticeable that the vorticity distribution downstream the circular hole scheme is clearer than the corresponding vorticity distribution downstream the MTJ scheme. The vorticity downstream the circular hole scheme is represented in the presence of a Counter Rotating Vortex Pair (CRVP) surrounding the injection location with significantly increasing intensity with blowing ratio increase. Downstream the MTJ scheme, CRVP are also observable; however, they are not strong as the case of the circular hole schemes. The CRVP surrounding the MTJ scheme are surrounded with randomly distributed vortices resulting in the wake region behind the scheme lip.

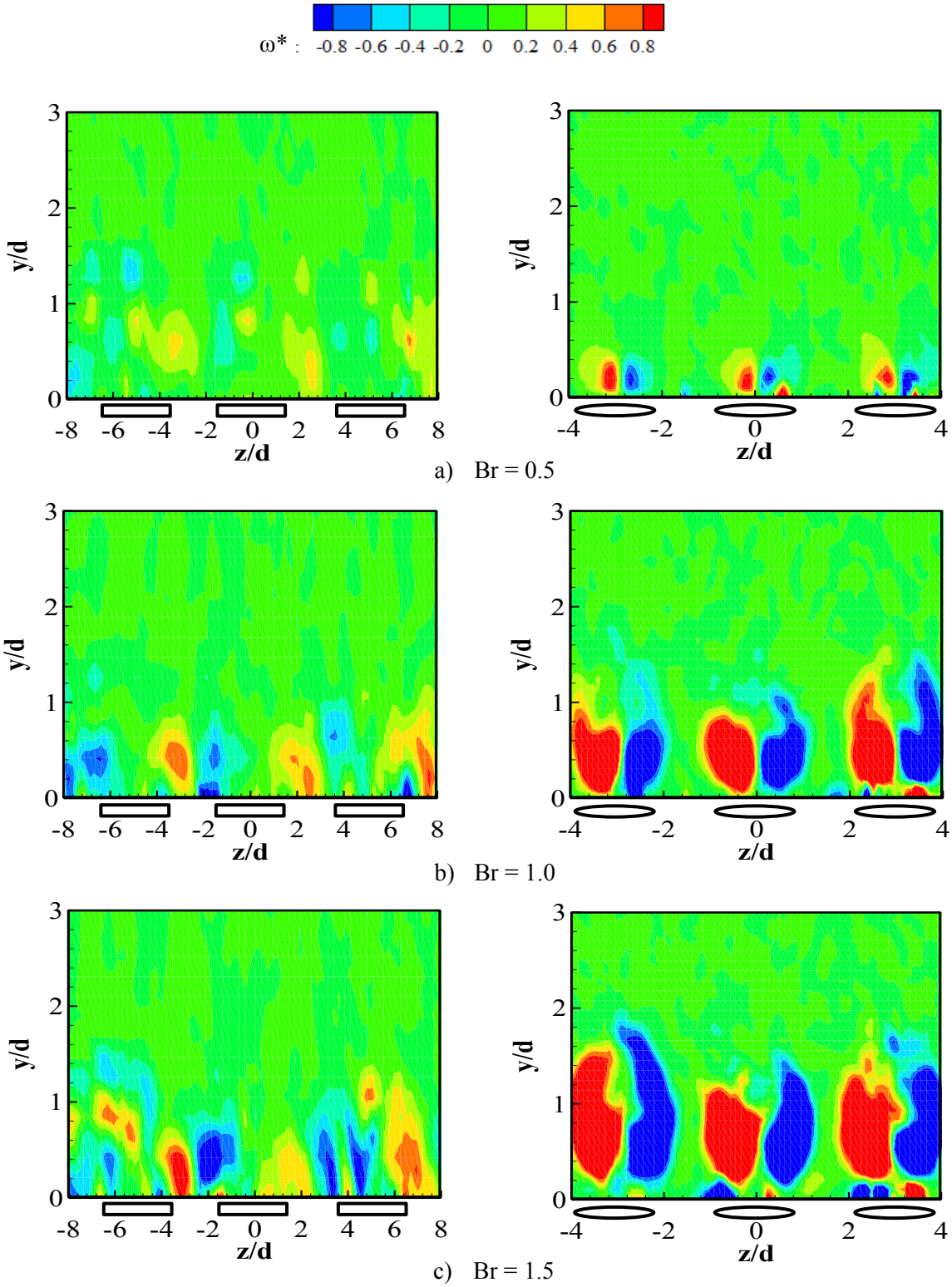

Figure 6.6, Dimensionless vorticity distribution at x/d = 2.0 for the MTJ and the circular hole schemes at different blowing ratios

By comparing the vorticity contours of the MTJ scheme in Fig. 6.6 and the velocity contours in Fig. 6.2, it is clear that the locations of the CRVP in Fig. 6.6 are the locations of maximum velocity gradients in the intermediate gaps between adjacent jets. The latter is the reason of the fixed CRVPs centers locations in the z-directions at different blowing ratios. However, the changes in the CRVPs centers occur in the y-direction as it get closer to the surface with blowing ratio increase. This is a result of the increased velocity gradients between the secondary and the mainstreams close to the surface as the flow in this region is mainly derived by the shear from adjacent jets. Vice versa, the centers of the CRVPs accompanying the circular hole schemes change in both y and z directions with blowing ratio increase due to the increased secondary jet size and momentum. Moreover, the kidney shape of the vortex pair gets clearer with blowing ratio increase. Besides the main CRVPs that accompany the injection from circular hole schemes, small vortices appear attached to the surface beneath the main CRVP and opposite to them in direction. This is a result of the interaction between the entrained mainstream beneath the secondary jet and the lower surface of the secondary jet. The difference in the CRVPs location between the MTJ and the circular hole schemes is also clear in Fig. 6.6. The vortex pair that surrounds the circular hole scheme jet is located around the jet centerline as a result of the direct interaction with the mainstream. Meanwhile, it is located on the sides of the MTJ scheme jet, where the interaction with the main stream is limited to this region. This is one of the advantages of the MTJ scheme added material. The latter protects the secondary jets from the strong mainstream and limits the interaction between both to the shear layer at the top of the jet and the intermediate regions between adjacent jets.

Far downstream from the injection location, at x/d = 8.0, the vortex structure downstream the MTJ scheme is clearer than that in the region close to the injection location. The latter is due to the absence of the vortices generated behind the scheme lip. At low blowing ratio, Fig. 6.7a, there is not any traces of the CRVPs that appeared at x/d = 2.0 while very weak vortices are

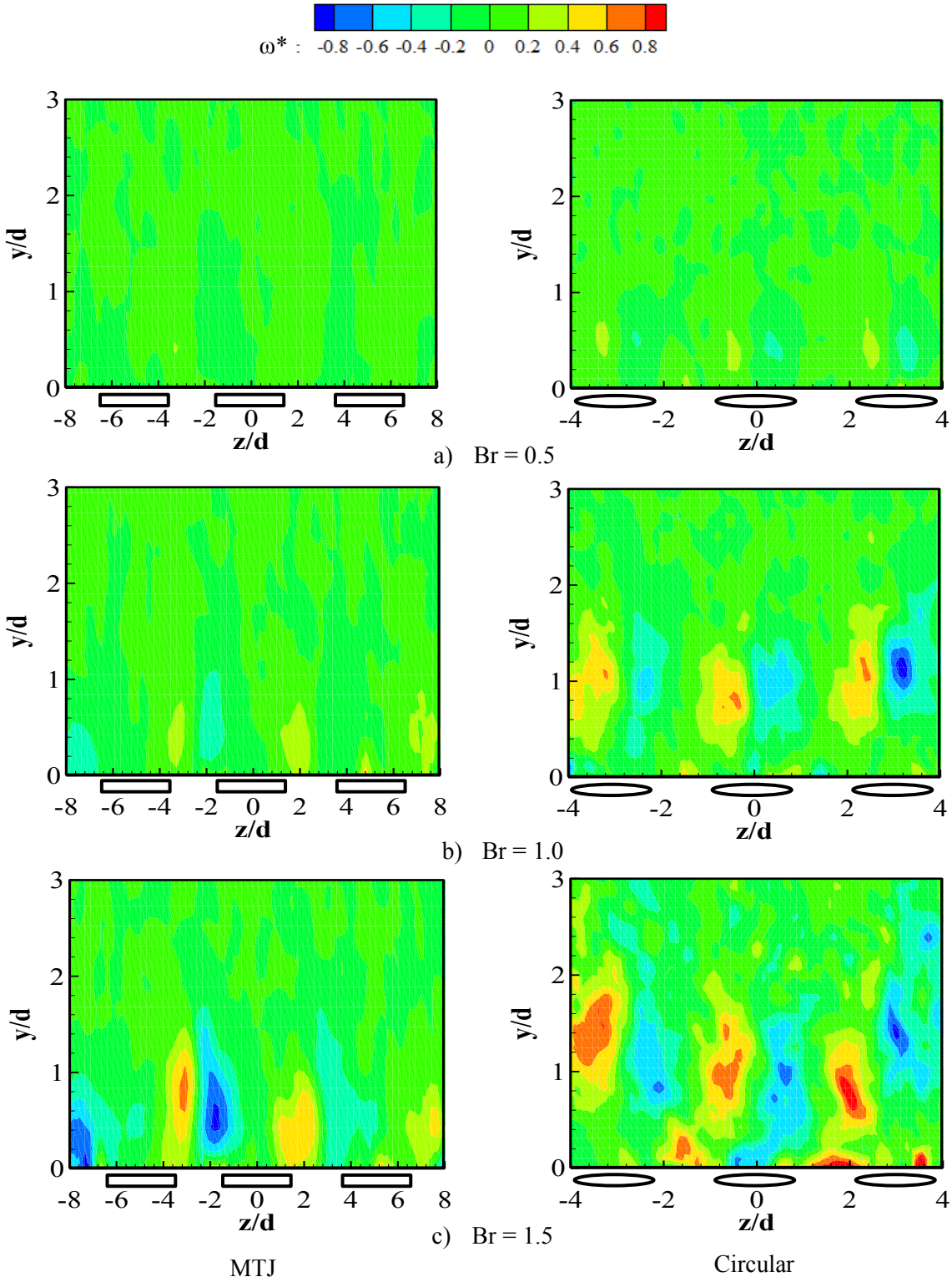

Figure 6.7, Dimensionless vorticity distribution at x/d = 8.0 for the MTJ and the circular hole schemes at different blowing ratios

apparent at Br = 1.0, Fig 6.7b. This is a result of the formation of a continuous secondary film attached to the surface and hence the interaction between the two streams is limited to the interface area at the top region of the film. At Br = 1.5, the CRVPs are still clear with decayed strength and higher y-axis location, compared to the corresponding CRVPs at x/d = 2.0. By re-calling the velocity contours of the MTJ scheme at Br = 1.5, Fig. 6.3c, it is noticeable that the joining of adjacent jets resulted in a thick film region with in-plane secondary velocities directed upward, towards the mainstream. The latter acts as if there is normal secondary injection at these locations. Such in-plane velocities interact with the mainstream and form the CRVPs observed in Fig. 6.7c. The performance of the circular hole scheme jets far from the injection location is not similar to that of the MTJ scheme jets, especially at high blowing ratios. The increased circular jets sizes allow more interaction with the mainstream with reduced velocity gradients. This is clear from the size of the CRVPs and the presence of random vortices distributed all over the flow field.

The previous observations are supported quantitatively through the peak vorticity variation with blowing ratio at different downstream locations presented in Fig. 6.8. From the figure, it is clear that the vortex strength of the vortices accompanying the MTJ scheme is lower than that accompanying the circular hole scheme all the time regardless of the blowing ratio or the downstream location. Close to the injection location and due to the severe interaction between the two cross streams, the circular jet and the mainstream, the vortex intensity is significantly increasing with blowing ratio increase. Far downstream, the peak vorticity of both schemes at different blowing ratios are very close. With the MTJ scheme, the only blowing ratio at which a clear difference in the vorticity value is observable is Br = 1.0. This could be related to the presence of the secondary film without the presence of the too much coolant mass moving towards the mainstream as the case of Br = 1.5 and hence the interaction between the two streams is at minimum. The latter is an indication that the film cooling performance of the MTJ scheme at

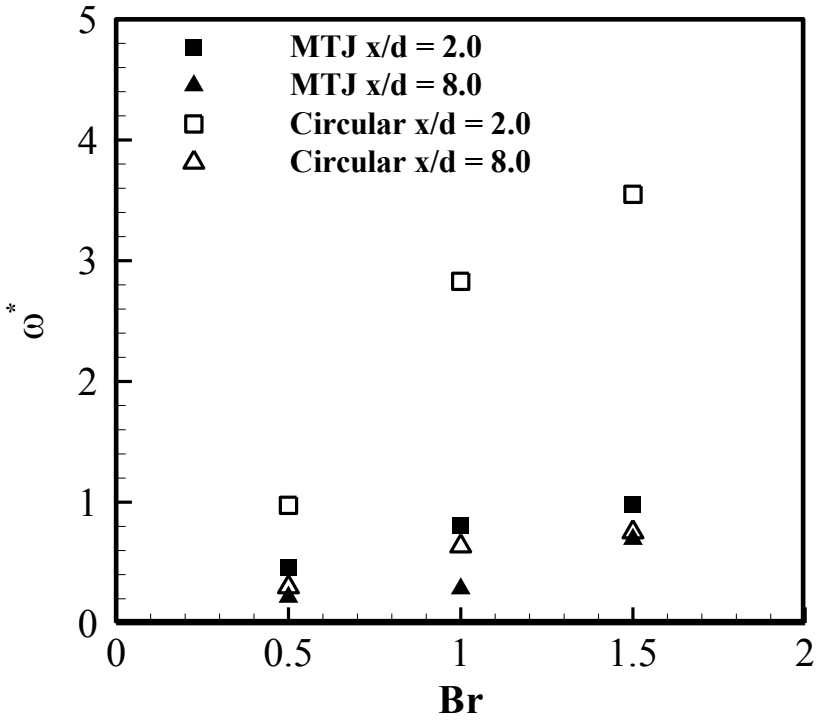

Figure 6.8, Peak vorticity variation with blowing ratio increase at different x/d locations for both MTJ and circular hole schemes

Br = 1.0 is expected to be optimal.

If the vortex structure accompanying the MTJ is only the one presented in the y-z plane, Figs. 6.6 to 6.8, it could be concluded that the film cooling performance of the scheme will be directly proportional to the blowing ratio. However, by examining the flow structure in the x-y plane, Fig. 6.9, it is obvious that the previous conclusion is not valid. The z-axis vortex, ω_z, generated at the interface layer between the two streams has a significant impact on the film cooling performance of the scheme as the vortex strength increases considerably with blowing ratio increase. The latter enhances the mixing between the two streams and the turbulence intensity close to the surface. This in turn, increases the film temperature and the HTC. Moreover, the location of maximum vorticity with Br = 1.5 is closer to the surface than the corresponding maximum vorticity location with Br = 1.0. When the impact of the peak vorticity location is added to the impact of the vorticity values, the film cooling performance will be worse.

6.3. The MTJ Scheme Cooling performance Based on the Current Flow Field Characteristics

The main aim of investigating the flow field characteristics downstream the scaled-up MTJ scheme is to provide more explanations to the observed film cooling performance downstream the MTJ scheme. The two main geometrical differences between the MTJ scheme and the scaled-up one are the size of both schemes and the geometry at which each scheme was investigated. The geometrical ratios of both schemes are identically the same; however, the MTJ scheme critical dimensions are in the micro scale while the scaled-up MTJ scheme critical dimensions are in the macro scale. The impact of such point is expected to be clear in the intensity of different vortices accompanying the jets of both schemes. Based on the results of Gau et al. (2009), the vortices intensities accompanying micro jets are expected to be less than those accompanying

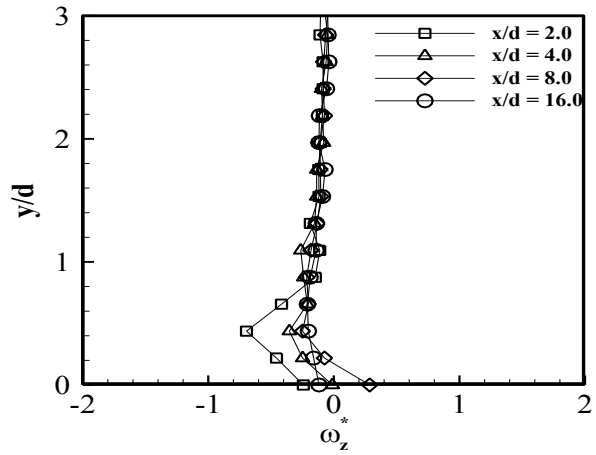

a) Br = 0.5

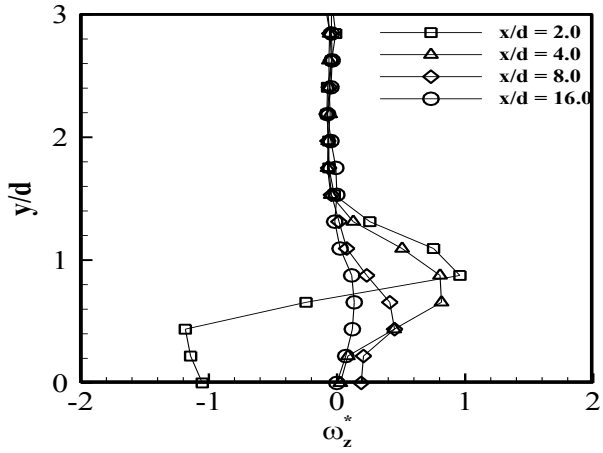

b) Br = 1.0

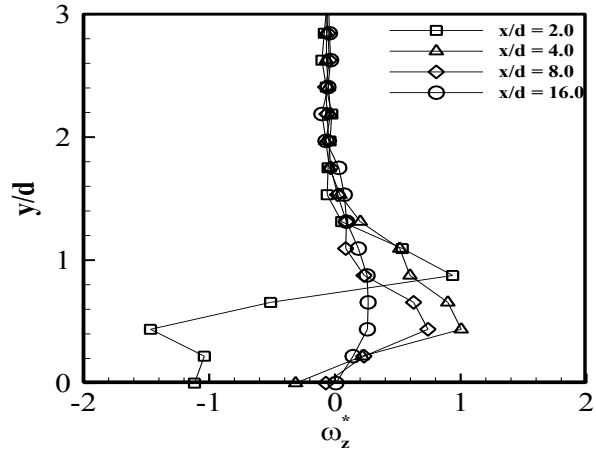

c) Br = 1.5

Figure 6.9, Dimensionless z- axis vorticity distribution at the mid-x-y plane (z/d = 0.0) for the MTJ scheme at different blowing ratios and downstream locations

macro jets. This in turn affects the penetration depth of the jet and the HTC. A micro sized jet is expected to penetrate much deeper than a macro one, while the HTC augmentation due to the injection from a micro scaled scheme is expected to be less than the corresponding augmentation due to the injection from a macro scaled one. The secondary jet penetration depth is not one of the parameters under investigation in the present study. Moreover, investigating the performance of a film cooling scheme over an actual airfoil is expected to produce relatively different results, quantitatively, than investigating its performance over a flat plate. This is due to the differences in velocities and pressure distributions between the two cases. The airfoil vane on which the film cooling performance of the MTJ scheme was investigated is a subsonic one and the velocity distribution on the pressure side is not characterized with significant changes with downstream distance from the leading edge to the trailing edge. Based on this it could be concluded that assuming similarity in the film cooling performance of both schemes, from trend point of view, is practically acceptable.

When the MTJ scheme effectiveness performance was examined over the airfoil vane pressure side, enhancement in the effectiveness performance was observed when the blowing ratio was increased from 0.5 to 1.0. Meanwhile, when the blowing ratio was increased from 1.0 to 1.5 the observed enhancement in the effectiveness was less than that observed when the blowing ratio was increase from 0.5 to 1.0. Based on the flow field characteristics, the previous performance is totally explainable. When the blowing ratio was increased from 0.5 to 1.0, enhancement in the film characteristics is observable without significant enhancement in the vorticity strength. This in turn provides extra thermal protection represented in the effectiveness enhancement. The enhancement in the film characteristics with blowing ratio increase from 1.0 to 1.5 is also noticeable which helps enhance the effectiveness; however, it is accompanied with vorticity strength enhancement as well. The net effectiveness performance is dependent on both factors. The latter resulted in reduced effectiveness enhancement with blowing ratio increase from

1.0 to 1.5, compared to the effectiveness enhancement with blowing ratio increase from 0.5 to 1.0. The reduced effectiveness performance of the MTJ scheme with blowing ratio increase beyond unity is not unique as it was the case with almost all previously proposed slot schemes.

The HTC performance downstream the MTJ over the airfoil vane pressure side was opposite to the previously mentioned effectiveness performance. When the blowing ratio was increased from 0.5 to 1.0 slight HTC augmentation was observed. This is explainable throughout the vortex structure downstream the MTJ scheme. The vorticity enhancement with blowing ratio increase from 0.5 to 1.0 is not significant and is accompanied with enhanced film characteristics. Moreover, the vorticity peak is not very close to the surface. Those factors together result in enhanced effectiveness performance without significant HTC augmentations. With blowing ratio increase from 1.0 to 1.5, significant HTC augmentation was observed downstream the MTJ scheme. The vorticity behavior in the x-y plane downstream the MTJ scheme, Fig. 6.9, explains this performance. The vorticity strength downstream the MTJ increases considerably with blowing ratio increase and the gets closer to the surface at the same time. This in turn enhances the turbulence too much close to the surface which results in HTC augmentation.

6.4. Summary

The flow field characteristics downstream the MTJ scheme, was investigated using the PIV technique over a flat plate. The flow field characteristics downstream the MTJ scheme was compared to the corresponding flow field characteristics downstream a circular hole scheme under the same test conditions. Three different blowing ratios, calculated based on the scheme exit area, were considered, 0.5, 1.0 and 1.5. The density ratio during all investigations was unity and the average turbulence intensity was 8%. The Reynolds Number was 1.16E5, based on the free stream velocity and the main duct hydraulic diameter.

The investigation showed that the flow field characteristics downstream the MTJ scheme, are totally different than the corresponding characteristics downstream the circular hole scheme. From velocity point of view, the MTJ scheme supplies the jet parallel to the surface and it keeps attached to the surface till far downstream distances, regardless of the blowing ratio value. Moreover, the lateral expansion angles of the scheme help combine the jets from neighboring holes very close to the scheme exit and perform a continuous film similar to that of continuous slot schemes. Such advantage gives the MTJ scheme superiority over both, circular hole schemes from continuous film formation point of view and the continuous slot schemes from material strength point of view. The case is different with the circular hole scheme as the jet lifts from the surface and penetrates into the mainstream at relatively low blowing ratios, $Br \geq 1$.

Similar to the velocity distribution, the vortical structures downstream both schemes are totally different. The MTJ scheme jet is accompanied with two CRVPs with relatively low intensity, when compared to the corresponding CRVPs of the circular hole scheme, in the lateral plane and another vortex in the shear layer between the secondary jet and the mainstream parallel to the jet axis. The vortex at the interface between the secondary film and the mainstream is claimed to be the main contributor to the reduction in the film cooling effectiveness of the MTJ scheme at blowing ratios greater than unity. The vortex entrains the main stream inside the secondary film and enhances the turbulence intensity close the surface and the HTC accordingly. For the circular hole scheme, the vortex structure is very complicated especially when the jet lifts off the surface as it is surrounded with the mainstream from all direction and the interaction is at maximum and so the vortex intensity.

Chapter 7

Closing

7.1. Conclusions and Contributions

The inclination angle of the coolant supply scheme, and the shape and size of the exit area are the typical geometric parameters that significantly affect the scheme performance. Zero inclination angle, tangential secondary jet injection, has been proven by many researchers to be the best injection scenario. Meanwhile, a micro sized scheme provides better secondary jet penetration and less turbulence enhancement than a macro sized one. Moreover, designing a film cooling scheme in the form of discrete-holes arrangements reduces the harmful impact on the component material strength that usually accompanies continuous slot schemes. Besides, adding lateral expansion angles to the scheme exit helps spreading the secondary jet in the lateral direction and provides enhanced thermal protection. Designing a cooling scheme that combines the advantages of the previously mentioned parameters is the objective of the present study. The Micro-Tangential-Jet (MTJ) scheme is a discrete-holes shaped cooling scheme with micro sized exit height that supplies the jet parallel to the surface. The scheme is provided with lateral expansion angles that help spread the jet in the lateral direction.

Before investigating the performance of the MTJ scheme over an airfoil vane surface using the transient TLC technique, validations of the test facility and the test methodology were conducted. In effect, the present study imitated the test facility of trusted literature works and investigated the same cooling schemes for film cooling performance over a flat plate and over an airfoil. Good agreements were achieved between the results obtained using the current facility

and test methodology and those presented in the reference works. Furthermore, the velocity distribution measurement technique was also validated against reference work and good agreement was achieved as well.

The film cooling performance of one row of MTJ schemes is investigated on both pressure and suction sides of a gas turbine vane using the transient TLC technique. The investigations were carried out at three different blowing ratios on the pressure side 0.5, 1.0 and 1.5 and four different blowing ratios on the suction side 0.25, 0.375, 0.5 and 0.625. All blowing ratios were calculated based on the MTJ scheme exit area. An average density ratio of 0.93, a Reynolds Number of 1.4E5, based on the free stream velocity and the main duct hydraulic diameter (1.2E5 based on the vane true chord), and a turbulence intensity of 8.5% were employed throughout the investigations.

The presence of the MTJ scheme over the airfoil surface did not result in significant changes in the fluid flow characteristics. The maximum recorded disturbance in the Mach number distribution was less than 10% of that when no MTJ on the surface and was limited to a narrow region over the suction side, around the scheme exit location. This is attributed to the small size of the scheme and the well selected locations over the surface. Meanwhile, the MTJ scheme showed superior film cooling performance over the airfoil vane pressure and suction sides. The achieved effectiveness downstream the MTJ scheme was much higher than that achieved using normal inclined angle shaped schemes, with the same coolant amount being supplied in all cases. Additionally, the effectiveness performance of the MTJ scheme on the suction side was better than the corresponding performance on the pressure side. The latter was due to the reduced pressure over the suction side, compared with the pressure side, and hence to the ability of the secondary jet to penetrate deeper inside the main stream without significant mixing. The effectiveness distribution downstream the MTJ scheme was characterized with superior lateral spreading over both pressure and suction surfaces. This helps reducing the thermal stresses that

accompany the coolant injection from separate holes. The measurements showed similarity in the characteristics of the 2-D film downstream the MTJ scheme and the one that accompanies the injection from continuous slot schemes. The noticeable difference between the two cases, the MTJ and the continuous slot, was the distance needed for the 2-D film to be formed. The latter is formed downstream the continuous slot directly at the injection location. However, with the MTJ scheme a specific distance from the scheme exit is needed for the film to be formed. The length of this distance depends on the value of the blowing ratio.

The investigations showed that the presence of the MTJ scheme over the vane pressure or suction sides did not result in significant HTC augmentation, especially at blowing ratios less than unity. Over the pressure side, the only blowing ratio that resulted in significant HTC augmentation was Br = 1.5. This was attributed to the significantly enhanced turbulence downstream the scheme at this high blowing ratio. Meanwhile, on the suction side, the HTC augmentation at all investigated blowing ratios was not significant. This could be related to the facts that all investigated blowing ratios were less than unity and the flow over the suction side was fully turbulent and hence the presence of the scheme did not affect the flow characteristics significantly.

The NHFR parameter was used to judge the overall performance of the MTJ scheme, compared to other shaped schemes that have been previously proposed and investigated in literature. Significant NHFR enhancement downstream the MTJ scheme was recorded, in comparison to other shaped schemes. Furthermore; on the pressure side, the optimal NHFR downstream the MTJ scheme was recorded at a blowing ratio of one. This is because the enhancement in the effectiveness at higher blowing ratios is followed by a significant HTC augmentation. Meanwhile, the NHFR showed an increasing trend over the suction side for the investigated blowing ratios. However, the rate of NHFR enhancement was decaying while the

blowing ratio was getting closer to unity. This indicates that a blowing ratio of unity is expected to give optimal film cooling performance over the suction side as well as the pressure side.

To help provide more explanations to the enhanced film cooling performance of the MTJ scheme, the flow field characteristics downstream a scaled up model were investigated using the PIV technique over a flat plate. Three different blowing ratios, calculated based on the scheme exit area, were considered, 0.5, 1.0 and 1.5. A density ratio of unity, a Reynolds number of 1.16E5, and a turbulence intensity of 8% were employed throughout all investigations. From velocity distribution point of view, the MTJ scheme supplies the jet parallel to the surface and keeps it attached to the surface until it reaches far downstream distances, regardless of the blowing ratio value. Moreover, the lateral expansion angles of the scheme help combine the jets from neighboring holes very close to the scheme exit and perform a continuous film similar to that of continuous slot schemes. Such an advantage gives the MTJ scheme superiority over circular hole schemes from continuous film formation point of view, and superiority over continuous slot schemes from material strength point of view. Furthermore, the MTJ scheme jet is accompanied with a CRVP of low intensity relatively to the corresponding CRVP of the circular hole scheme. Another vortex in the shear layer between the secondary jet and the mainstream parallel to the jet axis is observed as well for the MTJ scheme. This vortex is claimed to be the main contributor to the reduction in film cooling effectiveness of the MTJ scheme at blowing ratios greater than unity. The vortex entrains the main stream inside the secondary film and enhances the turbulence intensity close the surface and the HTC accordingly.

Two main challenges accompany the previously mentioned superior film cooling performance of the MTJ scheme. The first challenge is the increased pressure drop across the MTJ schemes especially at high blowing ratios. Increasing the diameter of the supply micro tube or reducing its length, while keeping the exit slot height constant, is expected to overcome this disadvantage. The second challenge is the application of the MTJ scheme to airfoils under real

engine conditions. The added material to the surface results in aerodynamic losses therefore keeping the height of the scheme at a minimum is important. To minimize the scheme height, the lip thickness should be as small as possible. However, a very thin lip may induce thermal stresses. In this case, a compromise between the gain in thermal resistance and the loss in aerodynamic performance and film cooling is required, and it is up to the designer to decide upon the optimal lip thickness.

7.2. Recommendations

7.2.1. MTJ Scheme Dimensions Optimization

The MTJ scheme showed superior film cooling performance over the airfoil vane. However; a comprehensive CFD study is recommended to optimize the dimensions of the MTJ scheme for superior film cooling performance and minimum aerodynamic impact over the vane surface. The scheme location over the pressure and the suction sides, multiple row injection, lip thickness, scheme height and width, pitch to diameter ratio, and the lateral expansion angles, are all factors that affect the scheme performance.

7.2.2. PIV Investigations over Airfoil Surface

The PIV investigations presented in the current study were conducted over a flat plate downstream the MTJ scheme. Changing the test geometry is not expected to have significant impact on the obtained results; however, conducting the flow field investigations over a vane geometry is preferable. Conducting PIV investigations over a vane geometry requires replacing the currently available calibration target with a smaller one. Moreover, modifying the currently available traverse with a 3D one is also essential as this will help in the fine adjustment of the cameras and the laser locations to match the small size of the vane geometry.

References

[1] V. Aga, M. Rose and Reza S. Abhari, “Experimental flow structure investigation of compound angled film cooling”, J. of Turbomachinery, 130 (2008) 031005.

[2] P.A. Berger and J.A. Liburdy, “Near-field investigation into the effects of geometry and compound angle on the flow field of a row of film cooling”, ASME Gas Turbine, (1998) 98-GT-279.

[3] S. Bernsdorf, M.G. Rose and R.S. Abhari, “Experimental validation of quasisteady assumption in modeling of unsteady film-cooling”, J. of Turbomachinery, 130 (2008) 011022.

[4] G. Bittlinger, A. Schulz and S. Wittig, "Film cooling effectiveness and heat transfer coefficients for slot injection at high blowing ratios," ASME Paper, (1994) 94-GT-182.

[5] F. Burggraf and R.W. Huffmeier, "Film effectiveness and heat transfer coefficient downstream of a metered injection," Proceedings of the ASME, (1973) 73-HT-31.

[6] J. Chappell, P. Ligrani, S. Sreekanth and T. Lucas, "Suction-Side Gill Region Film Cooling: Effects of Hole Shape and Orientation on Adiabatic Effectiveness and Heat Transfer Coefficient", ASME J. of Turbomachinery, 132 (2010) 031022.

[7] J.H. Chin, S.C. Skirvin, L.E. Hayes and A.H. Silver, “Adiabatic wall temperature downstream of a single, tangential slot,” ASME Paper, (1958) 58-A-107.

[8] W. Colban, A. Gratton, K.A. Thole and M. Haendler, “Heat transfer and film-cooling measurements on a stator vane with fan-shaped cooling holes”, ASME J. of Turbomachinery, 128 (2006) 53-61.

[9] W. Colban and K. Thole, “Influence of hole shape on the performance of a turbine vane endwall film-cooling scheme” Int. J. Heat and Fluid Flow, 28 (2007) 341-356.

[10] W. Colban, K. A. Thole and M. Haendler, "Experimental and computational comparisons of fan-shaped film cooling on a turbine vane surface," J. of Turbomachinery, 129 (2007) 23-31.

[11] J.E. Dees, D.G. Bogard and R.S. Bunker, "Heat Transfer Augmentation Downstream of Rows of Various Dimple Geometries on the Suction Side of a Gas Turbine Airfoil," J. of Turbomachinery, 132 (2010) 031010.

[12] J. Dittmar, A. Schulz and S. Wittig, "Assessment of various film-cooling configurations including shaped and compound angle holes based on large-scale experiments", J. of Turbomachinery, 125 (2003) 57-64.

[13] J. Dittmar, A. Schulz and S. Wittig, “Adiabatic effectiveness and heat transfer coefficient of shaped film cooling holes on a scaled guide vane pressure side model” Int. J. of Rotating Machinery, 10/5 (2005) 345–354.

[14] J.P. Downs and K.K. Landis, "Turbine cooling systems design - past, present and future", ASME Paper, (2009) GT2009-59991.

[15] S.V. Ekkad, H. Nasir and S. Acharya, "Film cooling on a flat surface with a single row of cylindrical angled holes: Effect of discrete tabs", American Society of Mechanical Engineers, Heat Transfer Division, 366 (2000) 3-12.

[16] S.V. Ekkad and J.-C. Han, “A transient liquid crystal thermography technique for gas turbine heat transfer measurements”, Meas. Sci. Technol., 11 (2000) 957–968.

[17] T. Elnady, W. Saleh, I. Hassan, L. Kadem and T. Lucas, “Experimental investigations of louver cooling scheme on gas turbine vane pressure side”, Proceedings of ASME IHTC, (2010) IHTC14-22398.

[18] T. Elnady, I. Hassan, L. Kadem and T. Lucas, “Experimental investigations of louver cooling scheme on gas turbine vane suction side”, Proceedings of ASME Power Conference, (2010) POWER2010-27227.

[19] Z. Gao, D.P. Narzary and J.-C. Han, "Film-cooling on a gas turbine blade pressure side or suction side with compound angle shaped holes," J. of Turbomachinery, 131(2009) 1-11.

[20] R.J. Goldstein, R.B. Rask and E.R.G. Eckert, "Film Cooling With Helium Injection into an Incompressible Air Flow", Int. J. Heat Mass Transfer, 9 (1966) 1341-1350.

[21] R.J. Goldstein, E.R.G. Eckert and F. Burggraf “Effects of hole geometry and density on three dimensional film cooling”, Int. J. Heat and Mass Transfer, 17 (1974) 595-607.

[22] J.P. Farmer, D.J. Seager and J. A. Liburdy, “The Effect of shaping inclined slots on film cooling effectiveness and heat transfer coefficient”, ASME paper, (1997) 97-GT-339

[23] C.O. Folayan and J.H. Whitelaw, "Effectiveness of combined tangential and normal film cooling with finite", Proceedings of the ASME, (1976) 76-HT-30.

[24] C. Gau, C.H. Shen and Z.B. Wang, "Peculiar phenomenon of micro-free-jet flow", J. of Physics of Fluids, 21/9 (2009) 092001.

[25] M. Gritsch, A. Schulz and S. Wittig, "Adiabatic wall effectiveness measurements of film-cooling holes with expanded exits", ASME J. of Turbomachinery, 120 (1998) 549-556.

[26] M. Gritsch, A. Schulz and S. Wittig, "Film-cooling holes with expanded exits: Near-hole heat transfer coefficients," Int. J. of Heat and Fluid Flow, 21 (2000) 146-155.

[27] M.G. Ghorab, I.G. Hassan and T.Lucas, "An experimental investigation of film cooling performance of louver scheme", Int. J. of Heat and Mass Transfer, 54 (2011) 1387-1399.

[28] K.L. Harrison, J.R. Dorrington, J.E. Dees, D.G. Bogard and R. S. Bunker, "Turbine airfoil net heat flux reduction with cylindrical holes embedded in a transverse trench", J. of Turbomachinery, 131 (2009) 011012.

[29] J.P. Hartnett, R.C. Birkebak and E.R.G. Eckert, "Velocity distributions, temperature distributions, effectiveness and heat transfer for air injected through a tangential slot into a turbulent boundary layer". J. Heat Transfer, 83 (1961) 293–306.

[30] J.E. Hatch and S.S. Papell, "Use of a theoretical flow model to correlate data for film cooling on heating an adiabatic wall by tangential injection of gases of different fluid properties", NASA TN D-130, (1959).

[31] J.D. Heidmann and S. Ekkad, "A novel anti-vortex turbine film-cooling hole concept," J. of Turbomachinery, 130 (2008) 031020-1.

[32] A. Hoffs, U. Drost and A. Bolcs, "Investigation of Effectiveness and Heat Transfer on a Showerhead-Cooled Cylinder," Proceedings of the ASME Turbo Expo, (1997) 97-GT-69.

[33] A. Immarigeon and I. Hassan, "An advanced impingement/film cooling scheme for gas turbines - numerical study," Int. J. of Numerical Methods for Heat & Fluid Flow, 16 (2006) 470-493.

[34] S.C. Kacker and J.H. Whitelaw, "The effect of slot height and slot turbulence intensity on the effectiveness of the uniform density two dimensional wall jet," J. of Heat Transfer, 70/4 (1968) 469-475.

[35] S.J. Kline and F.A. McClintock, "Describing uncertainties in Single-Sample Experiments," ASME Mechanical Engineering, 75 (1953) 3-8.

[36] K. Kusterer, D. Bohn, T. Sugimoto and R. Tanaka, "Double-jet ejection of cooling air for improved film cooling", J. of Turbomachinery, 129 (2007) 809-815.

[37] H.-W. Lee, J.J. Park and J.S. Lee, “Flow visualization and film cooling effectiveness measurements around shaped holes with compound angle orientation”, Int. J. of Heat and Mass Transfer, 45 (2002) 145-156.

[38] H.M. Li, O. Hassan and I. Hassan, “The effects of counter rotating vortex pairs intensity on film cooling effectiveness” Proceedings of the ASME IMECE, (2011) IMECE2011-64400.

[39] P.L. Li, H.S. Ko, D.Z. Jeng, C.W. Liu and C. Gau, "Micro film cooling performance", Int. J. of Heat and Mass Transfer, 52 (2009) 5889-94.

[40] G.-C. Li and W. Zhang, "Improving film cooling performance by using one-inlet and double-outlet hole," Journal of Thermal Science, 19 (2010) 430-437.

[41] D.N. Licu, M.J. Findlay, I.S. Gartshore and M. Salcudean, “Transient heat transfer measurements using a single wide-band liquid crystal test”, Transactions of the ASME, 121 (2000) 546-552.

[42] C.L. Liu, H.R. Zhu, J.T. Bai and D.C. Xu, " Film cooling performance of converging slot-hole rows on a gas turbine blade", Int. J. of Heat and Mass Transfer, 53 /23-24 (2010) 5232-41.

[43] C.L. Liu, H.R. Zhu, J.T. Bai and D.C. Xu, "Film cooling performance of converging-slot holes with different exit-entry area ratios", ASME J. of Turbomachinery, 133/1 (2011) 011020-11.

[44] C.L. Liu, H.R. Zhu, J.T. Bai and D.C. Xu, "Experimental and numerical investigation on the film cooling of waist-shaped slot holes comparing with converging slot holes", ASME J. of Turbomachinery, 134/1 (2012) 011021-11.

[45] Y. Lu, D. Allison and S.V. Ekkad, “Turbine Blade Showerhead Film Cooling: Influence of Hole Angle and Shaping,” International Journal of Heat and Fluid Flow, 28/5 (2007) 922-93.

[46] Y. Lu, A. Dhungel, S.V. Ekkad and R.S. Bunker, "Effect of trench width and depth on film cooling from cylindrical holes embedded in trenches", ASME J. of Turbomachinery, 131 (2009) 1-13.

[47] Y. Lu, A. Dhungel, S.V. Ekkad and R.S. Bunker, "Film cooling measurements for cratered cylindrical inclined holes", ASME J. of Turbomachinery, 131(2009) 1-12.

[48] G.I. Mahmood, R. Gustafson and S. Acharya, “Experimental investigation of flow structure and Nusselt number in a low-speed linear blade passage with and without leading-edge fillets”, J. of Heat Transfer, 127 (2005) 499-512.

[49] M. Martiny, A. Schulz, S. Wittig and M. Dilzer, "Influence of a mixing-jet on film cooling," ASME Turbo Expo, (1997) 97-GT-247

[50] L. Matthews and J.H. Whitelaw, "Film Cooling effectiveness in the presence of a backward-facing step," Transactions ASME, Series C, J. of Heat Transfer, 95 (1973) 135-137.

[51] E.L. McGrath and J.H. Leylek, “Physics of hot cross flow ingestion in film cooling” ASME Turbo Expo, (1998) GT1998-48695.

[52] D.E. Metzger, P. A. Kuenstler, P. L. Hale and J. Anderson, “Influences of upstream injection and intermediate panel temperature on multiple slot film cooling”, 6th Int. Heat Transfer Conference, (1978) Toronto, Canada, 7-11 August.

[53] S. Mhetras, J.-C. Han and R. Rudolph, "Effect of flow parameter variations on full coverage film-cooling effectiveness for a gas turbine blade," ASME Turbo Expo, (2007) GT2007-27071.

[54] B.R. Munson, D.F. Young, T.H. Okiishi, “Fundamentals of fluid mechanics” 5th edition (2006), USA, John Wiley and Sons.

[55] H. Nasir, S. Acharya and S. Ekkad, "Improved film cooling from cylindrical angled holes with triangular tabs: Effect of tab orientations", Int. J. of Heat and Fluid Flow, 24 (2003) 657-668.

[56] M.N.R. Nina and J.H. Whitelaw, "Effectiveness of film cooling with three-dimensional slot geometries", J. Eng. Power, 93 (1971) 425-430.

[57] M.D. Polanka, J. M. Cutbirth and D.G. Bogard, “Three component velocity field measurements in the stagnation region of a film cooled turbine vane”, J. of Turbomachinery, 124 (2002) 445-452.

[58] C. Saumweber, A. Schulz and S. Wittig, "Free-stream turbulence effects on film cooling with shaped holes," Transactions of the ASME, J. of Turbomachinery, 125 (2003) 65-73.

[59] C. Saumweber and A. Schulz, "Interaction of film cooling rows: Effects of hole geometry and row spacing on the cooling performance downstream of the second row of holes," J. of Turbomachinery, 126 (2004) 237-246.

[60] J.E. Sargison, S.M. Guo, M.L.G. Oldfield, G.D. Lock and A.J. Rawlinson, "A converging slot-hole film-cooling geometry-Part I: Low-speed flat-plate heat transfer and loss", ASME J. of Turbomachinery, 124/3 (2002) 453-460.

[61] J.E. Sargison, S.M. Guo, M.L.G. Oldfield, G.D. Lock and A.J. Rawlinson, "A converging slot-hole film-cooling geometry-Part II: Transonic nozzle guide vane heat transfer and loss", ASME J. of Turbomachinery, 124/3 (2002) 461-471.

[62] J.E. Sargison, M.L.G. Oldfield, S.M. Guo, G.D. Lock and A.J. Rawlinson, "Flow visualization of the external flow from a converging slot-hole film-cooling geometry," J. Experiments in Fluids, 38 (2005) 304-18.

[63] R.A. Seban, "Heat Transfer 6 Effectiveness for Turbulent Boundary Layer with Tangential Fluid Injection," Transactions of the ASME, Series C, J. Heat Transfer, 82 (1960) 303-312.

[64] J.L. Stollery and A.A.M. El-Ehwany, "A Note on the use of Boundary Layer Model for Correlating Film Cooling Data", Int. J. of Heat and Mass Transfer, 8 (1965) 55-65.

[65] K. Takeishi, M. Komiyama, Y. Oda, S. Mori and T. Kitamura, "Study of the thermal and flow fields of shaped film cooling holes", Heat Transfer Research, 42/1 (2011) 83-100.

[66] R.J. Vedula and D.E. Metzger, "A Method for the Simultaneous Determination of Local Effectiveness and Heat Transfer Distributions in Three-Temperature Convection Situations," ASME Turbo Expo, (1991) 91-GT-345.

[67] D. Venneman and K.A. Butesfisch, "The application of temperature sensitive crystals to aerodynamic investigations," European Space Agency, ESRO-RR-77, Translation of DLR-BD-73-121, 1 973.

[68] K. Wieghardt, "Hot-Air Discharge for De-icing", AAF Translation, Report No. F-TS-glg-Re, (1946), Wright Field.

[69] L.M. Wright, S.T. McClain and M.D. Clemenson, "Effect of density ratio on flat plate film cooling with shaped holes using PSP", ASME J. of Turbomachinery, 133(2011) 041011-1.

[70] L.M. Wright, S.T. McClain and M.D. Clemenson, "Effect of freestream turbulence intensity on film cooling jet structure and surface effectiveness using PIV and PSP", J. of Turbomachinery, 133 (2011) 041023.

[71] C.F. Yang and J.Z. Zhang, "Experimental investigation on film cooling characteristics from a row of holes with ridge-shaped tabs", Experimental Thermal and Fluid Science, 37 (2012) 113-120.

[72] S.K. Waye and D.G. Bogard, “High-Resolution film cooling effectiveness measurements of axial holes embedded in a transverse trench with various trench configurations”, ASME J. of Turbomachinery, 129 (2007) 294-302.

[73] X.Z. Zhang and I. Hassan, "Film cooling effectiveness of an advanced-louver cooling scheme for gas turbines", J. of Thermophysics and Heat Transfer, 20 (2006) 754-763.

[74] L. Zhang and H.-K. Moon, "Turbine blade film cooling study - The effects of film hole location on the pressure side," ASME Turbo Expo, (2007) GT2007-27546.

Publications

Journal Publications

[1] **O. Hassan**, and I. Hassan, "Experimental investigations of the film cooling effectiveness of a Micro-Tangential-Jet Scheme on a Gas Turbine Vane", Int. J. of Heat and Mass Transfer, 61 (2013) 158-171.

[2] **O. Hassan**, and I. Hassan, "Experimental Investigations of the Film Cooling Heat Transfer Coefficient of a Micro-Tangential-Jet Scheme on a Gas Turbine Vane", Int. J. of Heat and Mass Transfer, 64 (2013) 401-417.

[3] **O. Hassan**, and I. Hassan, "Experimental Flow Field Investigations Downstream a Scaled-Up Micro-Tangential-Jet Scheme Using the PIV Technique", Submitted to the ASME Journal of Fluids.

Conference Publications

[1] **O. Hassan,** and I. Hassan, "Experimental investigations of the film cooling performance of a Micro-Tangential-Jet scheme on a gas turbine vane, Part I: Effectiveness", Proceedings of the ASME IMECE2012, IMECE2012-88535.

[2] **O. Hassan,** and I. Hassan, "Experimental investigations of the film cooling performance of a Micro-Tangential-Jet scheme on a gas turbine vane, Part II: Heat transfer coefficient", Proceedings of the ASME IMECE2012, IMECE2012-88541.

[3] **O. Hassan,** and I. Hassan, "Experimental flow field investigations downstream a film cooling scheme over a flat plate using the PIV technique", Draft submitted to the ASME IMECE2013,

[4] H.M. Li, **O. Hassan** and I. Hassan, "The effects of counter rotating vortex pair's intensity on film cooling effectiveness" Proceedings of the ASME IMECE, (2011) IMECE2011-64400.

[5] T. Elnady, **O. Hassan**, I. Hassan, L. Kadem, and T. Lucas, "Experimental investigations of louver cooling scheme on gas turbine vane suction side", Proceedings of ASME Turbo Expo, (2011) GT2011-45585

[6] C. El Ayoubi, **O. Hassan**, W. Ghaly, and I. Hassan, "Aero-thermal optimization and experimental verification for the discrete film cooling of a turbine airfoil" Proceedings of ASME Turbo Expo, (2013) GT2013-95325

Appendix A

Experimental Data Tables

Table A.1, Centerline and laterally averaged effectiveness downstream a circular hole scheme over a flat plate at different blowing ratios and Re = 1.24E5, used for validation with Wright et al. (2011)

x/d	Br = 0.5 Centerline	Br = 0.5 Average	Br = 1.0 Centerline	Br = 1.0 Average
1.00	0.468	0.201	0.199	0.111
2.00	0.457	0.197	0.215	0.107
3.00	0.417	0.186	0.245	0.111
4.00	0.384	0.175	0.223	0.108
5.00	0.350	0.168	0.212	0.108
6.00	0.319	0.161	0.211	0.107
7.00	0.298	0.156	0.198	0.106
8.00	0.298	0.156	0.198	0.106
9.00	0.260	0.147	0.183	0.106
10.00	0.243	0.143	0.174	0.103
11.00	0.222	0.131	0.175	0.097
12.00	0.213	0.125	0.156	0.092
13.00	0.198	0.123	0.143	0.089
14.00	0.189	0.113	0.140	0.084
15.00	0.175	0.108	0.132	0.084
16.00	0.169	0.107	0.127	0.081
17.00	0.160	0.104	0.124	0.079
18.00	0.146	0.101	0.125	0.078
19.00	0.154	0.104	0.115	0.082
20.00	0.148	0.103	0.121	0.082
21.00	0.144	0.101	0.116	0.078
22.00	0.145	0.101	0.129	0.083
23.00	0.139	0.098	0.121	0.082

Table A.2, Centerline and laterally averaged effectiveness downstream fan-shaped scheme over a flat plate at different blowing ratios and Re = 1.24E5, used for validation with Wright et al. (2011)

x/d	Br = 0.5 Centerline	Br = 1.0 Centerline	Br = 0.5 Average	Br = 1.0 Average
1.00	0.590	0.590	0.317	0.301
2.00	0.531	0.531	0.276	0.244
3.00	0.460	0.462	0.242	0.211
4.00	0.421	0.421	0.221	0.192
5.00	0.408	0.416	0.203	0.180
6.00	0.339	0.344	0.187	0.169
7.00	0.307	0.319	0.177	0.167
8.00	0.282	0.301	0.166	0.159
9.00	0.263	0.284	0.156	0.154
10.00	0.251	0.274	0.151	0.153
11.00	0.225	0.255	0.145	0.153
12.00	0.214	0.244	0.137	0.146
13.00	0.199	0.231	0.135	0.146
14.00	0.199	0.228	0.122	0.135
15.00	0.175	0.210	0.112	0.130
16.00	0.172	0.204	0.108	0.126
17.00	0.139	0.180	0.108	0.126
18.00	0.151	0.180	0.100	0.123
19.00	0.146	0.176	0.093	0.116
20.00	0.133	0.165	0.085	0.112
21.00	0.131	0.164	0.078	0.110
22.00	0.119	0.152	0.076	0.108
23.00	0.106	0.144	0.076	0.110
24.00	0.105	0.145	0.073	0.111
25.00	0.116	0.151	0.070	0.108

Table A.3, Centerline and laterally averaged effectiveness downstream fan-shaped scheme over a flat plate at different blowing ratios and Re = 0.7E5, used for validation with Wright et al. (2011)

x/d	Br = 0.5 Centerline	Br = 1.0 Centerline	Br = 0.5 Average	Br = 1.0 Average
1.00	0.518	0.426	0.282	0.216
2.00	0.455	0.362	0.244	0.176
3.00	0.383	0.307	0.208	0.152
4.00	0.336	0.275	0.187	0.138
5.00	0.295	0.252	0.175	0.134
6.00	0.288	0.243	0.167	0.131
7.00	0.264	0.229	0.163	0.130
8.00	0.240	0.214	0.159	0.130
9.00	0.237	0.212	0.154	0.128
10.00	0.224	0.204	0.156	0.131
11.00	0.197	0.188	0.150	0.128
12.00	0.211	0.192	0.139	0.121
13.00	0.181	0.172	0.136	0.120
14.00	0.177	0.171	0.123	0.113
15.00	0.156	0.155	0.111	0.106
16.00	0.157	0.155	0.106	0.104
17.00	0.119	0.134	0.116	0.110
18.00	0.137	0.141	0.114	0.110
19.00	0.149	0.142	0.109	0.106
20.00	0.121	0.131	0.101	0.102
21.00	0.128	0.133	0.105	0.104
22.00	0.127	0.131	0.112	0.108
23.00	0.131	0.131	0.111	0.108
24.00	0.131	0.127	0.111	0.108
25.00	0.139	0.136	0.110	0.106

Table A.4, Mach number distribution around the validation vane, used for the validation with Chappell et al. (2010)

	x/Cx	Ma Without MTJ
Pressure side	62.22	0.192
	40.00	0.158
	11.11	0.100
	0.00	0.000
Suction side	8.89	0.328
	24.44	0.408
	38.89	0.408
	52.22	0.386
	67.78	0.358
	78.89	0.366

Table A.5, Spanwise-averaged effectiveness and HTC over the suction side of airfoil vane surface downstream double rows of circular hole scheme in staggered arrangement, for the validation with Chappell et al. (2010)

x/d	Br = 0.6 Effectiveness	Br = 0.9 Effectiveness	Br = 1.2 Effectiveness	Br = 1.2 HTC
10.55	0.215	0.177	0.117	168.846
11.89	0.216	0.184	0.111	166.516
12.56	0.208	0.177	0.106	165.139
13.90	0.208	0.176	0.107	160.881
15.24	0.204	0.175	0.107	157.296
16.09	0.192	0.171	0.105	158.434
16.94	0.181	0.161	0.097	158.520
17.80	0.174	0.156	0.095	155.984
18.65	0.169	0.153	0.092	159.757
19.50	0.168	0.149	0.088	164.079
20.35	0.160	0.144	0.087	162.269
21.20	0.163	0.144	0.079	163.629
21.89	0.161	0.140	0.079	167.014
22.57	0.158	0.139	0.077	165.144
23.25	0.155	0.140	0.077	160.449
23.93	0.152	0.137	0.076	167.430
24.61	0.148	0.133	0.078	171.280
25.30	0.149	0.134	0.076	165.920
26.00	0.146	0.135	0.077	168.992
26.66	0.142	0.133	0.078	166.436
27.34	0.143	0.130	0.077	167.191
27.97	0.140	0.130	0.077	156.911
28.53	0.144	0.130	0.078	165.778
29.10	0.139	0.129	0.078	171.401
29.67	0.138	0.127	0.078	181.927
30.24	0.138	0.121	0.079	173.603
30.81	0.137	0.131	0.078	171.145
31.37	0.138	0.131	0.079	173.481
31.94	0.138	0.122	0.079	173.817
32.51	0.137	0.126	0.081	176.352
33.08	0.137	0.124	0.080	173.729
33.65	0.136	0.123	0.082	182.105
34.21	0.136	0.122	0.082	176.390
34.78	0.133	0.123	0.081	182.664
35.07	0.134	0.124	0.082	176.787

Table A.6, Experimental 2D and 3D PIV velocity comparison with theoretical

y/d	u/V_{avg} 2D PIV	y/d	u/V_{avg} Theoretical	y/d	u/V_{avg} 3D PIV
0.00	0.279	0.00	0.000	0.00	0.000
0.13	0.683	0.16	0.714	0.21	0.837
0.32	0.789	0.31	0.785	0.42	0.861
0.51	0.826	0.47	0.829	0.84	0.925
0.71	0.865	0.63	0.863	1.05	0.944
0.90	0.894	0.78	0.890	1.26	0.961
1.09	0.925	0.94	0.912	1.68	0.990
1.28	0.941	1.09	0.931	2.10	1.010
1.48	0.965	1.25	0.949	2.31	1.018
1.67	0.977	1.41	0.964	2.52	1.027
1.86	0.996	1.56	0.978	2.73	1.040
2.05	1.026	1.72	0.991	3.15	1.066
2.24	1.034	1.88	1.003	3.57	1.083
2.44	1.048	2.03	1.014	3.78	1.088
2.63	1.059	2.19	1.024	3.99	1.101
2.82	1.066	2.34	1.034	4.20	1.114
3.01	1.077	2.50	1.043		
3.20	1.090	2.66	1.052		
3.40	1.103	2.81	1.060		
3.59	1.115	2.97	1.068		
3.78	1.123	3.13	1.076		
3.95	1.133	3.28	1.083		
		3.44	1.090		
		3.59	1.096		
		3.75	1.103		
		3.91	1.109		
		4.06	1.115		

Table A.7, Mach number distribution around the vane surface with and without the MTJ scheme

	x/Cx	Ma Without MTJ	Ma with MTJ
Pressure side	62.20	0.193	0.179
	42.60	0.128	0.127
	24.90	0.111	0.109
	15.70	0.095	0.091
	2.60	0.051	0.052
	0.00	0.000	0.000
Suction side	10.00	0.237	0.220
	23.20	0.340	0.329
	33.90	0.342	0.379
	42.40	0.338	0.363
	57.30	0.334	0.332
	69.60	0.328	0.326
	81.00	0.323	0.320

Table A.8, Pressure side centerline and spanwise-averaged effectiveness comparison downstream the MTJ scheme at different blowing ratios

x/d	Br = 0.5 Centerline	Br = 1.0 Centerline	Br = 1.5 Centerline	Br = 0.5 Average	Br = 1.0 Average	Br = 1.5 Average
2.92	0.913	0.848	0.854	0.859	0.769	0.735
4.63	0.752	0.733	0.761	0.739	0.698	0.686
6.33	0.667	0.687	0.692	0.628	0.637	0.629
8.03	0.551	0.617	0.623	0.547	0.582	0.580
9.74	0.493	0.560	0.574	0.485	0.534	0.541
11.44	0.461	0.513	0.540	0.448	0.502	0.515
13.15	0.418	0.492	0.526	0.415	0.477	0.489
14.85	0.397	0.460	0.485	0.386	0.450	0.465
16.55	0.375	0.445	0.475	0.369	0.428	0.448
18.26	0.362	0.426	0.453	0.355	0.411	0.434
19.96	0.348	0.406	0.440	0.344	0.400	0.423
21.67	0.322	0.394	0.428	0.328	0.385	0.412
23.37	0.326	0.376	0.415	0.313	0.376	0.404
25.07	0.309	0.379	0.416	0.306	0.370	0.397
26.78	0.316	0.370	0.407	0.301	0.362	0.389
28.48	0.302	0.371	0.403	0.287	0.355	0.383
30.19	0.275	0.353	0.390	0.274	0.347	0.377
31.89	0.267	0.349	0.388	0.265	0.345	0.373
33.59	0.256	0.342	0.380	0.260	0.337	0.366
35.30	0.266	0.360	0.391	0.250	0.330	0.361
37.00	0.256	0.328	0.373	0.246	0.327	0.357
38.71	0.241	0.326	0.369	0.239	0.321	0.353
40.41	0.232	0.313	0.358	0.233	0.319	0.350
42.11	0.225	0.310	0.355	0.224	0.313	0.345
43.82	0.237	0.299	0.347	0.222	0.309	0.342
45.52	0.237	0.343	0.364	0.210	0.303	0.337
47.23	0.215	0.310	0.354	0.202	0.300	0.335

Table A.9, Pressure side spanwise effectiveness distribution downstream the MTJ scheme at different streamwise locations and Br = 0.5

z/d	x/d = 3.0	x/d = 20.0	x/d = 40.0
-12.5	0.741	0.308	0.213
-11.61	0.802	0.317	0.208
-10.71	0.812	0.317	0.244
-9.82	0.846	0.311	0.216
-8.93	0.801	0.314	0.178
-8.04	0.806	0.313	0.214
-7.14	0.847	0.302	0.197
-6.25	0.832	0.302	0.215
-5.34	0.903	0.289	0.194
-4.46	0.921	0.323	0.226
-3.57	0.927	0.349	0.235
-2.68	0.839	0.336	0.214
-1.79	0.877	0.371	0.222
-0.89	0.877	0.338	0.221
0.00	0.913	0.348	0.232
0.83	0.903	0.364	0.245
1.67	0.850	0.348	0.256
2.50	0.860	0.357	0.262
3.33	0.818	0.379	0.239
4.17	0.903	0.361	0.239
5.00	0.929	0.348	0.247
5.83	0.892	0.359	0.251
6.67	0.817	0.380	0.245
7.50	0.870	0.382	0.253
8.33	0.833	0.373	0.249
9.17	0.889	0.360	0.237
10.00	0.882	0.374	0.281
10.83	0.834	0.349	0.247
11.67	0.859	0.360	0.279
12.50	0.876	0.386	0.250

Table A.10, Pressure side spanwise effectiveness distribution downstream the MTJ scheme at different streamwise locations and Br = 1.0

z/d	x/d = 3.0	x/d = 20.0	x/d = 40.0
-12.50	0.657	0.357	0.308
-11.61	0.718	0.378	0.305
-10.71	0.779	0.365	0.303
-9.82	0.761	0.363	0.315
-8.93	0.725	0.369	0.307
-8.04	0.728	0.387	0.325
-7.14	0.727	0.387	0.307
-6.25	0.789	0.385	0.321
-5.34	0.834	0.394	0.315
-4.46	0.868	0.404	0.336
-3.57	0.857	0.408	0.359
-2.68	0.819	0.424	0.340
-1.79	0.761	0.423	0.300
-0.89	0.804	0.412	0.319
0.00	0.848	0.406	0.313
0.83	0.844	0.420	0.339
1.67	0.786	0.402	0.314
2.50	0.735	0.417	0.311
3.33	0.734	0.422	0.316
4.17	0.782	0.402	0.323
5.00	0.824	0.403	0.322
5.83	0.791	0.397	0.304
6.67	0.718	0.406	0.326
7.50	0.710	0.422	0.344
8.33	0.746	0.410	0.322
9.17	0.778	0.393	0.319
10.00	0.803	0.405	0.327
10.83	0.771	0.393	0.319
11.67	0.705	0.408	0.318
12.50	0.681	0.417	0.316

Table A.11, Pressure side spanwise effectiveness distribution downstream the MTJ scheme at different streamwise locations and Br = 1.5

z/d	x/d = 3.0	x/d = 20.0	x/d = 40.0
-12.50	0.577	0.386	0.335
-11.61	0.647	0.406	0.328
-10.71	0.736	0.393	0.326
-9.82	0.761	0.388	0.335
-8.93	0.734	0.394	0.331
-8.04	0.697	0.415	0.350
-7.14	0.690	0.414	0.340
-6.25	0.752	0.421	0.354
-5.34	0.829	0.433	0.352
-4.46	0.864	0.437	0.378
-3.57	0.844	0.444	0.387
-2.68	0.743	0.461	0.366
-1.79	0.729	0.456	0.362
-0.89	0.796	0.449	0.368
0.00	0.854	0.440	0.358
0.83	0.858	0.444	0.373
1.67	0.787	0.427	0.350
2.50	0.669	0.429	0.348
3.33	0.648	0.432	0.348
4.17	0.711	0.420	0.348
5.00	0.769	0.416	0.354
5.83	0.759	0.410	0.334
6.67	0.695	0.415	0.351
7.50	0.636	0.423	0.358
8.33	0.662	0.423	0.343
9.17	0.728	0.412	0.349
10.00	0.772	0.422	0.354
10.83	0.768	0.411	0.344
11.67	0.695	0.422	0.346
12.50	0.632	0.436	0.345

Table A.12, Suction side centerline effectiveness at different blowing ratios downstream the MTJ scheme

x/d	Br = 0.25 Centerline	Br = 0.375 Centerline	Br = 0.5 Centerline	Br = 0.625 Centerline
1.88	0.576	0.712	0.819	0.825
3.76	0.511	0.608	0.718	0.735
5.64	0.405	0.516	0.636	0.651
7.51	0.343	0.453	0.554	0.596
9.39	0.310	0.419	0.535	0.559
11.27	0.278	0.391	0.504	0.537
13.15	0.257	0.368	0.489	0.511
15.03	0.235	0.345	0.467	0.493
16.90	0.226	0.347	0.464	0.478
18.78	0.199	0.314	0.433	0.459
20.42	0.201	0.317	0.439	0.463
21.82	0.184	0.299	0.425	0.448
23.22	0.179	0.281	0.403	0.447
24.62	0.170	0.271	0.396	0.431
26.02	0.178	0.264	0.383	0.424
27.42	0.165	0.276	0.406	0.432
28.82	0.165	0.263	0.392	0.426
30.22	0.161	0.265	0.392	0.407
31.62	0.139	0.248	0.365	0.400
33.02	0.133	0.231	0.350	0.400
34.42	0.155	0.245	0.373	0.411
35.82	0.153	0.250	0.384	0.420
37.22	0.145	0.247	0.372	0.414
38.62	0.147	0.243	0.372	0.410
40.02	0.135	0.222	0.346	0.389
41.42	0.138	0.231	0.342	0.385
42.82	0.153	0.228	0.343	0.394
44.22	0.269	0.245	0.362	0.409
45.52	0.192	0.249	0.378	0.429
46.73	0.128	0.244	0.373	0.422
47.33	0.155	0.243	0.375	0.429
48.54	0.157	0.239	0.374	0.428
49.74	0.135	0.229	0.358	0.408
50.95	0.126	0.233	0.367	0.434
52.16	0.123	0.247	0.378	0.440
53.36	0.148	0.239	0.381	0.447
54.57	0.133	0.238	0.368	0.465
55.77	0.176	0.256	0.383	0.466

Table A.13, Suction side spanwise-averaged effectiveness at different blowing ratios downstream the MTJ scheme

x/d	Br = 0.25 Average	Br = 0.375 Average	Br = 0.5 Average	Br = 0.625 Average
1.88	0.504	0.698	0.855	0.842
3.76	0.448	0.568	0.697	0.722
5.64	0.374	0.490	0.621	0.654
7.51	0.324	0.436	0.558	0.602
9.39	0.285	0.400	0.521	0.564
11.27	0.259	0.373	0.494	0.534
13.15	0.238	0.353	0.473	0.512
15.03	0.217	0.334	0.451	0.488
16.90	0.207	0.296	0.410	0.457
18.78	0.186	0.286	0.399	0.431
20.42	0.187	0.311	0.397	0.453
21.82	0.181	0.287	0.400	0.434
23.22	0.175	0.279	0.391	0.425
24.62	0.168	0.272	0.383	0.416
26.02	0.167	0.259	0.370	0.396
27.42	0.160	0.262	0.373	0.405
28.82	0.161	0.258	0.367	0.397
30.22	0.153	0.251	0.360	0.392
31.62	0.146	0.248	0.356	0.386
33.02	0.145	0.244	0.353	0.385
34.42	0.152	0.242	0.350	0.384
35.82	0.144	0.241	0.349	0.378
37.22	0.146	0.239	0.346	0.377
38.62	0.157	0.237	0.344	0.373
40.02	0.141	0.233	0.340	0.371
41.42	0.142	0.233	0.341	0.372
42.82	0.161	0.255	0.361	0.392
44.22	0.170	0.238	0.345	0.377
45.52	0.149	0.239	0.348	0.378
46.73	0.141	0.234	0.342	0.374
47.33	0.148	0.235	0.342	0.375
48.54	0.152	0.234	0.341	0.373
49.74	0.173	0.229	0.343	0.388
50.95	0.146	0.227	0.334	0.368
52.16	0.148	0.237	0.347	0.377
53.36	0.143	0.245	0.352	0.389
54.57	0.146	0.251	0.363	0.391
55.77	0.139	0.255	0.371	0.403

Table A.14, Suction side spanwise effectiveness distribution downstream the MTJ scheme at different streamwise locations and Br = 0.25

z/d	x/d = 4.0	x/d = 25.0	x/d = 50.0
-13.00	0.390	0.172	0.127
-12.28	0.384	0.154	0.139
-11.56	0.415	0.160	0.345
-10.83	0.445	0.164	0.125
-10.11	0.447	0.160	0.153
-9.39	0.429	0.150	0.148
-8.67	0.395	0.142	0.205
-7.94	0.384	0.154	0.118
-7.22	0.384	0.146	0.096
-6.50	0.424	0.168	0.098
-5.78	0.424	0.169	0.102
-5.06	0.425	0.167	0.122
-4.33	0.428	0.149	0.122
-3.61	0.414	0.150	0.137
-2.89	0.400	0.158	0.158
-2.17	0.389	0.153	0.153
-1.44	0.390	0.172	0.142
-0.72	0.403	0.159	0.132
0.00	0.427	0.149	0.120
0.72	0.451	0.163	0.128
1.44	0.481	0.169	0.133
2.17	0.503	0.161	0.152
2.89	0.511	0.190	0.139
3.61	0.489	0.176	0.010
4.33	0.478	0.180	0.150
5.06	0.466	0.172	0.142
5.78	0.455	0.172	0.360
6.50	0.469	0.172	0.156
7.22	0.480	0.176	0.182
7.94	0.503	0.188	0.413
8.67	0.516	0.184	0.200
9.39	0.488	0.187	0.163
10.11	0.483	0.1967	0.453
10.83	0.463	0.190	0.276
11.56	0.480	0.189	0.205
12.28	0.523	0.193	0.203
13.00	0.552	0.190	0.211

Table A.15, Suction side spanwise effectiveness distribution downstream the MTJ scheme at different streamwise locations and Br = 0.375

z/d	x/d = 4.0	x/d = 25.0	x/d = 50.0
-13.00	0.500	0.267	0.218
-12.28	0.489	0.254	0.218
-11.56	0.506	0.252	0.241
-10.83	0.529	0.263	0.200
-10.11	0.531	0.254	0.210
-9.39	0.515	0.262	0.212
-8.67	0.498	0.255	0.209
-7.94	0.517	0.242	0.218
-7.22	0.528	0.255	0.205
-6.50	0.576	0.256	0.251
-5.78	0.563	0.261	0.199
-5.06	0.566	0.265	0.214
-4.33	0.564	0.254	0.209
-3.61	0.532	0.256	0.222
-2.89	0.499	0.255	0.232
-2.17	0.488	0.236	0.215
-1.44	0.487	0.254	0.229
-0.72	0.506	0.244	0.249
0.00	0.535	0.236	0.215
0.72	0.562	0.250	0.220
1.44	0.589	0.249	0.241
2.17	0.604	0.260	0.230
2.89	0.608	0.274	0.223
3.61	0.582	0.266	0.010
4.33	0.567	0.280	0.233
5.06	0.560	0.272	0.254
5.78	0.569	0.265	0.266
6.50	0.609	0.268	0.248
7.22	0.634	0.267	0.272
7.94	0.666	0.275	0.249
8.67	0.664	0.291	0.285
9.39	0.633	0.306	0.267
10.11	0.630	0.313	0.263
10.83	0.609	0.325	0.254
11.56	0.622	0.036	0.254
12.28	0.673	0.321	0.276
13.00	0.721	0.319	0.262

Table A.16, Suction side spanwise effectiveness distribution downstream the MTJ scheme at different streamwise locations and Br = 0.5

z/d	x/d = 4.0	x/d = 25.0	x/d = 50.0
-13.00	0.685	0.394	0.340
-12.28	0.650	0.381	0.336
-11.56	0.646	0.365	0.356
-10.83	0.642	0.368	0.309
-10.11	0.627	0.355	0.314
-9.39	0.601	0.349	0.311
-8.67	0.611	0.351	0.294
-7.94	0.657	0.341	0.315
-7.22	0.691	0.374	0.298
-6.50	0.729	0.374	0.291
-5.78	0.705	0.387	0.319
-5.06	0.692	0.383	0.327
-4.33	0.679	0.384	0.333
-3.61	0.633	0.367	0.350
-2.89	0.588	0.356	0.355
-2.17	0.575	0.341	0.333
-1.44	0.600	0.364	0.349
-0.72	0.646	0.356	0.356
0.00	0.682	0.353	0.328
0.72	0.700	0.365	0.337
1.44	0.709	0.377	0.375
2.17	0.713	0.383	0.366
2.89	0.718	0.390	0.349
3.61	0.696	0.381	0.406
4.33	0.683	0.386	0.358
5.06	0.680	0.378	0.366
5.78	0.703	0.367	0.369
6.50	0.772	0.372	0.350
7.22	0.810	0.376	0.365
7.94	0.806	0.380	0.350
8.67	0.793	0.405	0.384
9.39	0.767	0.436	0.373
10.11	0.759	0.424	0.362
10.83	0.740	0.435	0.350
11.56	0.748	0.211	0.335
12.28	0.810	0.405	0.350
13.00	0.852	0.389	0.314

Table A.17, Pressure and suction side HTC distribution over the vane surface without film cooling

x/d	ho Pressure side	x/d	ho Suction side
2.92	225.148	1.88	299.845
4.63	203.284	3.76	292.882
6.33	187.302	5.64	285.603
8.03	177.567	7.51	283.867
9.74	171.866	9.39	274.128
11.44	168.081	11.27	273.219
13.15	164.731	13.18	281.438
14.85	162.166	15.03	274.786
16.55	160.039	16.90	269.683
18.26	158.870	18.78	260.812
19.96	158.050	20.42	256.980
21.67	156.446	21.82	255.517
23.37	155.310	23.22	255.897
25.07	155.028	24.62	255.373
26.78	154.489	26.02	251.536
28.48	153.192	27.42	251.256
30.19	152.484	28.82	248.377
31.89	151.387	30.22	245.209
33.59	151.141	31.62	244.425
35.30	150.382	33.02	243.526
37.00	150.627	34.42	242.367
38.71	150.558	35.82	239.632
40.41	150.491	37.22	238.930
42.11	151.081	38.62	238.752
43.82	151.687	40.02	238.316
45.52	152.219	41.42	236.111
47.23	152.976	42.82	234.036
		44.22	235.208
		45.52	230.967
		46.73	227.746
		47.94	226.330
		49.14	225.215
		50.35	222.946
		51.55	220.735
		52.76	219.110
		53.97	217.684
		55.17	215.704
		56.38	213.979

Table A.18, Pressure side centerline and spanwise-averaged HTC ratio downstream the MTJ scheme at different blowing ratios

x/d	Br = 0. 5 Centerline	Br = 1.0 Centerline	Br = 1.5 Centerline	Br = 0.5 Average	Br = 1.0 Average	Br = 1.5 Average
2.92	1.670	1.606	1.611	1.404	1.375	1.521
4.63	1.290	1.704	1.789	1.145	1.416	1.679
6.33	1.291	1.777	1.913	1.135	1.358	1.743
8.03	1.196	1.479	1.965	1.122	1.315	1.761
9.74	1.159	1.406	1.915	1.114	1.287	1.711
11.44	1.101	1.494	1.987	1.059	1.244	1.649
13.15	1.019	1.335	1.831	1.041	1.177	1.593
14.85	1.079	1.247	1.838	1.061	1.213	1.654
16.55	1.178	1.469	2.026	1.041	1.210	1.624
18.26	1.080	1.250	1.710	1.034	1.174	1.565
19.96	1.000	1.180	1.647	1.011	1.107	1.460
21.67	1.000	1.128	1.502	1.007	1.095	1.430
23.37	1.000	1.058	1.438	1.000	1.076	1.392
25.07	1.000	1.144	1.503	1.013	1.054	1.307
26.78	1.000	1.000	1.104	1.000	1.009	1.241
28.48	1.000	1.000	1.357	1.004	1.022	1.249
30.19	1.000	1.000	1.276	1.000	1.014	1.229
31.89	1.000	1.040	1.387	1.000	1.005	1.185
33.59	1.000	1.000	1.231	1.000	1.008	1.168
35.30	1.000	1.000	1.280	1.000	1.003	1.178
37.00	1.000	1.032	1.365	1.000	1.001	1.129
38.71	1.000	1.000	1.167	1.002	1.002	1.117
40.41	1.000	1.095	1.441	1.000	1.008	1.116
42.11	1.000	1.000	1.256	1.000	1.000	1.111
43.82	1.000	1.000	1.245	1.000	1.002	1.109
45.52	1.092	1.049	1.407	1.005	1.010	1.138
47.23	1.000	1.000	1.195	1.007	1.003	1.130

Table A.19, Pressure side centerline and spanwise-averaged NHFR downstream the MTJ scheme at different blowing ratios

x/d	Br = 0. 5 Centerline	Br = 1.0 Centerline	Br = 1.5 Centerline	Br = 0.5 Average	Br = 1.0 Average	Br = 1.5 Average
2.92	1.813	1.512	1.428	1.615	1.400	1.350
4.63	1.363	1.308	1.308	1.263	1.231	1.239
6.33	1.117	1.087	1.113	1.050	1.083	1.084
8.03	0.943	0.971	0.918	0.898	0.958	0.940
9.74	0.834	0.882	0.816	0.786	0.858	0.828
11.44	0.776	0.760	0.701	0.731	0.796	0.761
13.15	0.730	0.731	0.635	0.679	0.756	0.700
14.85	0.636	0.698	0.542	0.621	0.694	0.625
16.55	0.567	0.569	0.440	0.600	0.652	0.586
18.26	0.558	0.617	0.500	0.575	0.628	0.563
19.96	0.600	0.601	0.477	0.568	0.627	0.564
20.81	0.577	0.548	0.454	0.564	0.618	0.563
22.52	0.562	0.545	0.478	0.536	0.607	0.557
24.22	0.548	0.561	0.468	0.517	0.602	0.559
25.93	0.581	0.618	0.560	0.536	0.639	0.601
27.63	0.529	0.574	0.509	0.486	0.588	0.551
29.33	0.499	0.607	0.536	0.458	0.568	0.534
31.04	0.475	0.579	0.528	0.426	0.644	0.622
32.74	0.471	0.581	0.550	0.438	0.566	0.554
34.45	0.444	0.558	0.510	0.421	0.554	0.540
36.15	0.424	0.549	0.472	0.410	0.547	0.532
37.85	0.428	0.544	0.451	0.404	0.541	0.546
39.56	0.395	0.532	0.470	0.392	0.536	0.546
41.26	0.419	0.561	0.561	0.380	0.525	0.529
42.97	0.385	0.521	0.517	0.367	0.519	0.535
44.67	0.366	0.516	0.463	0.360	0.517	0.533
46.37	0.399	0.531	0.539	0.333	0.495	0.495
48.08	0.331	0.506	0.481	0.318	0.492	0.500

Table A.20, Suction side centerline HTC ratio downstream the MTJ scheme at different blowing ratios

x/d	Br = 0.25 Centerline	Br = 0.375 Centerline	Br = 0.5 Centerline	Br = 0.625 Centerline
1.88	1.222	1.140	1.168	1.168
3.76	1.162	1.155	1.155	1.157
5.64	1.156	1.181	1.167	1.160
7.51	1.000	1.184	1.188	1.093
9.39	1.094	1.231	1.218	1.177
11.27	1.000	1.113	1.098	1.045
13.15	1.000	1.000	1.000	1.000
15.03	1.000	1.139	1.149	1.036
16.90	1.000	1.000	1.000	1.000
18.78	1.000	1.133	1.123	1.101
20.42	1.000	1.176	1.183	1.153
21.82	1.000	1.000	1.000	1.000
23.22	1.000	1.000	1.000	1.000
24.62	1.000	1.000	1.000	1.000
26.02	1.000	1.011	1.037	1.000
27.42	1.393	1.200	1.166	1.110
28.82	1.000	1.000	1.000	1.000
30.22	1.000	1.000	1.000	1.000
31.62	1.000	1.000	1.000	1.000
33.02	1.000	1.100	1.091	1.000
34.42	1.000	1.212	1.123	1.050
35.82	1.146	1.090	1.155	1.038
37.22	1.000	1.046	1.128	1.084
38.62	1.000	1.000	1.000	1.024
40.02	1.000	1.000	1.000	1.000
41.42	1.000	1.000	1.000	1.000
42.82	1.000	1.000	1.000	1.000
44.22	1.000	1.000	1.000	1.000
45.52	1.000	1.000	1.000	1.000
46.73	1.000	1.000	1.000	1.039
47.94	1.000	1.000	1.000	1.000
49.14	1.000	1.000	1.000	1.000
50.35	1.000	1.000	1.000	1.000
51.55	1.000	1.014	1.096	1.135
52.76	1.000	1.000	1.000	1.000
53.97	1.000	1.000	1.000	1.042
55.17	1.000	1.000	1.000	1.118

Table A.21, Suction side spanwise-averaged HTC ratio downstream the MTJ scheme at different blowing ratios

x/d	Br = 0.25 Average	Br = 0.375 Average	Br = 0.5 Average	Br = 0.625 Average
1.88	1.212	1.170	1.175	1.207
3.76	1.123	1.171	1.189	1.193
5.64	1.085	1.149	1.192	1.170
7.51	1.011	1.115	1.129	1.079
9.39	1.022	1.115	1.119	1.085
11.27	1.009	1.080	1.084	1.064
13.15	1.004	1.049	1.053	1.043
15.03	1.005	1.036	1.049	1.039
16.90	1.007	1.088	1.100	1.051
18.78	1.058	1.082	1.089	1.086
20.42	1.056	1.074	1.118	1.083
21.82	1.029	1.067	1.095	1.085
23.22	1.022	1.055	1.071	1.064
24.62	1.021	1.029	1.062	1.070
26.02	1.016	1.065	1.105	1.098
27.42	1.058	1.069	1.106	1.103
28.82	1.025	1.040	1.087	1.079
30.22	1.025	1.065	1.097	1.087
31.62	1.043	1.043	1.102	1.118
33.02	1.036	1.059	1.112	1.126
34.42	1.019	1.056	1.089	1.102
35.82	1.046	1.079	1.118	1.149
37.22	1.017	1.044	1.098	1.128
38.62	1.000	1.012	1.050	1.086
40.02	1.023	1.027	1.072	1.088
41.42	1.008	1.031	1.068	1.090
42.82	1.044	1.082	1.123	1.151
44.22	1.000	1.042	1.081	1.115
45.52	1.002	1.032	1.081	1.127
46.73	1.005	1.010	1.048	1.127
47.94	1.000	1.018	1.045	1.088
49.14	1.000	1.002	1.018	1.045
50.35	1.024	1.029	1.019	1.039
51.55	1.025	1.032	1.033	1.052
52.76	1.000	1.020	1.029	1.060
53.97	1.000	1.002	1.016	1.063
55.17	1.000	1.012	1.018	1.065

Table A.22, Suction side centerline NHFR downstream the MTJ scheme at different blowing ratios

x/d	Br = 0.25 Centerline	Br = 0.375 Centerline	Br = 0.5 Centerline	Br = 0.625 Centerline
1.88	0.944	1.210	1.421	1.420
3.76	0.811	1.007	1.216	1.249
5.64	0.629	0.830	1.078	1.119
7.51	0.577	0.702	0.929	1.007
9.39	0.454	0.617	0.864	0.941
11.27	0.464	0.612	0.844	0.930
13.15	0.424	0.607	0.819	0.886
15.03	0.379	0.494	0.729	0.839
16.90	0.346	0.563	0.776	0.833
18.78	0.327	0.436	0.686	0.762
20.42	0.329	0.416	0.673	0.763
21.82	0.323	0.494	0.722	0.782
23.22	0.309	0.460	0.663	0.737
24.62	0.301	0.428	0.623	0.716
26.02	0.287	0.418	0.623	0.725
27.42	-0.021	0.333	0.611	0.719
28.82	0.269	0.441	0.660	0.742
30.22	0.224	0.399	0.611	0.700
31.62	0.221	0.395	0.594	0.674
33.02	0.231	0.306	0.532	0.685
34.42	0.249	0.253	0.550	0.673
35.82	0.126	0.357	0.557	0.719
37.22	0.245	0.393	0.579	0.707
38.62	0.259	0.411	0.645	0.681
40.02	0.325	0.387	0.577	0.660
41.42	0.206	0.402	0.575	0.670
42.82	0.202	0.397	0.588	0.668
44.22	0.279	0.393	0.576	0.662
45.52	0.257	0.391	0.604	0.720
46.73	0.222	0.398	0.600	0.688
47.94	0.213	0.383	0.601	0.707
49.14	0.223	0.383	0.599	0.697
50.35	0.254	0.384	0.610	0.715
51.55	0.214	0.376	0.553	0.662
52.76	0.231	0.404	0.610	0.761
53.97	0.244	0.404	0.635	0.748
55.17	0.279	0.43	0.693	0.747

Table A.23, Suction side spanwise-averaged NHFR downstream the MTJ scheme at different blowing ratios

x/d	Br = 0.25 Average	Br = 0.375 Average	Br = 0.5 Average	Br = 0.625 Average
1.88	0.787	1.191	1.500	1.492
3.76	0.721	0.943	1.197	1.249
5.64	0.594	0.795	1.044	1.110
7.51	0.535	0.700	0.924	1.008
9.39	0.464	0.632	0.856	0.936
11.27	0.426	0.597	0.812	0.885
13.15	0.395	0.571	0.780	0.848
15.03	0.359	0.543	0.741	0.807
16.90	0.341	0.430	0.654	0.754
18.78	0.266	0.423	0.641	0.703
20.42	0.273	0.485	0.631	0.732
21.82	0.283	0.447	0.636	0.700
23.22	0.277	0.439	0.628	0.690
24.62	0.265	0.440	0.617	0.671
26.02	0.267	0.388	0.575	0.632
27.42	0.224	0.399	0.582	0.641
28.82	0.250	0.409	0.578	0.634
30.22	0.237	0.384	0.563	0.621
31.62	0.211	0.390	0.554	0.599
33.02	0.214	0.373	0.543	0.594
34.42	0.240	0.372	0.548	0.601
35.82	0.205	0.357	0.534	0.574
37.22	0.230	0.374	0.538	0.581
38.62	0.262	0.388	0.554	0.589
40.02	0.218	0.373	0.538	0.585
41.42	0.231	0.373	0.543	0.586
42.82	0.258	0.412	0.576	0.620
44.22	0.283	0.372	0.543	0.583
45.52	0.247	0.380	0.547	0.581
46.73	0.232	0.385	0.551	0.576
47.94	0.246	0.382	0.551	0.589
49.14	0.253	0.390	0.560	0.601
50.35	0.265	0.355	0.562	0.630
51.55	0.220	0.347	0.554	0.602
52.76	0.246	0.382	0.565	0.603
53.97	0.239	0.408	0.580	0.624
55.17	0.244	0.412	0.600	0.626

Table A.24, Pressure and suction sides specially-averaged NHFR downstream the MTJ scheme at different blowing ratio

	Br	NHFR
Pressure Side	0.50	0.590
	1.00	0.680
	1.50	0.655
Suction Side	0.25	0.306
	0.375	0.464
	0.50	0.655
	0.625	0.708

Table A.25, Mid-plane (z/d = 0.0) x-axis velocity ratio comparison for the MTJ scheme at Different downstream locations and Br = 0.5

y/d	u/V_{avg} x/d = 2.0	u/V_{avg} x/d = 4.0	u/V_{avg} x/d = 8.0	u/V_{avg} x/d = 16.0
0.00	0.000	0.000	0.000	0.000
0.22	0.355	0.592	0.679	0.762
0.44	0.464	0.602	0.693	0.787
0.66	0.643	0.700	0.754	0.831
0.88	0.794	0.762	0.808	0.871
1.09	0.844	0.807	0.853	0.915
1.31	0.876	0.876	0.900	0.947
1.53	0.943	0.916	0.933	0.975
1.75	0.973	0.953	0.955	1.005
1.97	1.000	0.990	0.977	1.012
2.19	1.035	1.012	1.009	1.029
2.41	1.051	1.030	1.025	1.059
2.63	1.070	1.053	1.040	1.076
2.85	1.084	1.069	1.061	1.087
3.06	1.104	1.080	1.078	1.096
3.28	1.130	1.010	1.094	1.106
3.50	1.138	1.112	1.102	1.113
3.72	1.156	1.129	1.117	1.123
3.94	1.173	1.150	1.135	1.136
4.16	1.180	1.157	1.148	1.144

Table A.26, Mid-plane (z/d = 0.0) x-axis velocity ratio comparison for the MTJ scheme at Different downstream locations and Br = 1.0

y/d	u/V_{avg} x/d = 2.0	u/V_{avg} x/d = 4.0	u/V_{avg} x/d = 8.0	u/V_{avg} x/d = 16.0
0.00	0.000	0.000	0.000	0.000
0.22	0.197	1.409	1.274	1.161
0.44	0.182	1.413	1.296	1.159
0.66	0.651	1.395	1.199	1.126
0.88	1.335	1.248	1.102	1.094
1.09	1.162	1.063	1.025	1.057
1.31	1.008	0.956	1.004	1.038
1.53	0.930	0.922	0.984	1.037
1.75	0.948	0.942	0.985	1.040
1.97	0.987	0.968	0.997	1.033
2.19	1.023	0.989	1.011	1.037
2.41	1.051	1.012	1.025	1.051
2.63	1.075	1.027	1.039	1.065
2.85	1.092	1.047	1.045	1.074
3.06	1.105	1.059	1.051	1.085
3.28	1.113	1.076	1.065	1.093
3.50	1.118	1.090	1.085	1.103
3.72	1.135	1.106	1.101	1.116
3.94	1.144	1.117	1.105	1.133
4.16	1.160	1.131	1.119	1.139

Table A.27, Mid-plane (z/d = 0.0) x-axis velocity ratio comparison for the MTJ scheme at Different downstream locations and Br = 1.5

y/d	u/V_{avg} x/d = 2.0	u/V_{avg} x/d = 4.0	u/V_{avg} x/d = 8.0	u/V_{avg} x/d = 16.0
0.00	0.000	0.000	0.000	0.000
0.22	0.038	1.649	1.460	1.358
0.44	0.148	1.736	1.500	1.355
0.66	0.490	1.573	1.382	1.289
0.88	1.221	1.317	1.205	1.220
1.09	1.146	1.178	1.107	1.152
1.31	0.969	1.040	1.097	1.102
1.53	0.952	0.978	1.064	1.083
1.75	0.994	0.978	1.036	1.075
1.97	1.026	0.989	1.038	1.061
2.19	1.044	1.025	1.049	1.067
2.41	1.071	1.047	1.062	1.091
2.63	1.095	1.062	1.078	1.110
2.85	1.128	1.085	1.092	1.116
3.06	1.144	1.102	1.100	1.129
3.28	1.159	1.125	1.115	1.137
3.50	1.175	1.138	1.133	1.147
3.72	1.188	1.151	1.151	1.155
3.94	1.200	1.166	1.158	1.169
4.16	1.217	1.174	1.156	1.183

Table A.28, Mid-plane (z/d = 0.0) x-axis velocity ratio comparison for the MTJ and the circular schemes at Different downstream locations and blowing ratios

	Br = 1.0		Br = 1.5	
y/d	u/V_{avg} x/d = 4	u/V_{avg} x/d = 8	u/V_{avg} x/d = 4	u/V_{avg} x/d = 8
0.00	0.000	0.766	0.000	0.218
0.22	0.706	0.888	0.577	0.807
0.44	0.873	0.981	0.854	0.925
0.66	0.941	1.033	0.945	0.977
0.87	0.946	1.052	1.017	1.035
1.09	1.003	1.042	0.992	1.076
1.31	1.157	1.032	1.119	1.160
1.53	1.230	1.042	1.374	1.141
1.75	1.184	1.106	1.442	1.146
1.97	1.112	1.141	1.383	1.190
2.19	1.117	1.145	1.235	1.221
2.41	1.137	1.153	1.177	1.254
2.62	1.159	1.173	1.166	1.272
2.84	1.183	1.179	1.169	1.236
3.06	1.193	1.195	1.173	1.208
3.28	1.206	1.201	1.185	1.190
3.50	1.212	1.206	1.204	1.201
3.72	1.219	1.209	1.205	1.207
3.94	1.224	1.225	1.200	1.207
4.04	1.223	1.227	1.202	1.214

Table A.29, Peak vorticity variation with blowing ratio increase at different x/d locations for both MTJ and circular hole schemes

Br	MTJ x/d = 2.0	MTJ x/d = 8.0	Circular x/d = 2.0	Circular x/d = 8.0
0.50	0.456	0.215	0.974	0.297
1.00	0.806	0.2838	2.83	0.636
1.50	0.9783	0.694	3.55	0.753

Table A.30, Dimensionless z- axis vorticity distribution at the mid-x-y plane (z/d = 0.0) for the MTJ scheme at different downstream locations and Br = 0.5

y/d	u/V_{avg} x/d = 2	u/V_{avg} x/d = 4	u/V_{avg} x/d = 8	u/V_{avg} x/d = 16
0	-0.243	-0.011	0.285	-0.118
0.22	-0.457	-0.249	-0.075	-0.161
0.44	-0.696	-0.355	-0.250	-0.203
0.66	-0.417	-0.211	-0.203	-0.210
0.88	-0.148	-0.240	-0.216	-0.189
1.09	-0.113	-0.264	-0.182	-0.141
1.31	-0.187	-0.154	-0.134	-0.140
1.53	-0.118	-0.138	-0.104	-0.091
1.75	-0.120	-0.137	-0.108	-0.070
1.97	-0.109	-0.082	-0.111	-0.119
2.19	-0.091	-0.089	-0.074	-0.115
2.41	-0.086	-0.098	-0.084	-0.058
2.63	-0.086	-0.062	-0.081	-0.040
2.85	-0.110	-0.050	-0.065	-0.046
3.06	-0.105	-0.075	-0.043	-0.050
3.28	-0.090	-0.070	-0.048	-0.043
3.50	-0.101	-0.087	-0.066	-0.048
3.72	-0.079	-0.068	-0.065	-0.049
3.94	-0.055	-0.003	-0.038	-0.036
4.16	-0.060	-0.033	-0.023	-0.052

Table A.31, Dimensionless z- axis vorticity distribution at the mid-x-y plane (z/d = 0.0) for the MTJ scheme at different downstream locations and Br = 1.0

y/d	u/V_{avg} x/d = 2	u/V_{avg} x/d = 4	u/V_{avg} x/d = 8	u/V_{avg} x/d = 16
0	-1.051	0.026	0.189	-0.001
0.22	-1.142	0.084	0.207	0.068
0.44	-1.184	0.447	0.450	0.120
0.66	-0.242	0.815	0.412	0.134
0.88	0.959	0.804	0.232	0.115
1.09	0.754	0.508	0.076	0.024
1.31	0.256	0.127	0.016	-0.018
1.53	-0.021	-0.049	-0.043	-0.001
1.75	-0.063	-0.074	-0.064	-0.009
1.97	-0.064	-0.070	-0.070	-0.048
2.19	-0.079	-0.053	-0.076	-0.074
2.41	-0.074	-0.062	-0.059	-0.047
2.63	-0.042	-0.063	-0.043	-0.038
2.85	-0.011	-0.057	-0.055	-0.043
3.06	-0.036	-0.075	-0.091	-0.043
3.28	-0.023	-0.061	-0.091	-0.055
3.50	-0.061	-0.061	-0.045	-0.075
3.72	-0.082	-0.053	-0.053	-0.058
3.94	-0.054	-0.051	-0.054	-0.032
4.16	-0.031	-0.048	-0.055	-0.046

Table A.32, Dimensionless z- axis vorticity distribution at the mid-x-y plane (z/d = 0.0) for the MTJ scheme at different downstream locations and Br = 1.5

y/d	u/V_{avg} x/d = 2	u/V_{avg} x/d = 4	u/V_{avg} x/d = 8	u/V_{avg} x/d = 16
0	-1.117	-0.313	-0.073	0.007
0.22	-1.039	0.217	0.231	0.144
0.44	-1.467	1.004	0.740	0.258
0.66	-0.512	0.897	0.626	0.264
0.88	0.936	0.597	0.232	0.256
1.09	0.535	0.516	0.0859	0.187
1.31	0.054	0.202	0.0909	0.092
1.53	-0.062	0.039	0.0215	0.075
1.75	-0.054	-0.043	-0.034	0.031
1.97	-0.039	-0.073	-0.049	-0.071
2.19	-0.026	-0.034	-0.063	-0.104
2.41	-0.069	-0.052	-0.073	-0.055
2.63	-0.103	-0.068	-0.045	-0.034
2.85	-0.085	-0.067	-0.055	-0.044
3.06	-0.066	-0.058	-0.071	-0.050
3.28	-0.044	-0.042	-0.084	-0.047
3.50	-0.048	-0.049	-0.045	-0.057
3.72	-0.049	-0.038	-0.005	-0.075
3.94	-0.044	-0.022	-0.013	-0.050
4.16	-0.051	-0.045	-0.051	-0.027